CZECH TECHNICAL UNIVERSITY IN PRAGUE

FACULTY OF NUCLEAR SCIENCES AND PHYSICAL ENGINEERING

DISSERTATION THESIS

2021

MARTIN DUDA

CZECH TECHNICAL UNIVERSITY IN PRAGUE

FACULTY OF NUCLEAR SCIENCES
and PHYSICAL ENGINEERING

THESIS

HARMONIC FREQUENCY GENERATION AND NONLINEAR COMPRESSION OF ULTRASHORT PULSES

Prague 2021 Ing. Martin Duda

Bibliografický záznam

Autor	Ing. Martin Duda, České vysoké učení technické v Praze, Fakulta jaderná a fyzikálně inženýrská, katedra fyzikální elektroniky
Název práce	Generace harmonických frekvencí a nelineární komprese ultrakrátkých impulzů
Studijní program	Aplikace přírodních věd
Studijní obor	Fyzikální inženýrství
Školitel	Ing. Martin Smrž, Ph.D., Fyzikální ústav Akademie věd ČR, centrum HiLASE
Školitel specialista	Prof. Ing. Václav Kubeček, DrSc., České vysoké učení technické v Praze, Fakulta jaderná a fyzikálně inženýrská, katedra fyzikální elektroniky
Akademický rok	2020/2021
Počet stran	104
Klíčová slova	Lasery, nelineární optika, generace harmonických frekvencí, ultrakrátké impulzy, tvarování impulzů

Bibliographic entry

Author	Ing. Martin Duda, Czech Technical University in Prague, Faculty of Nuclear Sciences and Physical Engineering, Department of Physical Electronics
Title of thesis	Harmonic frequency generation and nonlinear compression of ultrashort pulses
Degree programme	Application of Natural Sciences
Field of study	Physical Engineering
Supervisor	Ing. Martin Smrž, Ph.D., Institute of Physics of Czech Academy of Sciences, HiLASE Centre
Supervisor specialist	Prof. Ing. Václav Kubeček, DrSc., Czech Technical University in Prague, Faculty of Nuclear Sciences and Physical Engineering, Department of Physical Electronics
Academic year	2020/2021
Number of pages	104
Keywords	Lasers, nonlinear optics, second harmonic generation, ultrashort pulses, pulse shaping

Abstrakt

Nelineární frekvenční konverze z infračervené do viditelné spektrální oblasti je zajímavá pro vědeckou i komerční sféru. Proto je nutné mít k dispozici kompaktní a spolehlivý laserový zdroj s vysokým výkonem, pikosekundovými impulzy a výbornou kvalitou svazku, který pracuje v této části spektra.

První část dizertační práce popisuje vývoj a optimalizaci takového systému průmyslové kvality pro nelineární konverzi do viditelné spektrální oblasti s velmi vysokou účinností přeměny energie přesahující 75 %. Tento konverzní systém je s drobnými úpravami použit s několika různými laserovými vysokovýkonnými systémy.

Hlavní část práce je věnována originálnímu numerickému i experimentálnímu výzkumu nelineárního tvarování laserových impulzů z Yb:YAG vysokovýkonného laseru. Tvarování je založené na rozdílných grupových rychlostech a časovém zpoždění jednotlivých impulzů. Rozsáhlé numerické simulace ukazují, že se jedná o zajímavou metodu umožňující jednak kompresi frekvenčně zdvojených impulzů z jednotek pikosekund do oblasti nízkých stovek femtosekund a zároveň až pětinásobné zvýšení špičkového výkonu. Pro nejnovější generaci vysokovýkonných laserů s vlnovou délkou 1030 nm však dostupné nelineární krystaly neumožňují efektivní kompresi bez použití disperzního optického prvku. Experimentální výsledky naměřené s difrakční mřížkou způsobující naklánění čel vln naznačují, že dochází k nelineárnímu tvarování impulzů a kompresi v souladu s numerickými simulacemi. Například, s 20% účinností byl generovaný laserový impulz, jehož spektrum bylo natolik široké, že umožňovalo, aby byla délka impulzu kratší než 100 fs. Experimentální sestava, stejně jako diagnostika, je však citlivá na kvalitu svazku a vyžadovala by další optimalizaci, aby našla své praktické využití.

Abstract

Nonlinear frequency up-conversion from the infrared into the visible spectral range is of interest to both scientific and industrial communities. As such, there exists a need to have a compact and reliable laser source with high power, picosecond pulses and excellent beam quality operating in a defined spectral range.

The first part of this thesis describes the development and optimization of such industrial grade stage for nonlinear conversion into the visible spectral region with a very high energy conversion efficiency in excess of 75 %. This conversion stage is used, with small adjustments, in a number of high power laser sources.

Main part of the thesis is devoted to the original numerical and experimental research of nonlinear pulse shaping. The input pulses originate from a high-power Yb:YAG laser and the method is based on a group velocity mismatch and time predelay of the individual pulses. Extensive numerical simulations show, that it is an interesting method of decreasing duration of the up-converted pulses from few picoseconds to low hundreds of femtoseconds, while enhancing output peak power up to five times. However, for the current generation of high average power ultrafast lasers with a wavelength of 1030 nm, the available nonlinear crystals do not allow for an efficient pulse compression without the introduction of a dispersive element. With a diffraction grating causing tilting of the pulse fronts, the experimental results hint at an ongoing pulse shaping and compression in accordance with the numerical simulations. For example, pulse with a wide spectrum supporting a pulse duration of less than 100 fs was generated with a 20 % efficiency. However, the experimental setup, as well as the diagnostics, is sensitive on beam quality and would need further optimization, before it could find its practical uses.

Research is what I'm doing when I don't know what I'm doing.

—Wehrner von Braun

Acknowledgements

When I first met my superior, Ing. Ondřej Novák, Ph.D. in 2018, I automatically started to call him by his given name, because I thought he was only a student. He wasn't, and this was the first out of great many things that Ondřej showed me I didn't get right. Throughout the close to three years I spend at HiLASE centre, working on nonlinear optics, Ondřej was infinitely patient, allowing me to fail and break stuff, providing me with literature, reading my reports and manuscripts countless times, giving me feedback. He let me do interesting research, even when I didn't know what I was doing, and he was challenging me to do better. Thank you, Ondřej. I think I do better now than I did before, and I intend to grow further.

Ondřej and RNDr. Hana Turčičová, CSc. were the wise duo, sometimes each with a different idea, that taught me the most not only about harmonics generation, but also how to work in a lab and how not to get lost in the sheer amount of data both the literature and experiments provide me with.

My supervisor, Ing. Martin Smrž, Ph.D., ensured, that I had access to the equipment and beamtime I needed for my experiments. He also gave me a possibility to spend some time doing research in Japan, fulfilling my childhood dream.

There are, of course, other colleagues and friends, who helped me along the way, and made it fun and interesting, if only by their presence. I cannot possibly list them all, but I have to mention Ing. Martin Cimrman, who selflessly assisted me with the operation of the driving laser.

Lastly, but most truly, I have to thank my wife Aleksandra for her patience with my long experiments, for tolerating my absence from home, when I had to travel, and for giving me our beautiful daughter. They both give me strength to move forward, they encourage me to do my best and they show me, what matters the most. I am forever indebted to you. Thanks are insufficient, but they are all yours anyway, like everything else.

Martin Duda

26th May 2021

Contents

List of abbreviations

Abbreviation	Explanation
1H	First harmonic (frequency)
2H	Second harmonic (frequency)
AC	Autocorrelation
AR	Antireflection
ARW	AR coated window
BBO	Barium borate, β-BaB_2O_4
BD	Beamdump
BiBO	Bismuth borate, BiB_3O_6
BP	Beam profiler
DKDP	Potassium dideuterium phosphate, KD_2PO_4
DM	Dichoric mirror
FROG	Frequency-resolved optical gating
FT	Fourier transform or transformation
FTL	Fourier transform limited
FWHM	Full width at half maximum
GDD	Group delay dispersion
GVI	Group velocity index
GVM	Group velocity mismatch
HRR	High repetition rate
HWP	Half-wave plate
IR	Infrared
KDP	Potassium dihydrogen phosphate, KH_2PO_4
L	Lens
LBO	Lithium triborate, LiB_3O_5
M	Mirror
Nd	Neodymium
NLC	Nonlinear crystal
OPA	Optical parametric amplification
PBS	Polarizing beam splitter
PFT	Pulse front tilt

Continuing on the next page

Abbreviation	Explanation
PM	Power meter
RMS	Root mean square
RMSE	Root mean square error
SF	Sum frequency
SFG	Sum frequency generation
SHG	Second harmonic generation
STRIPED FISH	Spatially and temporally resolved intensity and phase evaluation device: full information from a single hologram
TBP	Time-bandwidth product
TFP	Thin film polarizer
Ti	Titanium
W	Wedge
W1, W2	Input wave 1 and 2
YAG	Yttrium aluminium garnet, $Y_3Al_5O_{12}$
Yb	Ytterbium

List of symbols

Symbol	Explanation
α	Pulse front tilt angle
α_0	External pulse front tilt angle
a, b	Geometry parameters for prisms
β_d	Diffraction angle
β_i	Angle of incidence
c	Speed of light
c_0	Speed of light in vacuum
γ, δ	Beam directions
d	Nonlinear coefficient
d_eff	Effective nonlinear coefficient
d_g	Grating constant
$D4\sigma$	Width according to the second moments
Δk	Phase mismatch
$\Delta t_\mathrm{P}^\mathrm{FWHM}$	FWHM pulse duration
$\Delta t_\mathrm{P}^\mathrm{min}$	Minimal pulse duration
$\Delta \tau_\mathrm{AC}^\mathrm{FWHM}$	FWHM duration of autocorrelation
e	Extraordinary polarization
E_p	Energy in pulse
$\mathcal{E}$	Electric field
ϵ	Ellipticity of a beam profile
ε	Permittivity
ε_0	Permittivity of a free space
η	Energy conversion efficiency
f	Frequency
ϕ	Azimuth angle of beam profile major axis
φ	One of the phase-matching angles
χ	Electric susceptibility
$\chi^{(2)}$	Second-order electric susceptibility
I	Intensity
I_p	Peak intensity

Continuing on the next page

Symbol	Explanation
k	Wavenumber
$\mathbf{k}$	Wavevector
L	Crystal length, crystal thickness
L_g	Temporal walk-off length
λ	Wavelength
m	Diffraction order
M^2 or $\mathbb{M}^2$	Beam quality parameter
μ	Permeability
μ_0	Permeability of free space
μ_A	Absorption coefficient
n	Index of refraction
$\bar{n}_e$	Principal value of the extraordinary refractive index
n_g	Group index of refraction
ν	Optical frequency
o	Ordinary polarization
ω	Angular optical frequency
P	Power
P_AV	Average power
$P(x,y)$	Power density distribution
$\mathcal{P}$	Polarization
$\mathcal{P}_{NL}$	Nonlinear component of polarization
ρ	Spatial walk-off
S_0	Mixing strength
$\mathbf{S}$	Poynting vector
σ	Standard deviation
t	Time
τ	Delay
θ	One of the phase-matching angles
v_g	Group velocity

1 Introduction

1.1 Motivation and goals

Ytterbium (Yb) doped solid state lasers have broad absorption and emission spectrum, a low level quantum defects and simple electronic structures. Therefore, they are suitable for direct diode pumping, allowing for high pulse repetition rates and high average powers. For the average powers in excess of 1 kW, high repetition rate lasers with very high beam quality and laser pulses with few picoseconds in duration, Yb doped thin disk lasers [1], such as those based on yttrium aluminium garnet (YAG) matrix and developed at HiLASE centre [2–4], are without a doubt laser systems of choice for various industrial applications like micro-machining and fabrication of functional surfaces [5–8]. They are also valued in scientific community for e.g. laser produced plasma extreme ultraviolet sources [9, 10] or laser induced damage threshold testing [11].

The second harmonic generation (SHG) of these lasers, which are normally emitting at $\approx 1\,\mu m$ wavelength, is important to both scientific community, because it allows one to pump optical parametric amplification (OPA) stages [12], as well as to industry for micromachining, such as welding and drilling [13, 14]. Finally, the green laser light can be converted further to the UV spectral region, which is useful for e.g. laser cutting and manufacturing of electronic devices [15] or laser annealing of nanotube layers [16]. To utilize the important qualities of thin-disk lasers, like excellent beam quality and high power, efficient energy conversion in thin borate crystals have to be employed for frequency doubling.

My thesis encompasses nonlinear frequency conversion of infrared (IR) light generated in the Yb doped thin-disk lasers at the wavelength of 1030 nm into the visible spectral range, specifically green light at a wavelength of 515 nm. **The first goal of the thesis is to develop and optimize stages for frequency conversion, which are used for both scientific and industrial applications.** This topic is expanded upon in chapter 2.

The visible laser beam can be generated with very high conversion efficiency, if the nonlinear crystal is carefully matched to the parameters of the driving laser. However, when certain conditions are imposed onto the nonlinear optical

crystal and the driving laser, pulse shaping and pulse compression of the second harmonic (2H) beam can take place throughout the generation process.

Some scientific (e.g. high harmonic generation, [17]) and industrial (e.g. material processing, [18]) applications require pulses shorter than 1 ps achievable with Yb:YAG thin-disk lasers. In the femtosecond regime, they have to rely on the Ti:sapphire laser, which works at a wavelength of 800 nm, and is limited in the available average power. Broadening the spectrum and compressing the pulses of the Yb:YAG lasers could make them more attractive for these applications and widen their potential use.

Nonlinear spectral broadening and pulse compression of Yb:YAG lasers in multi-pass gas cell [19] is an emerging method to compress picosecond pulses down to the tens of femtoseconds, while keeping the spectrum in the IR region. However, I take a different approach, and **as the second goal of my thesis, I research the nonlinear pulse shaping and compression through second harmonic generation**, discussed in more detail in an introductory section 1.4. The numerical simulations concerning nonlinear pulse shaping are presented in chapter 3 and experimentally demonstrated in chapters 4 and 5.

In the next few introductory sections, basic concepts and terminology for second-order nonlinear optics and frequency mixing are introduced, including some specific phenomena for spatially limited beams (like spatial walk-off) and ultrashort light pulses (temporal walk-off). The introduction is based on classical texts in the field of nonlinear optics [20–22] and is by no means intended to be comprehensive. Next, I expand on the topic of the second harmonic generation of ps long pulses and I provide key details about the lasers, for which I develop the universal SHG stage. Furthermore, I introduce the principles of nonlinear pulse shaping in detail and at the end of this chapter, I provide a description of the data collection and processing routine used throughout my experiments.

1.2 Basic concepts in nonlinear optics

In linear homogenous isotropic non-dispersive dielectric media, there is a linear dependence between polarization $\mathcal{P}$ and electric field $\mathcal{E}$:

$$\mathcal{P} = \varepsilon_0 \chi \mathcal{E}, \tag{1.1}$$

where ε_0 is permittivity of a free space and χ is the electric susceptibility of the dispersive medium, which is related to the refractive index n of medium by $n^2 = 1 + \chi = \varepsilon/\varepsilon_0$. In nonlinear optical media, the relation is linear only for small $\mathcal{E}$, but at high electric field and high *intensity* I, which is proportional to

the square of the electric field, $I \propto \mathcal{E}^2$, the relation becomes nonlinear. This can be written as

$$\mathcal{P} = \varepsilon\chi\mathcal{E} + \varepsilon_0\chi^{(2)}\mathcal{E}^2 + \ldots, \tag{1.2}$$

where $\chi^{(2)}$ is a second-order susceptibility and describes the strength of the second-order nonlinear effect. Higher order nonlinear components are omitted. It is also customary to write

$$\chi^{(2)} = 2d, \tag{1.3}$$

where d is a (second order) *nonlinear coefficient*.

The propagation of light can be described by wave equation derived from Maxwell's equations, and in nonlinear medium it has a form

$$\nabla^2\mathcal{E} - \frac{1}{c^2}\frac{\partial^2\mathcal{E}}{\partial t^2} = \mu\frac{\partial^2\mathcal{P}_{NL}}{\partial t^2}, \tag{1.4}$$

where c is a speed of light, $c = c_0/n$, $c_0 = 1/\sqrt{\varepsilon_0\mu_0}$ is speed of light in vacuum and

$$\mathcal{P}_{NL} = 2d\mathcal{E}^2. \tag{1.5}$$

In anisotropic medium, each component of the polarization vector is a function of three components of the electric field, eq. (1.5) can be written as

$$\mathcal{P}_{i,NL} = 2\sum_{jk} d_{ijk}\mathcal{E}_j\mathcal{E}_k. \tag{1.6}$$

There are various symmetries, usually dependent on the nonlinear material, which reduce the number of elements in d_{ijk}.

If one assumes, that the electric field $\mathcal{E}(t)$ comprises of two harmonic components at angular frequencies ω_1 and ω_2, the nonlinear component of polarization $\mathcal{P}_{NL}$ consists of components with sums, differences and doubles of the original frequencies. Only one of those components can be generated efficiently, and so this so called three-wave mixing (two input waves and one output wave) can be used for *sum frequency generation* (SFG), where the medium acts as a light source of frequency $\omega_3 = \omega_1 + \omega_2$. Special case is *second harmonic generation*, when $\omega_1 = \omega_2$ is called *first harmonic frequency* (1H frequency) and $\omega_3 = 2\omega_1$ is called *second harmonic frequency* (2H frequency).

Atom in the nonlinear optical medium will develop oscillating dipole moment with frequency ω_3 and will be radiating at this frequency. There are many atoms in the material, each oscillating with a phase determined by the incident

waves. If the relative phase of each atomic dipole is correct, radiation from them will add constructively and create the third well-defined wave.

The conditions for three-wave mixing are therefore dictated by two laws of conservation: energy (temporal or *frequency matching* condition) and momentum (spatial or *phase matching* condition):

$$\omega_1 + \omega_2 = \omega_3, \qquad \text{(frequency matching)} \tag{1.7}$$

$$\mathbf{k}_1 + \mathbf{k}_2 = \mathbf{k}_3, \qquad \text{(phase matching)} \tag{1.8}$$

where $\mathbf{k} = \omega n \mathbf{k}_0$ is a wavevector. Satisfying these matching conditions is necessary for the sustained mutual interaction of the three waves over large region of space and long duration of time. In collinear three wave mixing and dispersive media, satisfying both frequency-matching and phase-matching condition would be impossible without compensation by e.g. birefringence.

1.2.1 Phase-matching by birefringence, polarizations

In anisotropic medium, the refractive indexes are dependent on polarization of the waves, on the directions of the wavevectors relative to the optical axis, and on the temperature. To control the refractive indices at each optical frequency and achieve perfect phase matching of $\Delta k = k_3 - k_2 - k_1 = 0$, angle tuning and/or temperature tuning can be employed.

Angle tuning is simple, as for e.g. uniaxial crystals, the n of one polarization is dependent on the angle θ of propagation direction $\mathbf{k}$ to the optical axis (*extraordinary polarization*) by relation

$$\frac{1}{n_e(\theta)^2} = \frac{\sin^2\theta}{\bar{n}_e^2} + \frac{\cos^2\theta}{n_o^2}, \tag{1.9}$$

where $\bar{n}_e$ is principal value of the extraordinary refractive index and n_o is the refractive index of *ordinary polarization*, which is not angle dependent. There is, however, one drawback of angle tuning. When $\theta \notin \{0°, 90°\}$, the direction of wave propagation $\mathbf{k}$ and energy propagation $\mathbf{S}$ are different for extraordinary waves. This causes effect called *spatial walk-off* ρ, where the spatially limited ordinary and extraordinary waves diverge one from another, spatial overlap is limited and mixing efficiency (proportion of energy in the generated wave to the energy of the input waves, also called *conversion efficiency* η) is eventually decreased. The walk-off angle can be calculated from

$$\tan\rho = -\frac{1}{n_e}\frac{\mathrm{d}n_e}{\mathrm{d}\theta} \tag{1.10}$$

and for example, in Type II SHG of ≈ 1 µm Yb:YAG laser pulse in beta barium borate (BBO) crystal, the walk-off is around 70 µm/mm of the crystal length. For biaxial crystals like lithium triborate (LBO, LiB_3O_5), the calculation is more complicated.

For some crystals, the birefringence is strongly dependent on temperature, allowing *temperature tuning*, and it is sometimes possible to fulfil the phase matching condition with $\theta = 0°$ or $\theta = 90°$. The mixing process is then *non-critically phase-matched* and there is no spatial walk-off.

Usually, Δk does not need to be strictly zero, but below some limit. If the small, but tolerable *phase mismatch* is caused by angular inaccuracy, the range of acceptable angles is called *angular acceptance*. The acceptance bandwidth is dictated by $\Delta k \propto L^{-1}$, where L is length of the crystal, with the exact value dependent on a chosen definition. However, it always follows, that shorter crystal has larger acceptance bandwidth and thus is less susceptible to alignment inaccuracy and beam divergence.

If the wave with the highest frequency has different polarization than the other two waves, one calls it *Type I* phase-matching. If it has the same polarization as one of the other waves, it is called *Type II* phase-matching. Illustration of angle tuning and two types of phase-matching is in figure 1.1.

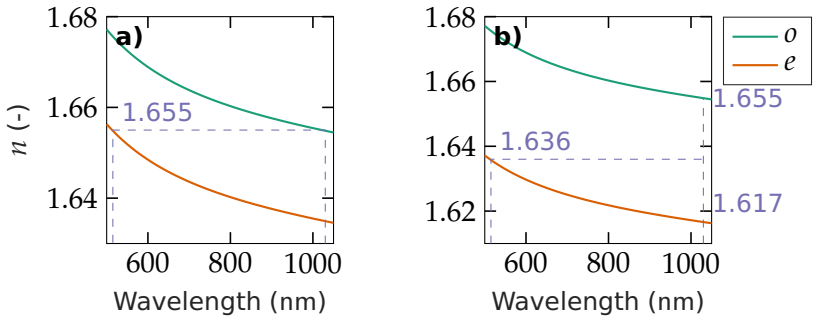

Figure 1.1: Illustration of two phase-matching types in BBO crystal: (a) type I at $\theta = 23.4°$ with the index of refraction n of ordinary polarization o at the wavelength of 1030 nm equal to the n of extraordinary polarization e at the wavelength of 515 nm; (b) type II at $\theta = 33.7°$, where n_e at 515 nm is equal to the average of the n_o and n_e at 1030 nm.

If one has a crystal of specific crystallographic group and orientation, one can calculate the so called *effective nonlinear coefficient* d_{eff}, which is a scalar calculated from d_{ijk} and it is the basic parameter to describe and compare the strength of nonlinear interaction in various crystals. If at least one interacting

wave has peak intensity comparable to *mixing strength* S_0 defined by

$$S_0 = \frac{\varepsilon_0 c^3 n_1 n_2 n_3}{2 d_{\text{eff}}^2 \omega_1 \omega_2 L^2}, \tag{1.11}$$

efficient energy transfer between the waves can take place. For Gaussian pulses, the *peak intensity* can be calculated by equation

$$I_{\text{peak}} = \frac{0.598 \times E}{(D4\sigma/20)^2 \, \Delta t_{\text{P}}^{\text{FWHM}}} \times 10^3 \left(\text{GW/cm}^2; \text{J}, \text{mm}, \text{ps}\right), \tag{1.12}$$

where $\Delta t_{\text{P}}^{\text{FWHM}}$is a pulse duration measured as a full width at half of the maximum (FWHM), $D4\sigma$ is diameter of a Gaussian beam, and E is energy in pulse. One can see from eq. (1.11), that for short crystals, the necessary peak intensity is higher than for long crystals. However, there is an upper limit of the peak intensity imposed by the *damage threshold* of the nonlinear crystal. Beyond this intensity, the crystal can get cracked.

When considering second harmonic generation, then for the low input intensities, the 2H conversion efficiency is small and grows linearly with increasing input intensity, $\eta \propto I_{1\text{H}}$, and the 2H intensity grows with the square of the 1H intensity, $I_{2\text{H}} \propto I_{1\text{H}}^2$. Once the 1H wave becomes significantly depleted, the increase of the 2H intensity becomes slower.

1.2.2 Pulsed nonlinear optics

In three-wave mixing process of ps long pulses, the three pulsed waves travel at their *group velocities* (velocities of the pulse envelope)

$$\begin{aligned} v_g &= \frac{c_0}{n_g} \\ &= \frac{c_0}{n}\left(1 + \frac{\lambda}{n}\frac{\mathrm{d}n}{\mathrm{d}\lambda}\right), \end{aligned} \tag{1.13}$$

where n_g is a group index of refraction and λ is a wavelength. The amplitudes of the waves are altered by the mixing process. If the pulse is very short (i.e. broadband), the red and blue part of the spectrum will have different group velocities and the colours will separate with propagation. This is *group velocity dispersion*, which leads to a frequency chirp and a reshaping of the pulse envelope. In the case of mixing of ps pulses, this second order dispersion effect can be usually neglected. What is important, however, is that the group velocities of the three mixed pulses can be different. This is called *group velocity mismatch* (GVM), and results in the eventual separation of the pulses and ceasing of the

mixing process. The pulse separation is called the *temporal walk-off* effect and for efficient mixing, the *temporal walk-off length*, defined by

$$L_g = \frac{c_0 \Delta t_{\mathrm{P}}^{\mathrm{FWHM}}}{\left| n_{g,1} - n_{g,3} \right|}, \tag{1.14}$$

where $\Delta t_{\mathrm{P}}^{\mathrm{FWHM}}$ is a FWHM pulse duration, has to be as small as possible. For Type II SHG of 1 ps long Yb:YAG laser pulse in BBO crystal, $n_{g,1} = 1.636$ and $n_{g,3} = 1.682$, resulting in $L_g = 6.5\,\mathrm{mm}$. This length poses an upper limit onto the nonlinear crystal thickness, and in order to achieve efficient conversion in a thin crystals, one has to use high intensities, sometimes close to the damage threshold.

When considering mixing of plane waves, the highest conversion efficiency is obtained, when the number of input photons in the interacting waves is balanced. This condition can be easily met in Type I SHG, where there is only one input wave (although for the sake of calculations, it is usually taken as two identical waves of half intensity). In other configurations, the waves can have photon balance at the start of the mixing process, but because they have varying spatial and temporal profile and they experience walk-off, they loose the photon balance as they propagate. The input waves transfer energy to the ω_3 wave, and the input wave with fever photons is gradually completely depleted after certain distance. Another mixing process starts, when the ω_3 wave will start to regenerate one of the input waves, till it depletes again. This cycling of energy is called *back-conversion* and has strong detrimental effect on energy mixing efficiency.

The effect of back-conversion is illustrated in figure 1.2, where the energy of the resulting 2H pulse is shown. This hypothetical example shows a numerical simulations with two input Gaussian pulses with the same parameters and an energy of 1 mJ being converted in a nonlinear crystal under perfect phase-matching. Virtually all of the energy is converted into the 2H pulse. But if a slight phase-mismatch is introduced, there exist an optimal thickness, where the highest 2H energy is obtained, and after exceeding this thickness, the energy is converted back to the input pulses. Afterwards, the energy oscillates with decreasing amplitude around some low value of energy. Finally, when the pulses are perfectly phase-matched, but there is a large GVM between them, the back-conversion appears at a different time, and since the interacting pulses cannot interact for a long time, the subsequent oscillations are damped more quickly.

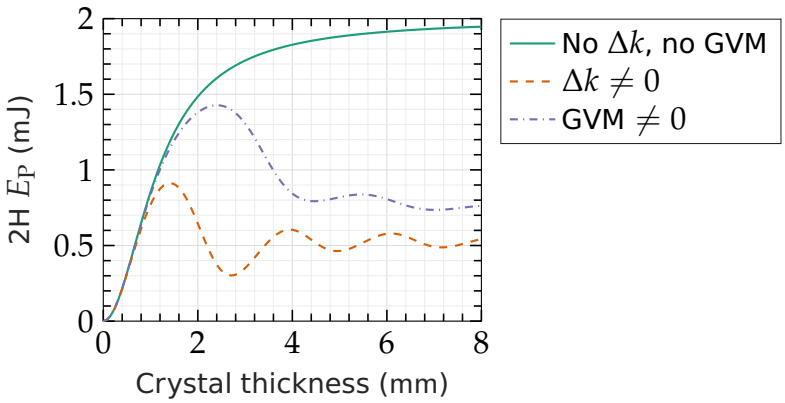

Figure 1.2: Illustration of energy exchange in nonlinear optical crystal. Energy of the generated pulse 2H E_P in dependence on crystal thickness is shown under three conditions: perfect phase-matching and no group velocity mismatch, slightly phase-mismatched SHG process with $\Delta k \neq 0$, and a case with perfect phase-matching, but with all the pulses having different group velocities.

1.3 SHG stage for ps lasers with high efficiency

1.3.1 Overview of target laser systems

The first aim of my work is to design, build and characterize reliable and maintenance-free stages for SHG of various laser system with ≈ ps long pulses and high energies currently being build or in operation at HiLASE. The various laser systems, for which the simple design is used, are following:

Perla B, an Yb:YAG thin disk laser with an excellent beam quality $M^2 < 1.2$, 1 kHz repetition rate, 10 mJ of energy and pulse duration below 2 ps. The energy in pulse is limited by the compressor. Improvement is planned for the near future to allow 20 mJ of energy in the compressed pulse.

DG laser is a similar thin disk laser system working at 1 kHz repetition rate, but with energy in pulse of 100 mJ after compression. This laser is designed for laser induced damage threshold measurements.

Perla HRR, where HRR stands for High Repetition Rate, are high power lasers developed for subjects outside of HiLASE centre, with usually higher repetition rates between 60 and 100 kHz, and proportionally lower energies in pulse, but still being built on the same general thin disk platform.

1.3.2 Literature review

Looking at papers about SHG of ps laser pulses from the last five years, one can see, that the nonlinear crystal of choice is usually LBO due to its high damage threshold, and the limit of the conversion efficiency η is below 75 %. Specifically, authors of papers [23, 24] used 1.5 mm thick BBO crystal and a laser source with 1 ps duration and a repetition rate of 5 kHz, and they generated 14 mJ of energy in the 2H pulse with an efficiency of 70 %. The input peak intensity was 80 GW/cm^2 and the 2H power was 70 W. More recently, authors of [25] presented about their thin-slab amplifier generating pulses with a duration of 0.9 ps and a repetition rate of 1 MHz, and they generated 95 W of the 2H beam in an LBO crystal with an efficiency of 74 %. The pulse energy was around 95 µJ.

Authors of [26] demonstrated a thin-disk laser with a pulse duration of 7.7 ps and a repetition rate of 300 kHz, and they achieved output 2H power of astounding 1400 W with an efficiency of 71 %. The conversion happened in a 5 mm long LBO crystal, with input intensity of 9 GW/cm^2, and the energy of the 2H pulse was 4.7 mJ. When one increases the pulse duration, group velocity mismatch stops imposing the limit on the conversion efficiency, so for example in paper [27], 76 ps long pulses with a repetition rate of 200 Hz were converted, in 7 mm thick LBO crystal cut for type II phase matching, with 79 % efficiency, reaching energy in pulse of 730 mJ, with the average output power being almost 150 W.

1.3.3 Specification of goals and methods

From the mentioned papers I expect, that to achieve efficient frequency conversion for ps pulses, I have to use *short crystals in the order of few* mm to eliminate the effect of temporal walk-off and to maintain good beam quality of the lasers. Requirement of high conversion efficiency leads to the need of using *high peak intensities* (between 10 and 100 GW/cm^2), which are generally limited by the damage thresholds of the optical components. Since the damage threshold of the LBO crystal is the highest among the nonlinear crystals, the next limiting optical element in the SHG setup are harmonic separators, and the damage threshold is above 90 GW/cm^2 of peak intensity at fundamental frequency before the frequency convertor. If high quality harmonic separators are used, using laser beams with intensities of up to 100 GW/cm^2 is possible.

Going back to the goal of building the SHG stages at the mentioned lasers, I should preferably reach *conversion efficiency of* 70 % to be on par with the recently published results. Before the start of my work, the only SHG stage at one of the HiLASE ps laser systems was operating at around 56 % of conversion efficiency [28, 29]. **I have build and optimized a SHG stage for the Perla B**

laser system, reaching conversion efficiencies of 80 % with various crystals, and I published the experiments in paper [30]. The experiments are presented in chapter 2 in more detail.

In the text I arrive to a conclusion, that one has to balance between a high conversion efficiency and a good beam quality of the laser, depending on the intended applications. At lower input intensities, the beam quality can be very good. As one increases the input intensity, region of maximum η is reached, but the beam quality worsens. After further increase of I, the beam quality worsening gets quicker and the conversion efficiency start to decrease due to the process of back-conversion, described in section 1.2.2.

The back-conversion not only worsens the beam-quality, but it also changes the shape of the 2H pulse – first, it creates a square-like pulse shape and if the back-conversion continues, double-peaked pulse develops. Even for this one can find an application, which is in contrast to the goal of reaching as high output power and beam quality as possible. **This simple picosecond pulse shaping technique can be useful e.g. for pumping of optical parametric chirped pulse amplification** [31]. For this particular application, flattop-like temporal profile of pump pulses or even flattop pulses with pronounced edges (like those in fig. 2.7b and c), lead to enhanced total conversion efficiency of the OPA processes. More importantly, gain-narrowing is eliminated and the OPA bandwidth is much larger than without using non-trivial pulse shapes.

1.4 Nonlinear pulse shaping

Except for this simple back-conversion in type I phase-matched nonlinear process, there exist other techniques for pulse shaping through nonlinear frequency conversion, which are usually used for obtaining much shorter pulses with high conversion efficiency, or generating rapid trains of short pulses, by the use of the group velocity mismatch discussed also in section 1.2.2. This approach is described in the following subsections.

1.4.1 Working principle

Sum frequency generation, particularly second harmonic generation, as a method of pulse compression, was first established in papers [32, 33]. When one uses nonlinear crystal cut for type I phase matching, as I do in chapter 2 and shortly discuss in the previous section, one can view it as a degenerated three wave mixing process, where the two input waves have the same frequency and the same polarization, and the energy is divided between them in half.

There is only one input wave, so both input waves in the three wave mixing process are identical, and they experience the same material properties of the nonlinear crystal. However, when the crystal is cut for type II phase matching, the input wave consists of two distinct waves. One has ordinary polarization and other extraordinary one, and each of the waves experience different material parameters, especially index of refraction n and group velocity v_g.

This leads to a group velocity mismatch being present between all three interacting waves. Normally, the GVM limits the conversion efficiency of very short pulses, but the authors of [32] noticed, that under particular conditions, the GVM can be actually used to increase the conversion efficiency and the ratio of peak power of 2H and 1H pulses can even exceed 100 % due to the pulse shortening of the generated wave. The specific and essential condition is, that the perpendicularly polarized pulses do not arrive into the crystal at the same time, but the faster one is predelayed* in respect to the slower one. If the predelay is just right, the faster pulse meets the slower one in the crystal and they will propagate together and partly overlap throughout the whole crystal length. This will increase the efficiency of the process, and as a side effect, it can also shorten the second harmonic pulse.

The authors of [32] studied the role of predelay on the second harmonic generation by the means of simple numerical simulations, and found specific values of predelay and crystal thickness for one particular laser, where either the energy conversion efficiency or the power conversion efficiency is the highest. Authors of [33] were more thorough in their investigation and offer a deeper insight into the pulse compression process, describing it more generally for the sum frequency generation.

The authors found, that the pulse compression is the most effective, when the group velocity of the SF wave v_g^{SF} is exactly halfway between the group velocities of the input waves v_g^{W1} and v_g^{W2}, where W1 and W2 are the input waves with ordinary and extraordinary polarization, respectively, when one is considering type II SHG, or they can be fundamental and frequency doubled wave, when considering third harmonic generation of any type.

The mechanism is sketched in figure 1.3. In the coordinate system connected with the SF pulse, the input waves W1 and W2 must move in opposite directions with the same velocities – they are approaching the SF pulse from two sides, and the SF pulse stays just in the middle of them.

*Grammar note: From the grammatical point of view, *pre-delay* is a correct form of the word. However, *predelay* without the hyphen is the form most commonly used in the literature. I follow this literature standard, and, as the classics say, the grammar will change and follow what people speak anyway.

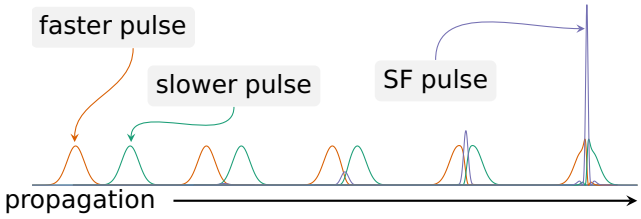

Figure 1.3: Sketch of the pulse compression mechanism showing the evolution of the SF pulse in different propagation times. The faster and slower pulse propagate through the crystal and are approaching one another. Eventually, short SF pulse with high peak power is generated at their small temporal overlap, while the input pulses are being depleted.

Now, the faster input pulse is sent into the crystal with a delay after the slower input pulse. As they propagate in the nonlinear crystal, the faster one will eventually catch up to the slower one. The SF pulse is then generated in the time interval, when the input pulses are passing one through another. If the nonlinear interaction between the pulses is strong enough – there is a strong energy exchange – almost all energy from the input pulses can be transferred to the SF pulse directly as they meet. This means, that the SF pulse will be generated only in the small temporal overlap, while depleting the input pulses, so it will remain as short as the temporal overlap necessary for the energy exchange to take place.

The resulting SF pulse can be much shorter than the input pulses and can have much higher intensity, but only, if the relation between the group velocities is just right – the group velocity of the SF pulse v_g^{SF} is an arithmetic mean of the group velocities v_g^{W1} and v_g^{W2}. The process can then be controlled by adjusting the predelay of the input pulses to compensate the delay generated by GVM in a crystal of particular length. If the group velocities are different, backwards energy transfer starts quite early and the conversion efficiency is limited. This can, however, be mitigated by a nonsymmetrical shapes of the input pulses or, more interestingly, by having input waves of different intensities. One final note is, that no group velocity dispersion components are needed for the pulse shaping to occur, making this potentially simple, cheap, compact and simple-to-align method of pulse compression.

1.4.2 Literature review

It is not an easy task to find a crystal, where the particular condition on group velocities for the selected wavelengths is satisfied. There have been reports of successfully utilizing this phenomena in a potassium dihydrogenphosphate (KDP)

or potassium dideuterium phosphate (DKDP) crystal for SHG of Nd:glass laser with a wavelength of 1053 nm to compress the frequency doubled pulse with duration between 1 and 12 ps up to 32 times [34–37]. Energy conversion efficiency of this process is usually reported to be lower compared to a type I phase matching, reaching 40 %. These frequency doubled pulses have been reported to be useful for compressed third [38] and fourth harmonic generation [39, 40].

Another possible combination of wavelengths and crystal has been reported in [41]. The authors used approximately 1 ps long pulses, the wave 1 had wavelength of 1055 nm and wave 2 between 1400 to 2200 nm. They generated compressed pulses at $600 - 720$ nm in BBO crystal, and they compressed the pulses down to 160 fs. In [42], 160 fs long pulses from travelling wave parametric amplifier pumped by Ti:Sapphire laser were also compressed in BBO crystal down to 34 fs. The wavelengths of the input pulses were 1.3 µm and 1.95 µm, with the resulting wavelength being around 780 nm.

Other theoretical investigation [43] has focused more on the case, where v_g^{SF} is not strictly an average of v_g^{W1} and v_g^{W2}. Apart from the predelay, crystal thickness and total input intensity, which has to be sufficiently large to ensure strong energy exchange in the nonlinear process, the ratio of the input intensities in the slower and faster input pulses are responsible for the resulting pulse shape and duration. The paper also shows, that due to the required high input intensities, the SF pulses are usually affected by a temporal breakup effect caused by the interaction between conversion and back-conversion processes, leading to generation of satellite pulses.

This back-conversion effect is normally detrimental to the beam quality and pulse temporal profile, but can be used to compress any of the three interacting pulses, if the proper ratio of input intensities is chosen [44]. If the intensity is even higher and back-conversion is stronger, a train of short pulses can be generated [45].

SFG and pulse compression of Yb doped solid state lasers were numerically studied in [46], assuming SHG in a KDP crystal. Unfortunately, for high power high repetition rate Yb:YAG thin-disk lasers, crystals from the PO_4 family like (D)KDP are not suitable due to their high linear absorption.[†] Commonly, borate crystals are used, as they have much better thermal properties. Pulse compression by SHG of Yb:YAG thin-disk laser has been demonstrated in [49]. The authors used simple collinear scheme and BBO crystal cut for type II phase-matching, and they claim, that they achieved fourfold compression, even though

[†]Before other nonlinear crystals were available, various methods for crystal cooling were developed, see for example [47]. For comparison, in 1 cm thick KDP crystal, around 8 % of the optical power at 1030 nm is absorbed. In LBO crystal, only around 0.06 % of power gets absorbed [48].

the v_g^{SF} does not lie in between the group velocities of input pulses in this particular crystal configuration [48]. The main mechanism for compression was the interaction between conversion and back-conversion process and the method of pulse duration measurement was an autocorrelation. Unfortunately, the authors provide very little detail to their experiment. I reported similar experiments in [50, 51] and will get to them in the fourth chapter.

1.4.3 Manipulating group velocities

To utilize different crystals at new wavelengths, two techniques to manipulate the group velocities have been developed. The use of pulses with tilted pulse fronts has been proposed in [52–54]. **The authors used this technique and by manipulating the pulse front tilt of the input pulses, they changed the effective group velocity of the SF pulse** and generated compressed third harmonic pulses of an Nd:glass laser.

This technique is based on the decomposition of the input pulses into its spectral components through the use of a diffraction grating, and then imaging of the diffraction grating onto the nonlinear optical crystal. Thus, the SF pulse is produced by a short tilted pulses, as is illustrated in fig. 1.4. The SF has to be directed onto another grating to cancel the angular dispersion and the pulse front tilt.

The change in group velocity Δv_g arises from lateral walk-off of the extraordinarily polarized pulse and can be calculated by

$$\Delta v_g = v_g \tan\rho \tan\alpha, \tag{1.15}$$

where ρ is lateral walk-off angle and α is the pulse tilt angle. GVM achieved by this effect is usually larger than the GVM occurring naturally, caused by dispersion.

Another method to change the GVM is based on a noncollinear scheme [55], which was designed as a GVM compensating scheme for Ti:sapphire laser with a wavelength of 800 nm and pulses shorter than 100 fs. This method is similar to that of tilting pulse fronts, but the effective group velocities in the nonlinear optical crystal are changed through the variations of the propagation angle and pulse front tilt of each of the input pulses. Thus, this method is useful even for the type I phase-matching schemes, as one can change the effective group velocity of ordinarily polarized pulses. This method also requires dispersion elements like diffraction gratings or prisms, but they have to be distinct for each input pulse – more dispersion elements are needed than for the case of tilting of the pulse fronts. Other theoretical investigations of noncollinear SFG and pulse compression are presented in [56, 57]. This method was experimentally

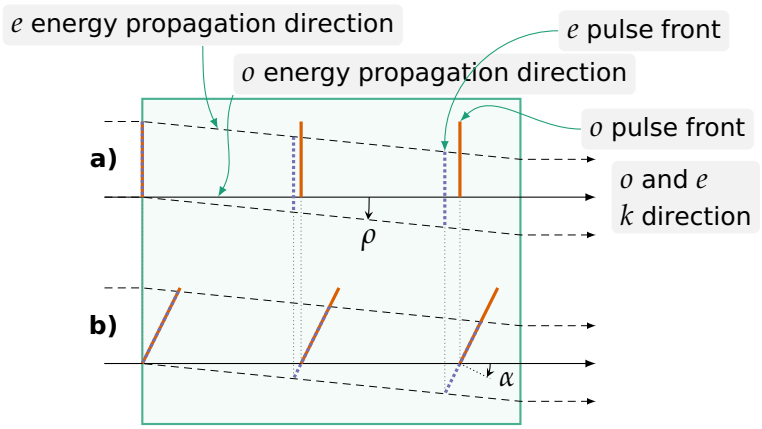

Figure 1.4: Geometrical illustration of a temporal walk-off compensation by tilting of the pulse fronts by an angle α in respect to the phase fronts, which remain perpendicular to the crystal input face. Three distinct positions in the crystal are shown. Dotted purple line is extraordinary polarized slower pulse with spatial walk-off angle ρ, orange solid line is ordinarily polarized faster pulse. Without pulse tilting (a), the pulses separate as they propagate through the crystal (green box). With tilting (b), spatial walk-off contributes to the group velocity and compensates for the temporal walk-off – there is no separation in time and the pulses stay overlapped in time, when propagating.

tested in Refs. [57, 58], and it was also used recently to increase the efficiency in fifth harmonic generation [59].

All the above mentioned papers typically report on the energy conversion efficiency, intensity conversion efficiency, pulse compression, spectral profile and also limited temporal pulse profile of the SF pulse. The beam profile and beam quality of the SF pulse are not considered, except for the papers from my group. However, the degradation of the beam quality and the deterioration of the beam profile is a serious issue severely limiting possible applications, and is of particular concern in those schemes, where back-conversion plays an important role, as the intensity and the rate of back-conversion is different in various parts of the laser beam.

1.4.4 Realization of pulse-front tilting

A tilting of the pulse front can be realized by means of prism or diffraction grating. In a prism, the pulse front will lag behind in the thicker part of the glass, causing the tilting in respect to phase fronts and propagation direction.

The tilting can be calculated from [60]

$$\alpha_0 = \arctan\left(\lambda \frac{\mathrm{d}\varepsilon}{\mathrm{d}\lambda}\right), \tag{1.16}$$

where

$$\frac{\mathrm{d}\varepsilon}{\mathrm{d}\lambda} = \frac{a}{b}\frac{\mathrm{d}n}{\mathrm{d}\lambda} \tag{1.17}$$

is the angular dispersion, n is the refraction index, λ is the wavelength and $\lambda \frac{\mathrm{d}n}{\mathrm{d}\lambda}$ is typically 2 to 15 % for commercially available prisms and considered wavelengths. Parameters a and b are related to the geometry of the beam and prism, for equilateral prism and angle of minimum deviation, $a/b = 1.14$.

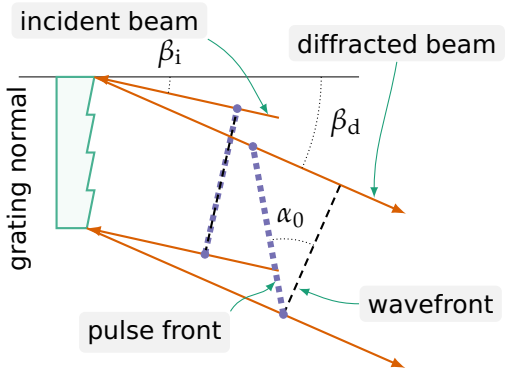

Figure 1.5: Illustration of the pulse front tilt originating after the diffraction at a diffraction grating. Incident beam with an incidence angle of β_i is diffracted at a diffraction grating (green) with a diffraction angle β_d. In the incident beam, wavefront (densely dashed black line) and the pulse front (purple dotted line) is coincident. In the diffracted beam, there is an angle α_0 between the pulse front and the wavefront, so called pulse front tilt.

In a diffraction grating, the part of the beam impinging on the near edge of the grating will precede the part impinging on the back edge [61], as is illustrated in figure 1.5. The angular dispersion of the grating is given by [62]

$$\frac{\mathrm{d}\varepsilon}{\mathrm{d}\lambda} = \frac{m}{d_\mathrm{g} \cos\beta_\mathrm{d}}, \tag{1.18}$$

where d_g is the grating constant, m is diffraction order and β_d is the diffraction angle, and the tilt angle can be calculated again by (1.16). The diffraction angle can be rewritten from diffraction equation as

$$\cos\beta_\mathrm{d} = \sqrt{1 - \left(\sin\beta_\mathrm{i} + \frac{m}{d}\lambda\right)^2}, \tag{1.19}$$

where β_i is angle of incidence.

Now, the second goal of my work becomes clear: **I want to research the possibility of nonlinear pulse shaping and compression of high-repetition-rate high-average-power thin-disk lasers in borate crystals by the means of numerical simulations and experiments.**

I focus on numerical simulations of nonlinear pulse shaping through the second harmonic generation of Yb:YAG laser, while including the important beam properties, in chapter 3 and I describe experiments without tilting of the pulse fronts in chapter 4 and with the tilting of the pulse fronts in chapter 5.

1.5 Experimental data collection and processing methods

Now, I describe the process of analysing the data collected in a typical experiment. The section is subdivided into parts by a type of a measured quantity.

1.5.1 Laser power

Power is typically measured by a power meter from a company Ophir, which can log the data into a text file as it measures them. Offset value, the power measured with the laser turned off, is subtracted from the data. To lessen the influence of power instability of the laser, it is advantageous to measure the power across at least 10 s. One can then load all the measured data and calculate the mean and standard deviation. Between ten and a low hundreds samples can be measured per second. The mean $\bar{A}$ and standard deviation σ_A of an N number of measurements A is calculated by

$$\bar{A} = \frac{1}{N}\sum_{i=1}^{N} A_i, \tag{1.20}$$

$$\sigma_A = \sqrt{\frac{1}{N-1}\sum_{i=1}^{N}(A_i - \bar{A})^2}. \tag{1.21}$$

The calculated value of power can then be reported as $(\bar{A} \pm \sigma)$ W or other units.

When calculating power conversion efficiency η, the standard deviation is propagated by means of propagation of uncertainty by following equations:

$$\eta = \frac{P_{\text{out}}}{P_{\text{in}}}, \tag{1.22}$$

$$\sigma_\eta = \eta \sqrt{\left(\frac{\sigma_{P_{\text{in}}}}{\bar{P}_{\text{in}}}\right)^2 + \left(\frac{\sigma_{P_{\text{out}}}}{\bar{P}_{\text{out}}}\right)^2}. \tag{1.23}$$

1.5.2 Laser spectrum

The spectrum is typically measured by a spectrometer from a company Ocean Optics or Narran. Part of the laser beam is sent into an integration sphere, which will diffuse the laser beam, preserve the spectral information and destroy the spatial dependence of the spectral intensity profile $I(\lambda)$. The light from integration sphere is sent to the spectrometer by means of an optical fibre with a flat spectral transmission curve.

When evaluating spectrum, multiple parameters can be observed. The four most important are:

1. Position of the peak, or the wavelength λ, at which the spectral intensity $I(\lambda)$ is at its maximum.

2. Width of the spectra peak calculated at half of the maximum, so called FWHM spectral width.

3. Position of the centre $\tilde{\lambda}$, calculated from the first moment of the spectral intensity profile. The data are normalized[‡] and integration region is chosen. First, the data can be clipped symmetrically around the position of the peak and the range is at least ten times that of the FWHM on each side. Then, the position of the centre can be calculated from equation

$$\tilde{\lambda} = \frac{\int_{-\infty}^{\infty} \lambda I(\lambda)\,\mathrm{d}\lambda}{\int_{-\infty}^{\infty} I(\lambda)\,\mathrm{d}\lambda}. \tag{1.24}$$

4. Width of the spectral profile calculated from second moment, which will take pedestals and all other features below the half of the maximum level

[‡]Normalization in this case is not done by subtracting minimum and then dividing by maximum. Instead, mean of the few first and last values is subtracted and then the data are divided by maximum. Values, which do not hold any information and are only noise should be chosen for the minimum subtraction. This will ensure, that the integral of the noisy background yields zero.

into account. This $D4\sigma$ width can be calculated from

$$D4\sigma = 4\sqrt{\sigma^2}, \tag{1.25}$$

where

$$\sigma^2 = \frac{\int_{-\infty}^{\infty} \left(\lambda - \tilde{\lambda}\right)^2 I(\lambda)\,\mathrm{d}\lambda}{\int_{-\infty}^{\infty} I(\lambda)\,\mathrm{d}\lambda}. \tag{1.26}$$

The farther away one is from the $\tilde{\lambda}$ position, the more significant is all the noise in the measured profile. One can be either satisfied with thus obtained $D4\sigma$ width, but it is often better to calculate the first and second moments iteratively, with adjustment made to the integration region in every iteration so that the region is equal to the $3 \times D4\sigma$ value. This means, that in every iteration, after the $D4\sigma$ calculation, new integration bounds are chosen to be $\tilde{\lambda} - 1.5 \times D4\sigma$ and $\tilde{\lambda} + 1.5 \times D4\sigma$. The iteration continues till convergence, when the $D4\sigma$ value does not change in between iterations. In case of a Gaussian spectral profile, the $D4\sigma$ width is the same as the width at the level of $1/\mathrm{e}^2$ of maximum.

One can convert the wavelength λ to the frequency ν by using

$$\nu = \frac{c_0}{\lambda}. \tag{1.27}$$

Next, one can calculate the Fourier transform (FT) limited pulse, by taking the spectral intensity profile, assuming flat spectral phase, and doing the FT. From this FT limited pulse, the minimal pulse duration $\Delta t_{\mathrm{P}}^{\mathrm{min}}$ can be found and the time-bandwidth product (TBP) calculated as

$$\mathrm{TBP} = \Delta\nu \Delta t_{\mathrm{P}}^{\mathrm{min}}, \tag{1.28}$$

where $\Delta\nu$ is the FWHM of the spectral intensity profile in frequency.

1.5.3 Beam profile

To measure the beam profile, I use camera-based beam profilers. One has to sent the laser beam onto the beam profiler chip as perpendicularly as possible, in order for the assessment of the ellipticity to be possible. The beam has to be attenuated to such a level, that the camera is not overexposed, but the exposure time can be still sufficiently high for multiple pulses to average over (and not e.g. 1 ms with a laser running at 1 kHz repetition rate). The camera needs

good background calibration for the exposure time and gain factor used, so no background light gets into the way of beam parameters calculation.

Otherwise, the beam profile parameters evaluation follows the ISO 11146 norm, with few steps for qualitative analysis added.

1. The centroid position of the power density distribution $P(x,y)$ is calculated from first moments similarly to (1.24), but in two dimensions:

$$\tilde{x} = \frac{\int_{-\infty}^{\infty}\int_{-\infty}^{\infty} xP(x,y)\,\mathrm{d}x\mathrm{d}y}{\int_{-\infty}^{\infty}\int_{-\infty}^{\infty} P(x,y)\,\mathrm{d}x\mathrm{d}y}, \tag{1.29}$$

$$\tilde{y} = \frac{\int_{-\infty}^{\infty}\int_{-\infty}^{\infty} yP(x,y)\,\mathrm{d}x\mathrm{d}y}{\int_{-\infty}^{\infty}\int_{-\infty}^{\infty} P(x,y)\,\mathrm{d}x\mathrm{d}y}. \tag{1.30}$$

2. Second moments are calculated by

$$\sigma_x^2 = \frac{\int_{-\infty}^{\infty}\int_{-\infty}^{\infty} (x-\tilde{x})^2 P(x,y)\,\mathrm{d}x\mathrm{d}y}{\int_{-\infty}^{\infty}\int_{-\infty}^{\infty} P(x,y)\,\mathrm{d}x\mathrm{d}y}, \tag{1.31}$$

$$\sigma_y^2 = \frac{\int_{-\infty}^{\infty}\int_{-\infty}^{\infty} (y-\tilde{y})^2 P(x,y)\,\mathrm{d}x\mathrm{d}y}{\int_{-\infty}^{\infty}\int_{-\infty}^{\infty} P(x,y)\,\mathrm{d}x\mathrm{d}y}, \tag{1.32}$$

$$\sigma_{xy}^2 = \frac{\int_{-\infty}^{\infty}\int_{-\infty}^{\infty} (x-\tilde{x})(y-\tilde{y}) P(x,y)\,\mathrm{d}x\mathrm{d}y}{\int_{-\infty}^{\infty}\int_{-\infty}^{\infty} P(x,y)\,\mathrm{d}x\mathrm{d}y}. \tag{1.33}$$

3. From these, beam widths in the laboratory system are calculated as

$$D4\sigma_x = 4\sqrt{\sigma_x^2}, \tag{1.34}$$

$$D4\sigma_y = 4\sqrt{\sigma_x^2}. \tag{1.35}$$

   Now, the laser beam occupies only a part of the camera chip, but the noise far away from the beam centre can dominate the integrals. Because of this, one has to integrate not over the whole chip, but only over a certain integration area. To determine the proper integration area, iterative procedure takes place: In first step, one calculates the integrals and the beam widths over the whole chip, assuming the noise level is small. These beam widths will serve as initial guesses for the approximation of the integration area, which is be defined as a square area with dimensions $3D4\sigma_x \times 3D4\sigma_y$ centred on the beam centroid. Next, the integration is calculated only over this area, and new approximation of the beam widths is obtained. This procedure is repeated until convergence of the beam widths. Notice, that this is virtually the same procedure as in the calculation of the spectral profile parameters.

4. Azimuthal angle, or the orientation of the principal axis of the beam to the x axis of the laboratory system, is calculated by

$$\phi = \frac{1}{2} \arctan\left(\frac{2\sigma_{xy}^2}{\sigma_x^2 - \sigma_y^2}\right), \tag{1.36}$$

if $\sigma_x^2 \neq \sigma_y^2$. Otherwise,

$$\phi = \frac{\pi}{4} \operatorname{sgn} \sigma_{xy}^2. \tag{1.37}$$

5. The beam widths in the direction of the principal axes of the beam profile are given by equations

$$D4\sigma_{xe} = 2\sqrt{2\left[\sigma_x^2 + \sigma_y^2 + \gamma\sqrt{\left(\sigma_x^2 - \sigma_y^2\right)^2 + 4\left(\sigma_{xy}^2\right)^2}\right]}, \tag{1.38}$$

$$D4\sigma_{ye} = 2\sqrt{2\left[\sigma_x^2 + \sigma_y^2 - \gamma\sqrt{\left(\sigma_x^2 - \sigma_y^2\right)^2 + 4\left(\sigma_{xy}^2\right)^2}\right]}, \tag{1.39}$$

where

$$\gamma = \operatorname{sgn}\left(\sigma_x^2 - \sigma_y^2\right). \tag{1.40}$$

The larger of the two widths is then the width of the major axis $D4\sigma_{\mathrm{Maj}}$ and the other one is the width of the minor axis $D4\sigma_{\mathrm{Min}}$.

6. Ellipticity ϵ is the ratio of $D4\sigma_{\mathrm{Min}}$ and $D4\sigma_{\mathrm{Maj}}$ and if it is greater than 0.87, the beam can be regarded as circular and the azimuth angle does not make much sense.

7. Now that one knows all the beam parameters, one can asses, how close the beam profile resembles an ideal gaussian beam, by looking at the root mean square error resulting from the following fitting procedure.

   Because the profile data are in rectangular grid in laboratory coordinates, one should rotate the image by the azimuth angle ϕ, provided that the beam is not circular. This way, the principal axes of the beam will be aligned with the laboratory system. I suggest using rotation with bilinear interpolation method, where the output pixel value is a weighted average of pixels in the nearest 2-by-2 neighbourhood. Before fitting, one should also normalize the beam profile, to be able to compare the fitting errors

across multiple beam profiles. To get rid of a potential noise, which could hinder the normalization, the beam profile can be filtered by a small Gaussian filter.

Now, one can cut the beam profile along its principal axes, the cut should go through the centre of the beam. Both of these cuts (1D vectors) can be fitted with a gaussian profile

$$P(x) = \exp\left[-2\left(\frac{x-C}{D/2}\right)^2\right], \tag{1.41}$$

where C and D are fitting parameters. C is the centre of the Gaussian fit and for symmetric beam, it should correspond to the position of the centroid. D is the diameter of the fitted Gaussian curve. The whole profile can be similarly fitted by a 2D Gaussian profile

$$P(x,y) = \exp\left[-2\left(\left(\frac{x-C_x}{D_x/2}\right)^2 + \left(\frac{y-C_y}{D_y/2}\right)^2\right)\right], \tag{1.42}$$

where the fitting parameters are C_x, D_x, C_y and D_y respectively. The quality of the fit, and thus the similarity of the beam profile to the Gaussian profile, can be assessed from the root mean squared error (RMSE) of the fit defined as

$$\mathrm{RMSE} = \sqrt{\frac{\sum_{x=1}^{N}\left(\bar{P}(x) - P(x)\right)^2}{N}}, \tag{1.43}$$

where $\bar{P}(x)$ is the value of the fit in point x, $P(x)$ is the value of the data in point (x) and N is the number of data points. The lower the value of RMSE is, the more is the beam profile similar to the Gaussian profile.

1.5.4 Pulse autocorrelation

The autocorrelation (AC) of a laser pulse is typically measured with an autocorrelator from a company APE-Berlin. It should be measured with reasonable resolution, depending on the pulse complexity, and averaging of the data should be small enough to quickly see deliberate disruptions, yet large enough for the noise to cancel out. Both the tuning of the nonlinear crystal inside the autocorrelator and the beam alignment should be chosen for the maximum intensity of the AC trace.

To evaluate the AC trace, one can assume either gaussian or sech^2 profile of the laser pulse. If the laser pulse is assumed to be gaussian,

$$I_{\mathrm{P},g}(t) = \exp\left[-2\left(\frac{2\sqrt{\ln(2)}t}{\Delta t_{\mathrm{P},g}^{\mathrm{FWHM}}}\right)^2\right], \tag{1.44}$$

where $\Delta t_{\mathrm{P},g}^{\mathrm{FWHM}}$ is the width of the pulse, the AC trace is also gaussian and can be fitted by a function

$$I_{\mathrm{AC},g}(\tau) = b\exp\left[-\left(\frac{2\sqrt{\ln(2)}\,(\tau+c)}{\Delta\tau_{\mathrm{AC},g}^{\mathrm{FWHM}}}\right)^2\right], \tag{1.45}$$

where τ is the delay acting as the independent variable and the fitting parameters are b, the amplitude, c the position of the centre, and the FWHM width of the AC trace $\Delta\tau_{\mathrm{AC},g}^{\mathrm{FWHM}}$. The width of the original gaussian pulse can be calculated as $\Delta t_{\mathrm{P},g}^{\mathrm{FWHM}} = \Delta\tau_{\mathrm{AC},g}^{\mathrm{FWHM}}/1.41$.

If the laser pulse is assumed to have a shape of the sech^2 function,

$$I_{\mathrm{P},s}(t) = \mathrm{sech}^2\left(\frac{1.7627t}{\Delta t_{\mathrm{P},s}^{\mathrm{FWHM}}}\right), \tag{1.46}$$

where $\Delta t_{\mathrm{P},s}^{\mathrm{FWHM}}$ is the FWHM width of the pulse, the AC trace can be fitted by a function

$$\begin{aligned} I_{\mathrm{AC},s}(\tau) = b\frac{3}{\sinh^2\left(\frac{2.7196\times(\tau+c)}{\Delta\tau_{\mathrm{AC},s}^{\mathrm{FWHM}}}\right)}\times \\ \left[\frac{2.7196\times(\tau+c)}{\Delta\tau_{\mathrm{AC},s}^{\mathrm{FWHM}}}\times\coth\left(\frac{2.7196\times(\tau+c)}{\Delta\tau_{\mathrm{AC},s}^{\mathrm{FWHM}}}\right)-1\right], \end{aligned} \tag{1.47}$$

where again τ is the delay, and the fitting parameters are the amplitude b, the position of the centre c, and the FWHM width of the AC trace $\Delta\tau_{\mathrm{AC},s}^{\mathrm{FWHM}}$. The width of the original sech^2 pulse can be calculated as $\Delta t_{\mathrm{P},s}^{\mathrm{FWHM}} = \Delta\tau_{\mathrm{AC},s}^{\mathrm{FWHM}}/1.54$.

1.5.5 Frequency-resolved optical gating

Autocorrelation requires initial assumptions about the pulse shape to obtain the pulse duration. If the pulse shape is not trivial, as will be the case of

the compressed and shaped pulses generated in my case by the procedure described in section 1.4, method to measure the complex pulse shape is needed. My method of choice is the frequency-resolved optical gating (FROG).

FROG can be measured with the same device as the AC, but instead of a short nonlinear crystal, very thick crystal is used. This way, one can resolve the AC in frequency by fine tuning the angle of the crystal across a range corresponding to the width of the spectral profile and measuring the AC at each crystal orientation. FROG trace is obtained with good temporal resolution (I usually measure with a temporal resolution of 7.5 fs) and a rather low spectral resolution (at best 0.1 nm).

To process the measured FROG trace, I centre the data in AC delay τ by two methods – I calculate a first moment and move it to the zero delay, or I filter the data by a Gaussian filter and I shift the unfiltered data in such way, that the maximum of the filtered data is at zero τ.

These data are then used in a pulse retrieval software from Rick Trebino, available on his website[§], and I will not go into the details of the pulse retrieval algorithm here.

[§] https://frog.gatech.edu/code.html

2 Universal SHG stage for ultrashort pulses

In the following text, I describe the optimization process of the first SHG stage intended for high energies, that I constructed. The text is based on a publication [30], but additional details, which describe the more recent efforts and the state of the current SHG stages, are provided. The optimization process is based on the evaluation of properties of 2H beam generated in 2, 5, and 10 mm thick LBO crystals. I show, that one cannot have an excellent beam quality and high conversion efficiency at the same time. The setup has to be changed according to the experimental needs – easiest is to change the nonlinear crystal to a shorter one, when beam quality is of concern, and slightly longer one, when one needs highest efficiency.

Currently, the SHG stage at Perla B laser system is optimized and characterized. With energy of 8 mJ at fundamental frequency and 1.4 ps long pulses, I routinely achieve 60 % conversion efficiency with beam quality parameter $M^2 < 1.5$ in $18 \times 18 \times 2.5\,mm^3$ LBO crystal. The SHG stage is fully operational, reliable and maintenance-free and is being regularly used for various user experiments, for example multi beam drilling [14]. Setups for third and fourth harmonic generation are being prepared.

SHG stage for the first Perla HRR laser is currently operated by an unqualified customer without any need for maintenance.* The crystal used is 2 mm long LBO, the 2H beam diameter being 2.4 mm with a pulse duration of 0.8 ps. The pulse energy is 0.58 mJ at a power of 35 W with an efficiency of 56 %. The stage was optimized for excellent beam quality, the M^2 being 1.27×1.22 at full power and 1.17×1.13 at 20 W.

2.1 Methods for SHG optimization

The schematic layout of the SHG optimization experiment is shown in fig. 2.1. The first harmonic (1H) beam comes from the Perla B laser system, working

*More information are available in an article (in czech) https://www.isibrno.cz/cs/novy-stroj-umi-obrabet-laserem-zastudena-s-mikrometrovou-presnosti, where are also links to a press release and a radio coverage.

at 1030 nm wavelength with 1 kHz pulse repetition rate. Compressed pulse duration was around 1.9 ps and maximum pulse energy at the time of the measurement was 6.5 mJ. The beam quality was high, with $M^2 < 1.3$.

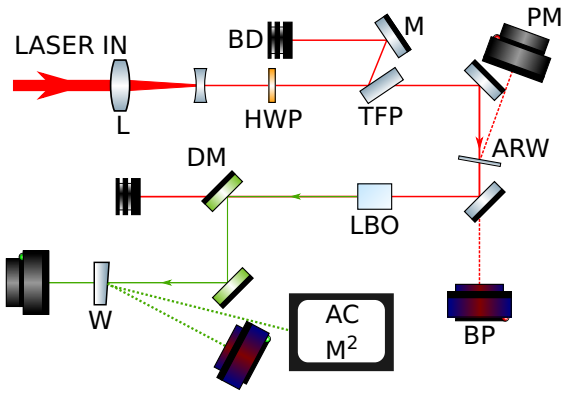

Figure 2.1: Experimental scheme used for frequency doubling experiments. Legend: L – lens, HWP – half-wave plate, TFP – thin film Brewster type polarizer, M – mirror, BD – beam dump, ARW – AR coated window, PM – power meter, LBO – nonlinear crystal, DM – dichroic mirror transmitting first harmonic and reflecting second harmonic, BP – beam profile measurement, W – beam-splitting wedge, AC – autocorrelator, and M^2 – beam quality factor meter.

Firstly, the beam at fundamental frequency enters the Galilean telescope, which adjusts the beam diameter. This is a crucial part of all the SHG stages developed, and it is actually the only part (except for the nonlinear crystal), that is varying across the different lasers lasers. I have found by means of numerical simulations, that there is one overall optimal laser beam intensity and corresponding crystal thickness. Every stage should work at similar peak intensity I_{peak} with similar crystals, which will differ only in the dimensions of their aperture. For higher energies, crystals with larger aperture are needed, because to achieve the same intensity at higher energies, the beam has to be expanded according to the equation 1.12.

Next, a half-wave plate and a thin film polarizer is used to attenuate the power of the 1H beam to allow simple power dependency measurements. This attenuator can also be in front of the telescope.

The power in this particular experiment is measured by a weak reflection of an antireflection (AR) coated window and it is calibrated before each individual measurement. The power meter used was Ophir 3A. Sometimes, it is advantageous to replace the beam dump in the attenuator by a power meter and measure the power without the need for any additional optics in the beam path. This method was used in other experiments.

The input 1H beam profile is measured after the transmission through a high-reflection (HR) mirror, at the same distance, as is the input face of the crystal. As a beam profiler, Spiricon SP620U was used, and the beam diameter was calculated by software BeamGage Standard 6.14 as $D4\sigma$ with Auto-aperture feature on.

After the frequency doubling in an AR coated LBO crystal, the 2H beam at a wavelength of 515 nm is isolated from the 1H beam by two dichroic mirrors. The 2H beam is then splitted by a wedged plate beamsplitter, one reflected part of the beam is used to measure the beam near field profile and the other part is used either for autocorrelation or for M^2 measurement. For autocorrelation, pulseCheck by a company APE-Berlin was used. M^2 parameter was measured by a device supplied by Laser-Laboratorium Göttingen and the measurement followed the ISO 11146 norm.

The transmitted beam was used for power measurements with power meter Ophir F150A-BB-26, and the power is corrected for the losses on the wedged beamsplitter – the beamsplitter was removed for the power calibration.

For the optimization, three LBO crystals were used. All were AR coated for wavelengths of 1030 and 515 nm at input and output faces. Cut angles were $\theta = 90°$ and $\varphi = 12.8°$ for 5 and 10 mm long crystals, and $\varphi = 13.8°$ for the 2 mm long crystal. All crystals had aperture of $8 \times 8\,\mathrm{mm}^2$ and had no temperature control.

For the analysis of the results, which are presented in the next section, I disregarded effects of spatial walk-off, being only 8 µm/mm, as well as of temporal walk-off, which is 53 fs/mm of the crystal length. Section 1.5 provides further details about the data processing.

2.2 Results of SHG stage optimization

2.2.1 Conversion efficiency

First, all three LBO crystals were used and energy conversion efficiency η was measured, to find the crystal with highest attainable output 2H power and satisfactory beam profile. Results are shown in figure 2.2. For these results, the input 1H beam diameter was 3.67 ± 0.15 mm.

For the longer crystals, maximum efficiencies of 75 % and 77 % for 10 mm and 5 mm thick crystals, respectively, were obtained at moderately low input intensities of $4\,\mathrm{GW/cm^2}$ and $15\,\mathrm{GW/cm^2}$, respectively. Above these intensities, back-conversion starts to appear and η decreases. For 2 mm thick crystal the highest achieved efficiency was somewhat lower, 74 % at maximum input 1H power of 5.88 W (corresponding to peak intensity of $52\,\mathrm{GW/cm^2}$), and with

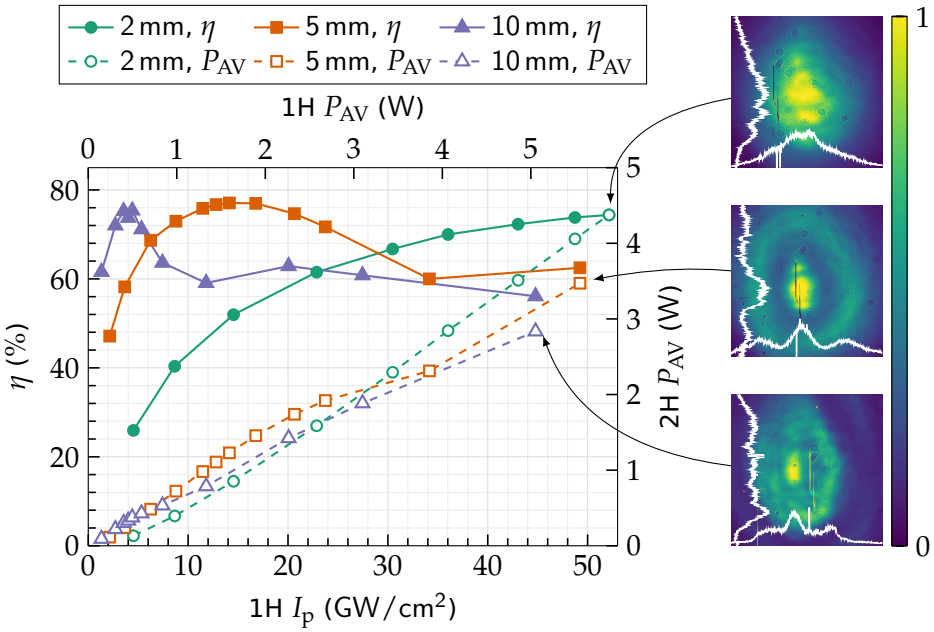

Figure 2.2: Measured dependency of frequency conversion efficiency η and output 2H average power P_{AV} on input fundamental beam peak intensity I_p in LBO crystals of various lengths. Input beam diameter was 3.67 ± 0.15 mm. Left are shown energy fluence profiles of output 2H beams at maximum input power. White lines are sectional views going through the beam centroid.

output 2H power of 4.38 W. This is the highest obtained output power among these crystals. The 2H beam profile is still decent, as is demonstrated by the right part of fig. 2.2, whereas for the longer crystals, the beam profile starts to degrade after achieving maximum η. This degradation occurs due to the back-conversion. First, sharp central peak appears with a ring structure around it. As the back-conversion increases further, the beam gets flatter, with less pronounced peak remaining in the central part.

This insight can be further confirmed by numerical simulations. I calculated numerical simulations in program SNLO, parameters were chosen according to the experiment. The only parameter not directly determined in experiments was phase mismatch Δk, which results for example from natural beam divergence, aberrations caused by imperfect optics, or laser pointing instability. The particular phase mismatch was estimated to be between 0.05 and 0.07 mm^{-1}, the proper phase mismatch for each crystal was chosen based on the similarity of the simulated data to the experimental data. The comparison of numerical and experimental results is plotted in fig. 2.3. The simulations follow the experimental data very well and from this comparison, one can be confident

in the predictive power of the numerical simulations. I write more about the simulation software and parameters in section 3.1.

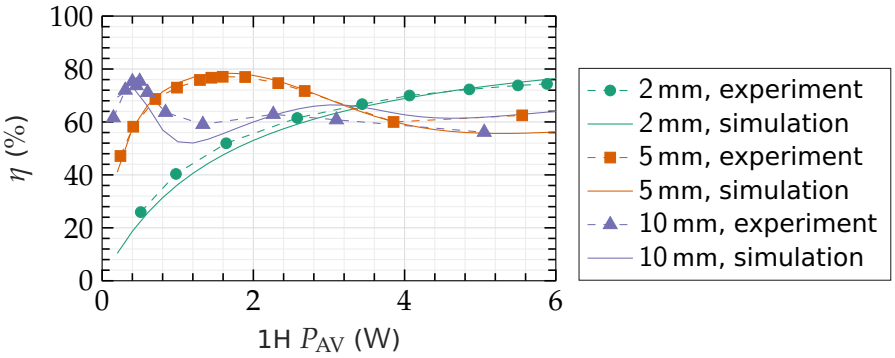

Figure 2.3: Comparison of efficiencies measured in various LBO crystals and numerical simulations calculated in SNLO.

Returning back to the laboratory, **the 2 mm thick crystal was chosen for further experiments, because it has highest potential for high output power while maintaining good beam quality.** To find the limits of the 2 mm thick crystal, I conducted new measurements with an adjusted telescope, decreasing the beam diameter to 0.50 ± 0.01 mm at the crystal input face. This caused an increase in the available peak intensity, even with lower input 1H average power. The beam was divergent after the crystal in order to avoid damage to dichroic mirrors, which have the lowest optical damage threshold, only above 90 GW/cm^2. This value differs based on a supplier of the separators. Note, that the beam was actually astigmatic, so even though it was circular at the crystal input face, it became elliptical upon further propagation.

The results of this new conversion efficiency measurement are shown in figure 2.4. **Maximum efficiency was 80 %** at 252 ± 3 mW of 1H average power (peak intensity was 117 ± 3 GW/cm^2, further in the text called optimal input intensity and rounded up to 120 GW/cm^2), giving 202 ± 2 mW of 2H average power.

2.2.2 Beam profile and quality

Spatial profile of the input 1H beam and the output 2H beam is shown in figure 2.5. Both beams are slightly elliptical and astigmatic. 1H beam has vertical and horizontal diameter of 0.48 mm and 0.52 mm, respectively, in position at the LBO crystal input face. 2H beam is larger due to the divergence of the beam, and has a diameter of 2.0 mm in vertical direction and 2.6 mm in horizontal direction $\approx$ 75 cm after the crystal. The beam is divergent and aberrated to a

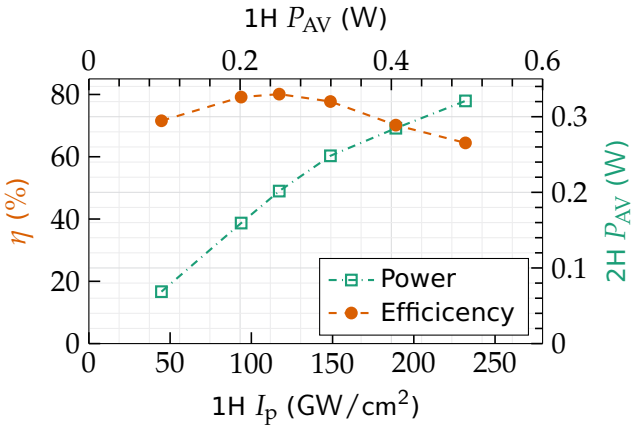

Figure 2.4: Dependency of frequency conversion efficiency η on input 1H peak intensity I_p in the 2 mm thick LBO crystal with smaller beam of 0.5 mm in diameter.

limited extent, which leads to phase-mismatch and, subsequently, drop in a maximum achievable conversion efficiency.

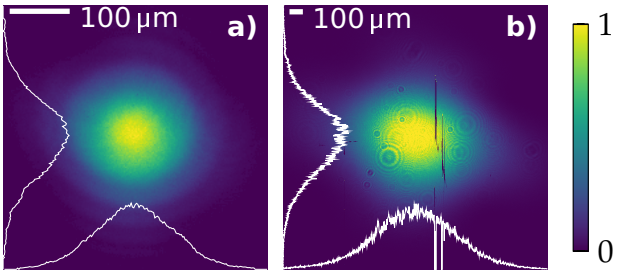

Figure 2.5: Energy fluence profile of the fundamental beam at the crystal input face (a) and of the frequency doubled beam 75 cm after the LBO crystal at optimal input intensity (b). Dark lines in b) are dead pixels of the CCD detector.

As was already mentioned, back-conversion process started by a small phase mismatch introduced by an aberrated beam can lead to decrease in 2H beam quality and η for higher than optimal input intensities. To evaluate this effect, I measured the M^2 parameter of the 2H beam in dependence on input 1H peak intensity. The results, together with beam profiles at various intensities and caustic measurement at optimal input intensity, can be seen in figure 2.6. First, the M^2 rises slowly from the 1.3 value at fundamental frequency with increasing input intensity. **At the optimal input intensity of 120 GW/cm^2, the beam quality is still very good, around 1.5.** But as the intensity increases to more than 150 GW/cm^2, the beam quality factor rises sharply, and the beam profile

gets more asymmetrical. This is caused by the onset of back-conversion above the optimal intensity, which is also confirmed by the numerical simulations.

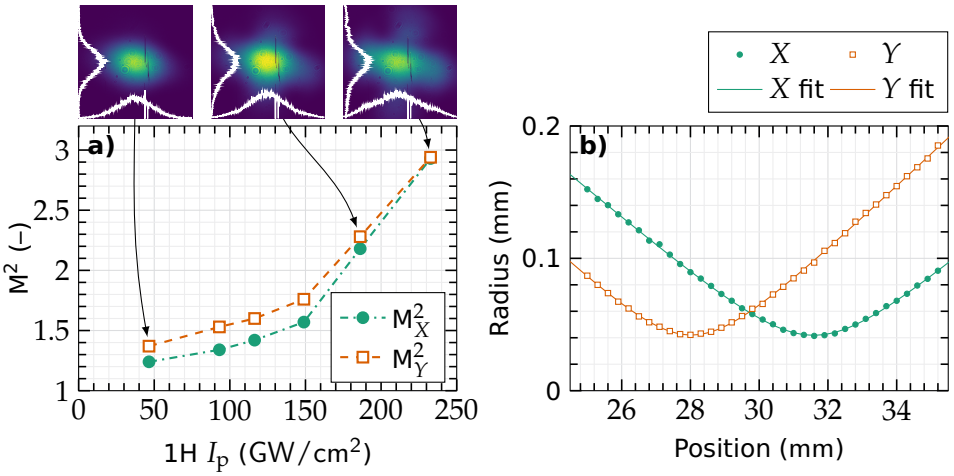

Figure 2.6: M^2 of the frequency doubled beam in horizontal (X) and vertical (Y) direction in dependence on input 1H peak intensity I_p, together with 2H beam profiles 75 cm after the crystal at given intensities (a). Caustic measurement at 120 GW/cm^2 input intensity (b).

2.2.3 Pulse duration and stability

The frequency up-converted pulses are usually somewhat shorter than the input pulses, because the low power edges of the 1H pulse are not converted efficiently. For low efficiency regime and Gaussian pulses, the 2H pulse shortening roughly follows $\Delta t_{2H} \approx \Delta t_{1H}/\sqrt{2}$, where Δt_{1H} is a duration of the 1H pulse. For example, $\Delta t_{1H} = 1.9$ ps results in $\Delta t_{1H} \approx 1.3$ ps. When the back-conversion is present, the 2H pulse can convert back to 1H pulse, starting at the region of maximum intensity and thus distorting the pulse. To determine the pulse shortening effect, as well as the effect of back-conversion, I measured the 2H pulse duration through the means of an autocorrelation. The results are visible in figure 2.7.

Below and at the optimal input beam intensity, the 2H pulse duration is about 1.3 ps, assuming sech^2 pulse shape, which results in lower fit error than using the assumption of Gaussian temporal pulse profile. More on this is in the section 1.5.4. As one exceeds the optimal intensity, back-conversion begins to play an important role. The AC trace starts to differ significantly from the assumed pulse shape and it is not possible any more to make statements about the pulse duration from AC measurements alone. If small phase mismatch

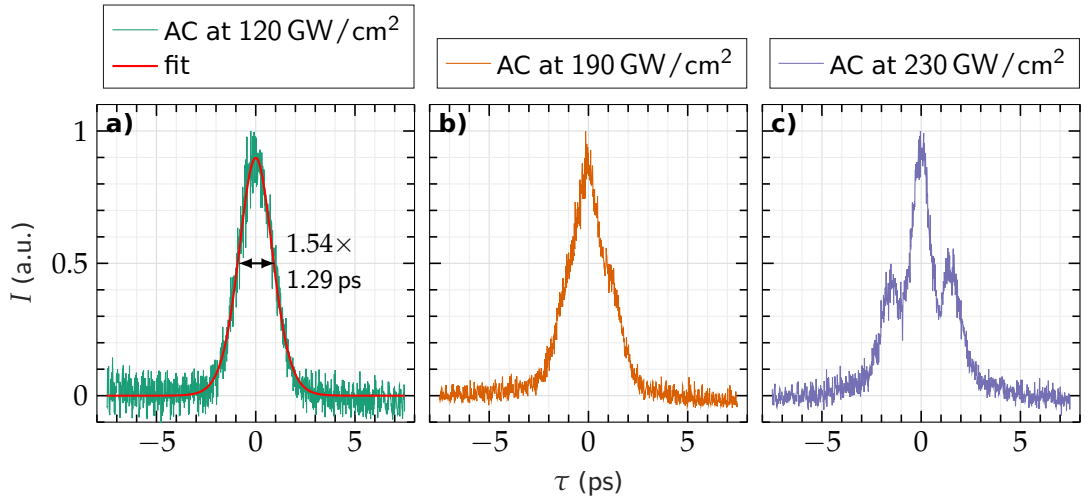

Figure 2.7: Autocorrelation trace of the 2H pulse at the optimal input intensity and fit corresponding to the AC of sech^2 pulse (a). Autocorrelation traces of pulses generated at higher than optimal input 1H peak intensities, i.e. at 185 GW/cm^2 (b) and at 230 GW/cm^2 (c), proving the presence of back-conversion process. I is the normalized AC trace intensity and τ is the delay.

and back-conversion are present, then as the input 1H intensity increases, the most intense part of the 2H pulse starts to convert back to the fundamental frequency. The pulse shapes are becoming more complex, the main peak is reduced and the expected pulse shape is similar to super-Gaussian, or, more roughly, rectangular. AC of rectangular pulse is a triangle, and the measured AC trace shown in figure 2.7b looks accordingly. As the input 1H intensity increases even further, the back-conversion eventually creates a double pulse. That is in agreement with the AC trace divided into three distinct peaks, shown in fig. 2.7c. The two pulses are partially overlapping and the distance between the peaks is around 1.5 ps.

One can also observe spectral profiles at some chosen input intensities, as is done in figure 2.8. As the input intensity and the rate of back-conversion increases, the spectral profile gets wider. Wider spectrum can support shorter pulse, as is evident from the Fourier transform of the spectral profiles. One can see, that the minimal pulse duration for the second harmonic pulse at optimal input intensity is 0.53 ps, so it is almost 2.5fold shorter than the pulse duration I measured by autocorrelation. This discrepancy partially follows from far from ideal compression of the driving laser pulse, where the spectrum also supports much shorter pulse, than what is actually available.

Finally, I measured the 2H pulse-to-pulse energy stability at different input intensities by Gentec Mach 3 energy meter. The energy was attenuated by a half-

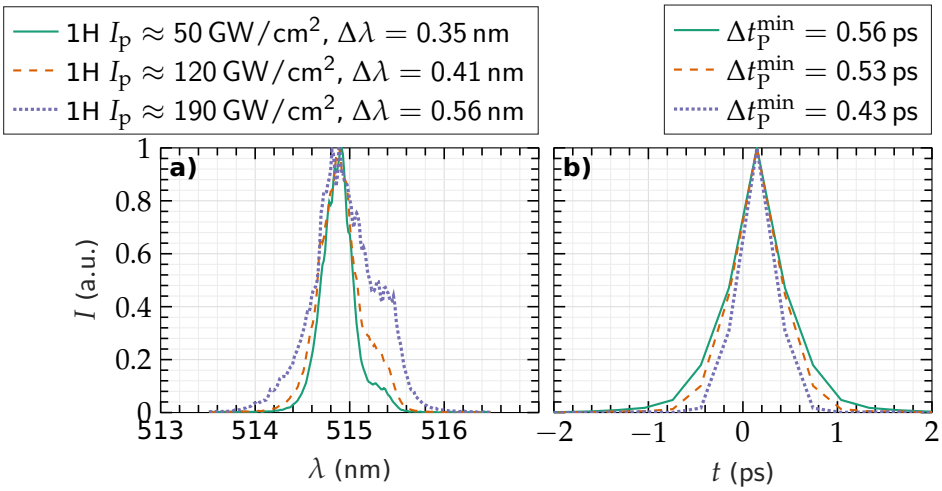

Figure 2.8: Spectral profiles (a) and corresponding transform limited pulses (b) with their FWHM widths at different input peak intensities. I is the intesnity of the profile,

wave plate and a thin-film polarizer, the actual values of energy were different than those presented here. Time series plots and histograms of the energy in the pulses is shown in figure 2.9 and statistically described in table 2.1.

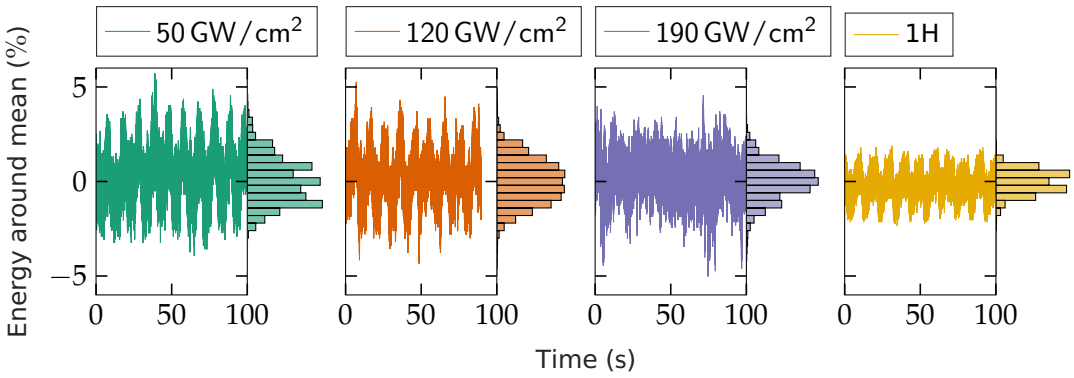

Figure 2.9: Measured pulse-to-pulse energy stability of the second harmonic at different input intensities and the energy stability of the input laser beam at the first harmonic frequency. Time series and corresponding histogram with an amplitude in the horizontal axis are plotted.

The root mean square (RMS) of the pulse-to-pulse energy was only about twice more than that of the 0.6 % RMS of the driving laser, and was slightly dependent on input intensities. At an input intensity of 50 GW/cm^2, the RMS of 2H energy in pulse was 1.2 %. The increase is in accordance with the quadratic dependency of the 2H intensity on the input intensity. At optimal intensity of

Table 2.1: Statistical parameters from the measurement of the pulse-to-pulse energy stability.

1H I_p	50 GW/cm^2	120 GW/cm^2	190 GW/cm^2
# of pulses	100 000	90 000	100 000
Min (nJ)	36.91	32.36	43.29
Max (nJ)	40.62	35.61	47.66
Mean (nJ)	38.42	33.83	45.58
Median (nJ)	38.35	33.79	45.57
Mode (nJ)	38.09	33.92	45.57
Std (nJ)	0.476	0.386	0.457
Std (%)	1.238	1.141	1.003

120 GW/cm^2, the RMS was 1.1 %. At higher intensities, e.g. 190 GW/cm^2, the RMS was again slightly lower, 1.0 %. The reduction of the RMS and increase in stability follows from decreasing slope of the 2H output average power dependency on 1H input average power, as can be seen in figure 2.4, green curve. In simple terms, at higher input intensities, comparable relative variation in the input energy will cause smaller change in the output energy.

This decrease of RMS is also clearly visible from fig. 2.9. In this figure, one can see fluctuations of the pulse energy at the first harmonic wavelength, the most prominent frequency f in the spectrum is 0.1 Hz, evident from the FT shown in figure 2.10. At lower input intensities, the energy of the frequency doubled pulses follows the energy of the original pulse and there is also a peak in the spectrum at 0.1 Hz. Other peaks in the spectrum, although lower, are at frequencies of 50 Hz, 100 Hz and their multiples. They appear already in the driving laser and discussion about their origin is outside the scope of this work. As the intensity is increased, the predictable fluctuations vanish and only noise remains, because in the back-conversion regime, it is amplified by stronger dependency on other non-observed experimental parameters, like beam pointing stability.

2.3 Concluding remarks

In this chapter, I have provided a description of a simple and universal stage for efficient second harmonic generation and I have characterized, how the stage works with one particular laser system. **I have shown, that with a stable and reliable laser source, second harmonic frequency can be generated very efficiently.** Each nonlinear crystal has an optimal input intensity, under which

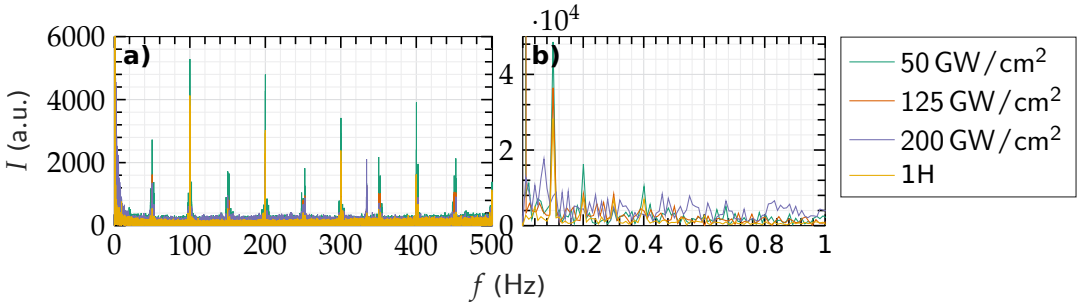

Figure 2.10: Fourier transformation of the pulse-to-pulse energy time series (a) and a zoomed region (b) of the same curves.

it works most efficiently. If one does not need record high efficiency in excess of 75 %, then **I clearly show, that by decreasing input intensity by a means of a telescope and increased beam diameter, or by decreased energy, the second harmonic beam is generated with lower efficiency, but much better beam quality close to the beam quality of the driving laser**. The optimal intensity of each crystal is defined by its material and thickness.

The presented SHG stage is highly universal. For different laser source with higher or lower energy in pulse, it is easy to change the beam diameter by a telescope. The maximal beam diameter is limited only by the clear aperture of the crysal, which can be very large. For example, the frequency conversion stage for the DG laser mentioned in the chapter introduction, with 100 mJ of energy in pulse, needs approximately 1.8 mm thick crystal. The optimal intensity for this crystal, at which the beam quality and the efficiency is balanced, is around 90 GW/cm^2, just below the damage threshold of the harmonic separators. The beam diameter necessary to achieve such peak intensity is around 12 mm ($D4\sigma$), and the crystal should have clear aperture of more than 6σ, or 18 mm. To be on the safe side, I am using crystal with aperture of 24×24 mm^2 and clear aperture of 22×22 mm^2. This is still far from the production capabilities of traditional crystal suppliers like Cristal-laser (France), which can offer apertures of up to 100×100 mm^2. This shows, that the limit for further energy increase is still beyond reach for the current laser sources and there is no engineering obstacle in scaling the frequency doubling stages for higher powers and energies.

In this chapter, I have also briefly shown, that I can simulate the harmonic generation process in SNLO program and that the numerical simulations agree with the experiments well.

There is a multitude of possible applications of an efficient second harmonic generation stage with very good beam quality and picosecond pulses, one example for all is multibeam micromachining [14]. For this application, excellent beam quality is necessary for the diffractive optical element

to work correctly. Nice microholes can be obtained from the diffractive optical element, and high efficiency allows the use of multiple beams (784 in this particular case) to speed up the process considerably.

There is also a possible application of the simple pulse shaping resulting from the back-conversion. The flat-top like or double-peaked pulse can be used for pumping of an optical parametric chirped pulse amplification system [31] to enhance the total conversion efficiency of the OPA process while increasing the available OPA bandwidth.

3 Numerical simulations of pulse shaping

In this chapter, I write about pulse shaping through nonlinear harmonic frequency conversion and about the numerical simulations I calculated with the help of the SNLO software [48].

First, I describe the SNLO software and I asses its applicability to the real world experiments, based on publications and my own experiments. Part of this was already shown in the previous chapter. Next, I have done extensive and numerous calculations to find experimental parameters, with which one could use borate crystals for pulse shaping of picosecond pulses through nonlinear frequency up-conversion. Rest of the chapter is devoted to these simulations. Most of the material in this chapter follows publication [63] and an unpublished poster presented at a conference SPIE Optics + Optoelectronics 2019 held in Prague, Czech Republic, on 1 – 4 April 2019.

3.1 SNLO introduction and verification

SNLO is a simple yet powerful software, which allows one to numerically calculate the frequency conversion process, while taking into account most of the physical phenomena. This software is also useful because of its collection of crystal parameters. I briefly describe the various modules, which are most important and I used them extensively.

3.1.1 SNLO modules

Qmix is a module full of crystal parameters. One can find the transparency range and d_{ijk} matrix of plethora of nonlinear crystals. For chosen crystal, temperature and wavelengths, one can easily calculate the phase-matching angle and the respective d_{eff} of the particular process, together with n, n_g, group velocity dispersion, walk-off, angular and temperature tolerance and mixing strength of the process. This allows one to quickly glance at all the most important parameters, when designing any frequency up-conversion experiment.

Ref. Ind. calculates all the parameters coming from the refractive index with higher accuracy than the Qmix module, and for arbitrary crystal orientation and temperature.

GVM calculates changes in the above-mentioned parameters caused by using pulse-front tilt or non-collinear generation, as is discussed in section 1.4.3.

2D-mix-SP is the most important module for extensive numerical simulations. One has to supply various parameters, which influence the frequency mixing process, the laser and crystal parameters and the grid parameters for numerical simulations, and the software calculates the three wave mixing process. Diffraction, spatial and temporal walk-off, group velocity dispersion, crystal face reflectance, linear and nonlinear absorption, chirp and phase of the laser beams, as well as mutual input beam positions in space and time can all be taken into account. Unfortunately, only (super)Gaussian beams and Gaussian pulses can be used as the input waves. Also, phase mismatch resulting from misalignment or temperature dephasing is represented by a single number. For these two reasons, the software is not very good at simulating third or higher harmonic generation, where the input beam is distorted from the previous frequency conversion and also, the absorption is higher and thermal dephasing is dependent on the process efficiency and is different in every part of the crystal.

For the simulations, I used Matlab SNLO software in version 72.5.2. When calculating the three wave mixing process, I usually disregarded the effects of nonlinear refractive index, two photon absorption and chirp. I assumed the face reflectivity to be zero. I can do this, because at the wavelengths and intensities I am using the higher order nonlinearities do not manifest themselves, I do not have the ability to measure the chirp of the laser, and its influence in the numerical simulations is rather small, and I plan to use crystals with AR coating.

I also assume the crystal losses to be negligible – I sometimes included them in just a few most important results, to check if there is significant difference. I can do this in the numerical simulations, but only because of the limitations of the software. In the software, the absorbed power is just gone from the laser pulse. Since the absorption is low, so is its influence. In the real world, the dissipated energy will heat up the crystal, and because the laser works at high repetition rate, the crystal can heat up considerably, generating thermally induced gradient of the refractive index in the nonlinear crystal. This will prevent proper phase-matching throughout the whole beam aperture, leading to the beam break-up. All this cannot be simulated with the SNLO software, but

that is of no concern in the visible part of the spectrum, where the absorption is usually negligible.

Important parameter not related to the experiment, but affecting the results of the numerical simulations very much, is grid density. At a basic level, number of grid points I used was $256 \times 42 \times 42 \times 35$ ($t \times x \times y \times z$). I then calculated once more with parameters $512 \times 80 \times 80 \times 60$ and compared the results for convergence. If the results were significantly different, or contained obvious numerical artefact, I increased the grid density once more to $1024 \times 128 \times 128 \times 80$. If the results were again significantly different or contained evident numerical artefacts, I threw away the values and did not consider them in the final analysis.*

3.1.2 Comparison of numerical simulations and publications

I have shown in figure 2.3, that after introducing some not well defined phase mismatch, I am able to simulate the curves of efficiencies very well. If I am to simulate pulse shaping, I would like to be sure, whether I can also simulate pulse compression.

The graphs of pulse durations I successfully recreated with numerical simulations are shown in figure 3.1.

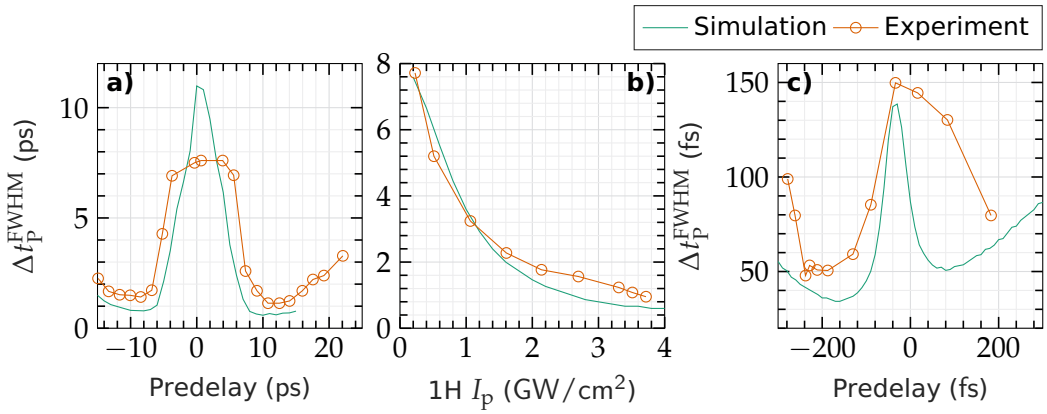

Figure 3.1: Comparison between my numerical simulations and results obtained from literature – (a) [35, Fig. 1], (b) [35, Fig. 3] and (c) [42, Fig. 1].

First is a publication [35], where the authors compressed 12 ps long pulses in KDP crystal. Although the energy and the exact pulse duration used to

*As a side note, one numerical simulation with one set of input parameters took tens of second at the basic level, and more than 30 minutes at the highest density level.

obtain the figures is not described in the paper, I was able to recreate the 2H pulse durations well by choosing the maximal energy and maximal input pulse duration. Other parameters can be found in the paper. I was not able to recreate the efficiency curve in [35, Fig. 3], the calculated efficiency was much higher.

Other graph I was able to recreate is [42, Fig. 1], where the authors compressed fs pulses in BBO. They do not state the pulse duration of one of the input pulses and measure the resulting pulses by autocorrelation. Simulations show a little shorter pulses than those measured, but the general trend kind of follows. Again, I was not able to recreate the efficiency curve in the same picture – the calculated efficiency was around seven times higher, but with identical trend.

I also tried to recreate [38, Fig. 5], again with pulse durations very similar and conversion efficiencies too high. I was not able to recreate results from [44, Fig. 3] or [36, Fig. 2 and Fig. 5] at all.

Most of the times, the discrepancies can be attributed to incomplete description of the experimental conditions. Especially, nowhere in the selected papers are there any mentions about the beam quality. In simulations, I assume perfect Gaussian beam, which can lead to much higher efficiencies than for worse beams. I also suspect, that flat-top beams could have been used in some of the papers. Anyway, **the simulated trends in the pulse durations of the generated pulses followed the reported experimental data well and referring also to the comparison made in figure 2.3, I am confident in the predictive power of the numerical simulations.**

3.2 Overview of the borate crystals

Now, I will present an overview on the nonlinear borate crystals, which could be potentially used for nonlinear pulse shaping and compression. I consider collinear non-tilted SHG in borate crystal cut for type II phase matching, but I will also comment on some general attributes of the crystals.

The laser beam with a wavelength of 1030 nm will be split into two orthogonally polarized parts and up-converted into 515 nm wavelength. BBO is a negative uniaxial crystal, where $n_e < n_o$ and extraordinarily polarized pulse has higher phase velocity than ordinarily polarized one. For the biaxial crystals LBO and bismuth borate (BiBO, BiB_3O_6), $n_f < n_s$, where subscript f means faster component in terms of phase velocity and subscript s means slower component. The basic parameters of these commercially available and convenient crystals are summarized in tab. 3.1.

The first row in the table shows the wavelength and the polarization of the interacting pulses. The second row is the refraction index and the third is a

Table 3.1: Selected parameters of different crystals cut for type II phase matching used for simulations at 293 K, taken mainly from SNLO. n is the index of refraction, n_g is group velocity index, ρ is spatial walk-off, GDD is group delay dispersion, θ and φ are phase-matching angles, d_{eff} is effective nonlinear coefficient and μ_{A} is absorption coefficient. The band-gap values are taken from [64, 65].

parameter	LBO			BBO			BiBO		
wave	1030_f	1030_s	515_f	1030_e	1030_o	515_e	1030_f	1030_s	515_f
n	1.565	1.594	1.580	1.617	1.655	1.636	1.785	1.862	1.824
n_g	1.582	1.614	1.611	1.636	1.675	1.682	1.817	1.897	1.928
d_{eff} (pm/V)		−0.613			1.38			2.22	
GDD (fs^2/mm)	20.9	19.9	82.2	39.8	47.5	126.7	99.0	114.9	326.5
θ, φ (°)		25.4, 90			33.7, 0			55.5, 0	
ρ (mrad)	0	7.08	0	68.54	0	70.53	0	83.81	0
μ_{A} (cm^{-1})	0.0006		0.0202	0.0015		0.0028	0.0087		0.0487
band-gap (eV)		7.78			6.43			< 4.3	

group velocity index, with which one can calculate the group velocity by using $v_g = c_0/n_g$, where c_0 is the speed of light in vacuum. The difference between the fastest and the slowest group velocity is the smallest in LBO crystal and the largest in BiBO crystal. Higher difference should generally increase the magnitude of the pulse compression, but only in the case, in which group velocity of the SF pulse is close to the arithmetic mean of group velocities of input pulses. This condition is met in neither crystals, but LBO crystal is the only one, in which the group velocity of the SF pulse is in between the group velocities of the fundamental pulses.

The next row shows the effective nonlinear coefficient, which is responsible for the strength of the energy exchange. As such, the higher the absolute values, the better. From this point of view, BiBO crystal looks the most favourable. However, it is worth noting, that larger d_{eff} means shorter optimal thickness of the crystal, so the difference between group velocities should be greater.

Group delay dispersion should be low to limit the pulse spreading, but for ps pulses and crystals shorter than 1 cm, these values are negligible. Phase matching angles θ and φ are presented for completeness.

To assess the importance of the lateral walk-off ρ, one first needs to estimate the input beam diameters. From literature, one can expect intensities between 10 and 50 GW/cm^2. For a Gaussian beam, the intensity is calculated by equation

(1.12). Assuming an energy in the pulse of 1 mJ[†] and FWHM pulse duration $\Delta t_{\mathrm{P}}^{\mathrm{FWHM}} = 2\,\mathrm{ps}$, one would need a beam diameter of 3.5 mm to get an intensity of $10\,\mathrm{GW/cm^2}$ and 1.5 mm to reach $50\,\mathrm{GW/cm^2}$. With walk-off 84 mrad in BiBO, which is the highest among the considered crystals, there is a lateral displacement of the beam of 0.84 mm after 1 cm of propagation in the crystal. This is possibly half of the beam diameter and it will have harmful impact on resulting beam profile and beam quality. In BBO crystal, the walk-off is only slightly lower and is also of concern. In LBO crystal, ρ is negligible. For tilting of the pulse fronts, the spatial walk-off is one of the defining parameters in changing the effective v_g (see eq. (1.15)). Therefore, one can expect only a limited control over the group velocities for the LBO crystal, but BBO and BiBO crystals should be suitable for this method of group velocity control.

The second to last row is the linear absorption coefficient, which is the highest in BiBO crystal, where 4 % of the frequency doubled radiation is absorbed in 1 cm thick crystal. This is a lot, and another issue with BiBO crystal is two-photon absorption, as can be seen from the last row. The band-gap in BiBO crystal is 4.3 eV or less, the lowest value of the three crystals, and the energy of 515 nm photon is 2.4 eV – two photons can cross the band-gap and get absorbed. High linear absorption can be a problem for long-term high-average-power operation, and nonlinear absorption poses problems, when high intensities like those considered are used. Indeed, authors of [65] reported high temperature increase from room temperature to 421 K and temperature gradient of 16 K across small and thin BiBO crystal ($1 \times 1 \times 0.4$ mm) under illumination from green high-power laser. For comparison, 1 mm thick BBO crystal under the same conditions heated itself to 300 K with temperature gradient below 0.5 K. In thicker crystals, the expected temperature gradient will be even larger and phase-matching much harder to achieve. Thus, **for high-power applications, BBO crystal with the lowest absorption is preferable.**

3.3 Pulse shaping through back-conversion

In order to verify whether it is possible to achieve significant pulse shaping and pulse compression by SHG in mentioned crystals, I conducted extensive numerical simulations with multiple varying parameters. First, the predelay of the faster pulse has to be scanned together with the crystal thickness. Other variable parameters are the total intensity (energy and diameter) and the ratio of

[†]The experiments will be conducted on Perla B laser system, where the achievable energy is around 10 mJ at 1 kHz. To measure the temporal profile of the output pulse using FROG from company APE Berlin, I need at least 10 kHz repetition rate, so the maximum energy is 1 mJ.

intensities in input pulses. I have chosen laser parameters as follows: 1 mJ input energy and 1.5 ps input pulse duration, with intensity between 7 to 20 GW/cm^2.

To analyse the results, few simple parameters were observed. Firstly, the maps of FWHM of the actual 2H temporal pulse profile, in dependence on predelay and crystal thickness, were studied, together with the maps of conversion efficiency, and two kinds of power: simply calculated $P_{\mathrm{naive}} = E/\Delta t_{\mathrm{P}}^{\mathrm{FWHM}}$, which can be easily measured in an experiment by a power meter and an autocorrelator, and P_{peak} as a maximum power, when plotting temporal output pulse profile, which would have to be measured by e.g. FROG. These powers were then compared to the power of input pulses to assess whether significant peak power enhancement could be achieved. I also calculated pulse duration based on second moments of the pulse profile, called $\Delta t_{\mathrm{P}}^{D4\sigma}$. This width takes into account pedestals regardless of the level at which they appear and as will be clear from the results, this property is of great importance.

The simplest pulse compression scheme operates only with a pulse predelay, which can be introduced by a delaying crystal positioned before the nonlinear frequency doubling crystal. By delaying crystal, I mean birefringent crystal with a sign of GVM between input pulses opposite in respect to the nonlinear crystal.

Before introducing detailed results for one chosen nonlinear crystal, I make some general conclusions and pick some of the varied parameters, which will maximize the output pulse power P_{naive} or minimize the FWHM pulse duration for large range of all the other parameters. **The optimal ratio of input intensities have been found to be $I_{\mathrm{slow}} : I_{\mathrm{fast}} \approx 1.1$, or $\approx 52.5\,\%$ of energy in slower pulse.** With this ratio, the resulting output peak powers were the greatest.

With higher total input intensity, optimal crystal thickness was smaller. It follows common sense, as higher intensity will lead to back-conversion sooner. **For LBO crystal, the total optimal intensity (14 GW/cm^2) was lower and thickness of the crystal larger (7 mm) than for BBO crystal (18 GW/cm^2 and 3 mm)**, because the group velocity mismatch in LBO is smaller. The difference in necessary intensities is rather low, BBO crystal only needs slightly higher intensity for less than half of crystal thickness, but that is caused by double the effective nonlinear coefficient d_{eff}. Optimal thickness of the BiBO crystal is even lower, around 1 mm, and the optimal intensity is again little higher than that of the BBO.

In fig. 3.2 are plotted the results calculated for the BBO crystal. Only these results are presented for the sake of brevity, as they clearly illustrate all the observed phenomena. One can see that there exists an optimal thickness and predelay, marked in the figure by a black or white symbol, for every observed

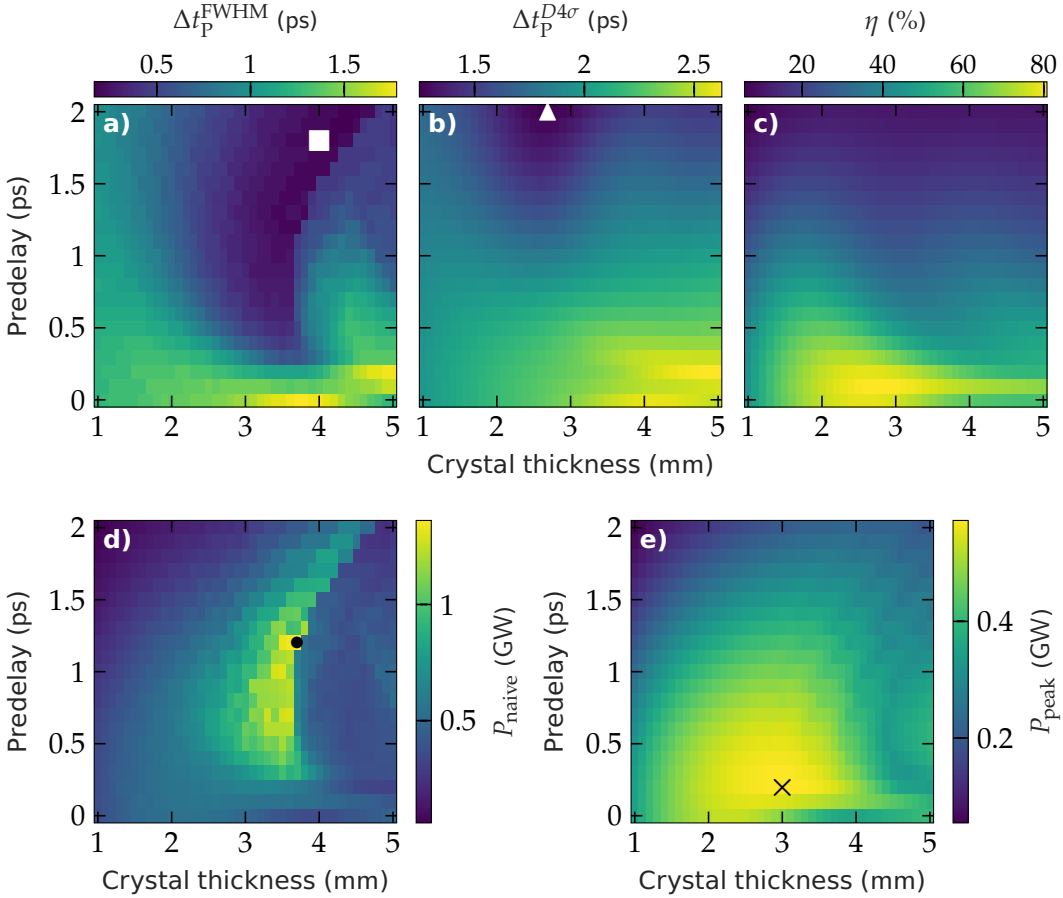

Figure 3.2: Results of numerical simulations of second harmonic pulse shaping through back-conversion in BBO crystal with total input intensity of 18 GW/cm^2 and ratio of intensities $I_{slow} : I_{fast} = 1.1$. FWHM pulse duration Δt_P^{FWHM} (a), 2nd moment pulse width $\Delta t_P^{D4\sigma}$ (b), energy conversion efficiency η (c), power calculated from energy and duration P_{naive} (d) and real peak power P_{peak} (e) in dependence on predelay and crystal thickness is shown. A positive value of predelay refers to the faster pulse trailing the slower pulse. Black and white symbols show the minima and maxima of the plotted parameters, respectively.

parameter. When the predelay increases, the pulse duration by both definitions decreases. As was said earlier, FWHM pulse duration experiences low values, but after exceeding certain crystal length (around 3.5 mm and thicker), the pulse duration rises sharply. Consequently, the exact opposite happens for P_{naive}, which is inversely proportional to the pulse duration. The reason for this is evident from the temporal profiles shown in fig. 3.3a of pulses with lowest FWHM or highest P_{naive}, where there is an energetic pedestal and a small short

peak on top of the pedestal. This peak gets lower with increasing thickness by back-conversion, as can be seen from values of P_{peak} in fig. 3.2e. This short peak will eventually lower so much that the FWHM will start to measure the duration of the long pedestal, and that causes the jump in apparent FWHM pulse duration. Temporal profiles of highest P_{naive} and FWHM are not what I am aiming for.

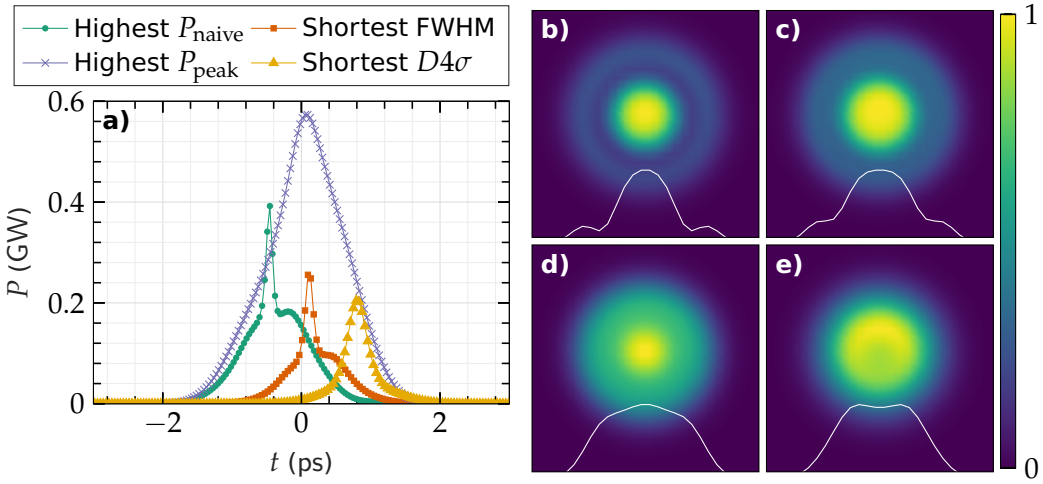

Figure 3.3: Simulated temporal pulse profiles (a) are shown for four distinct cases, together with beam fluences at the output of the BBO crystal: highest P_{naive} (b), shortest FWHM (c), shortest $D4\sigma$ (d) and highest P_{peak} (e). The size of the plotted area is $4.5 \times 4.5\,\mathrm{mm}^2$. The positions of the points in predelay-thickness space are plotted by their respective symbols in fig. 3.2.

If one simply looks at the highest achievable real peak power P_{peak}, one will find a quite long pulse, converted with high (but not record high) efficiency of 76 %. There is almost no compression. **One can find truly short pulse by looking for the shortest 2nd moment pulse duration $\Delta t_{\mathrm{P}}^{D4\sigma}$. This pulse has smooth temporal profile and FWHM of 0.46 ps.** However, the energy conversion efficiency is as low as 11 %.

One can look at the time-bandwidth product as a measure of pulse quality. I calculated the TBP as $\Delta t_{\mathrm{P}}^{D4\sigma} \times D4\sigma_{\mathrm{spectral}}$. The pulse with highest P_{naive} has TBP of 6.1, the pulse with shortest $\Delta t_{\mathrm{P}}^{\mathrm{FWHM}}$ has also high value of TBP equal to 5.4. The other two following cases have much higher quality, meaning lower TBP. The most powerful output pulse with highest P_{peak} has TBP of 1.5 and the pulse with the shortest $\Delta t_{\mathrm{P}}^{D4\sigma}$ has TBP of 1.9.

Energy fluence profiles at the output of the frequency doubling crystal, shown in fig. 3.3, are far from Gaussian, as expected. Temporal profiles of pulses with

highest P_{naive} and shortest $\Delta t_{\mathrm{P}}^{\mathrm{FWHM}}$ (fig. 3.3bc) have pedestal in time domain and their spatial profile has a ring structure, similar to what was observed in figure 2.2. The M^2 parameter of these beams is 2.5 and 2.4 , respectively. The pulse with shortest $\Delta t_{\mathrm{P}}^{D4\sigma}$ has M^2 equal to 1.4, whereas the pulse with highest P_{peak} has M^2 of 1.1 and is closest to the Gaussian beam shape, with only a small dip in the peak. As a remainder, I assumed the input beam was perfectly Gaussian with $M^2 = 1$.

From these numerical simulations, one can see that this pulse compression scheme will only lead to limited results. I reported on the measurements of SHG in BBO crystal with type II phase matching scheme and time predelay in [51] and I will further described it in the next chapter. Short summary follows: I possibly achieved 2.3-fold compression (measured by FROG) with a temporal profile similar to the one in short $\Delta t_{\mathrm{P}}^{D4\sigma}$ regime, and with energy conversion efficiency of 24 %. More probably, I measured the pulse with shape similar to the one observed in the shortest FWHM regime, but with larger pedestal and lower peak. The ambiguity exists because of a low quality FROG trace I measured and analysed. However, the 2H beam was strongly distorted and asymmetric.

Few notes onto the practical aspects of this second harmonic generation and compression regime: To control the predelay in Type II SHG, there are two possibilities. One can use a polarizer to divide the fundamental beam into two perpendicular polarizations. Pulses with one polarization can then be retarded by the use of a delay stage. The two beams then have to be combined in another polarizer. Here, the spatial walk-off pre-compensation can be easily adjusted at the same time. This is the preferred option from a researchers point of view, but requires a lot of optics and space.

The other option is to use a delaying birefringent crystal, which will be simply added into the setup before the nonlinear optical crystal. This method is much simpler, smaller, cost-effective and easier to align, but the available delay is limited by the crystal size. The birefringent crystal can be tilted to slightly adjust the predelay, but for significant changes in predelay, new crystal will have to be used. In principle, two delaying wedges could be used in arrangement similar to Soleil-Babinet compensator, to achieve variable predelay. Spatial walk-off in the birefringent delaying crystal could also be used for walk-off pre-compensation.

The ratio of input intensities can be varied by a half-wave plate before the first polarizer or the delaying crystal.

3.4 Pulse shaping through tilting of the pulse fronts

It is possible to vary the group velocities by pulse front tilting (PFT) by an angle α with an assumption of collinear phase-matching scheme in all mentioned crystals.

In the LBO crystal, the changes in group velocities are rather low because of the small walk-off (see eq. (1.15)). By varying α in range between $-50°$ and $50°$, the absolute value of maximum difference between the group refractive indexes of the input waves n_g^{W1} and n_g^{W2} (GVI difference) is less than 0.05. To put this value in perspective, this translates to temporal walk-off of roughly 1.6 ps/cm of the crystal length. The group velocity of the 2H pulse is still far from the arithmetic mean of v_g^{W1} and v_g^{W2}, which would be optimal and will be called ideal conditions further in the text.

In a BBO crystal, the ideal group velocity conditions can be found, when $\alpha = 23.5°$. At the same time, the GVI difference is 0.09.

In the BiBO crystal, an ideal condition is also met, with GVI difference is even higher, namely 0.22. However, quite large PFT angle of $\alpha = 39.8°$ is needed.

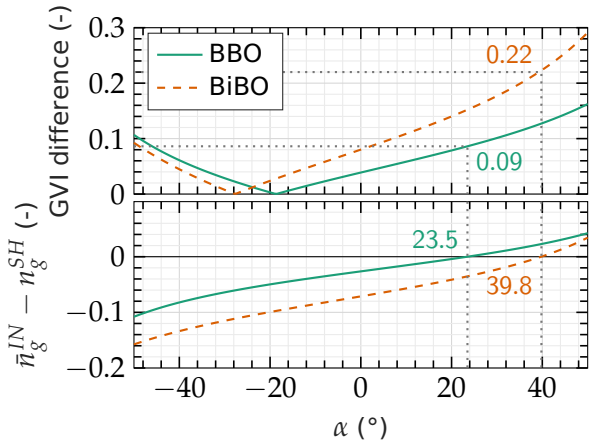

Figure 3.4: Difference between input group velocities (top) and difference between mean of the input group velocity indexes $\bar{n}_g^{IN}$ and the group velocity index of the second harmonic wave (bottom) dependent on the variable tilt angle α.

The difference between group velocities in respect to the tilt angle for BBO and BiBO crystals is shown in fig. 3.4. An important point to note is that these PFT angles are internal angles in the crystal and external tilting angles α_0 can

be calculated using [53]

$$\alpha_0 = \arctan\left(\frac{c_0 \times \tan\alpha}{v_g}\right). \tag{3.1}$$

To achieve $\alpha = 23.5°$ in BBO crystal, one needs external PFT of approximately $\alpha_0 \approx 35°$. This value differs for o and e polarized input pulses by $\approx 1.5°$. For BiBO crystal, the α_0 should be in the vicinity of 58°. In practice, one will tilt both input pulses by the same α_0 angle, because the difference in PFT angle α of few degrees plays negligible role.

Now I will present the results of numerical simulations of SHG in BBO crystal with tilted pulses. I also calculated the simulations for BiBO crystal. The obtained results are qualitatively similar, so I will limit further discussion only to BBO crystal for the sake of brevity. The internal PFT was set to $\alpha = 23.5°$ and other parameters were adjusted accordingly. Since the group velocities of input pulses were now symmetric in respect to the group velocity of the 2H pulse, no asymmetry in input intensities was required. Only predelay, crystal thickness, total intensity and mutual beam displacement was varied.

Before going to the results of calculation, I will again make few general notes. The optimal thickness of the crystal is expected to be longer and dependent on the value of predelay. Since the GVI difference is $|n_g| = 0.086$, one can calculate group length $L_g = \Delta t_{\mathrm{P}}^{\mathrm{FWHM}} \cdot c_0/|n_g| = 5.9\,\mathrm{mm}$ for transform-limited pulse duration of $\Delta t_{\mathrm{P}}^{\mathrm{FWHM}} = 1.7\,\mathrm{ps}$, which is a length over which the pulses have significant overlay. Therefore I shall calculate the simulations for thicknesses up to double that of L_g and predelays at least double that of $\Delta t_{\mathrm{P}}^{\mathrm{FWHM}}$.

The spatial walk-off of 71 mrad reflects to the lateral displacement of 0.85 mm over 12 mm long crystal, so achieving high intensity should be done by increasing pulse energy and not by decreasing diameter, as not to further limit the spatial overlap. Walk-off can be pre-compensated by mutual displacement of the input pulses in the walk-off direction. For the specific L_g, one can expect walk-off pre-compensation in the vicinity of 0.4 mm to be the best for most symmetrical 2H beam and highest efficiency.

I performed extensive numerical simulations, and from the results I make the following conclusions. **The optimal intensity is still around 20 GW/cm^2. Because of the quite large walk-off and long interaction lengths, the highest output power increase can be achieved with the largest considered beam.** Particularly, if one has FWHM beam diameter 2.5 mm and energy 2 mJ and 2.5 mJ, corresponding to an intensity 15.6 and 19.5 GW/cm^2, respectively, one can achieve a slightly higher output P_{peak} than by using beam with 2 mm diameter and 1.5 mJ of energy, corresponding to a peak intensity of 18.3 GW/cm^2. To be more specific, the output power P_{peak} can be five times

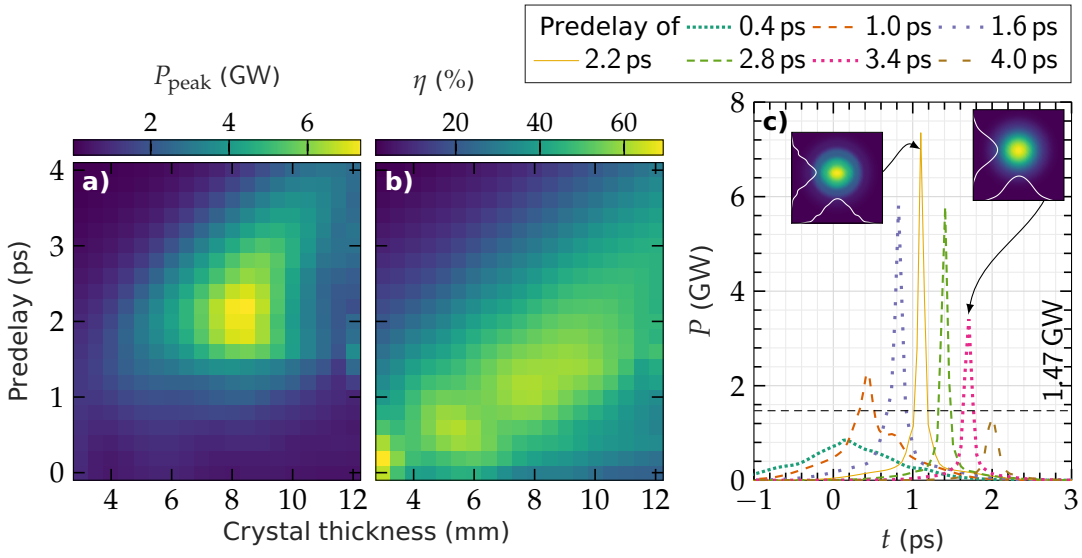

Figure 3.5: Results of numerical simulation of pulse shaping in the BBO crystal, employing group velocity control by tilting of the pulse fronts. A total input intensity of 19.5 GW/cm^2 was used, with input peak power of 1.47 GW. The real output peak power P_{peak} (a) and the energy conversion efficiency (b) in dependence on predelay and crystal thickness are shown. In (c), the temporal profiles of the pulses at different predelays with crystal thickness of 8.5 mm are shown. Two small insets show output energy fluence beam profiles at two indicated predelays. A positive value of predelay refers to the faster pulse trailing the slower pulse.

larger relative to the input power in case of beam with 2.5 mm diameter, and 4.5 times higher, when using beam with FWHM diameter of 2 mm.

The optimal spatial walk-off pre-compensation in this particular intensity range was found to be 0.3 mm. This means that the ordinarily polarized pulse was shifted by 0.3 mm relative to the extraordinarily polarized pulse in the walk-off direction. A misalignment by 0.05 mm worsens the peak power increase only by less than 10 %, but larger misalignments should be avoided.

Fig. 3.5 shows the results of numerical simulations for input energy of 2.5 mJ with FWHM beam diameter of 2.5 mm with input pulse duration 1.7 ps and a peak intensity of 19.5 GW/cm^2. It can be seen that the optimal thickness of the nonlinear crystal is around 8.5 mm. This is more than is the group length L_g, but that was to be expected. Efficient energy conversion starts sooner than when the pulses are half overlapped, as is visible in fig. 3.5c. As the crystal thickness increases, so does the optimal predelay.

There is a large range of predelays and thicknesses, where the FWHM pulse duration is around 0.1 ps. **For the specific case with highest $P_{peak} = 7.35$ GW,**

the predelay is 2.2 ps and the thickness of the BBO crystal is 8.5 mm. The energy conversion efficiency is high, being 48.3 %. The 2H pulse $\Delta t_{\mathrm{P}}^{\mathrm{FWHM}}$ is 87 fs. This means, that I have found parameters, where 5-fold increase in the pulse peak power and 19.5-fold compression of the output pulse in respect to the input pulses can be achieved.

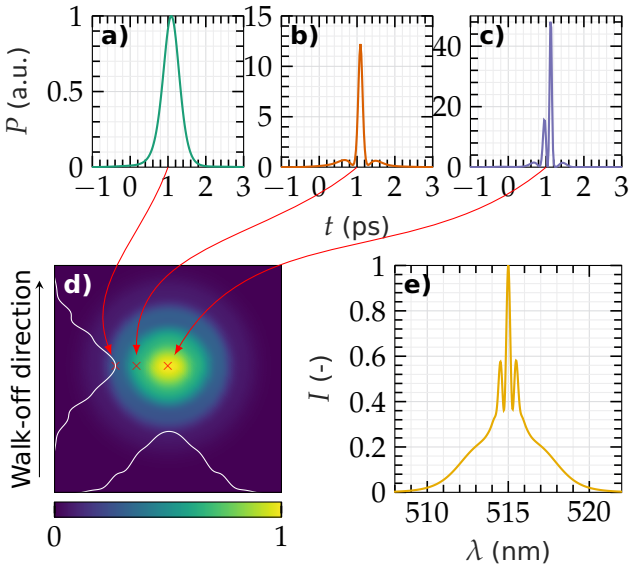

Figure 3.6: Variation of pulse shape (a-c) across beam fluence profile (d) of the pulse with the largest P_{peak} and spectrum (e) of said pulse. The size of the plotted area of the beam fluence profile is $7.4 \times 7.4\,\mathrm{mm}^2$.

The beam profile, together with a spectrum of the output 2H pulse with highest P_{peak}, is shown in fig. 3.6. For illustrative purposes, pulse temporal profiles at various parts of the beam are also shown. At the edge of the beam, the pulse is close to Gaussian. At the center of the beam, two peaks are visible, hinting at back-conversion. The beam profile is only slightly asymmetric, owning to the walk-off pre-compensation. The beam profile is narrower in the walk-off direction and broader in the direction perpendicular to it, the edges have step-like structure and the beam quality is $\mathrm{M}^2 = 3.3$, in which the back-conversion in the central part of the beam plays detrimental role. The spectrum is broadened and has multiple distinct peaks, as was expected, based on the observations in [42, 51]. The 2nd moment spectral width is 8.1 nm.

Looking at fig. 3.5c and comparing to the results without group velocity control in fig. 3.3a, one can see that the short pulses are truly short and intense. There are only very low, but wide pedestals, which then influence the $\Delta t_{\mathrm{P}}^{D4\sigma}$, which is 1.35 ps for the specific case with highest P_{peak}. TBP based on second moments widths of this pulse is 10.8, so very high. That is because even though

the $\Delta t_{\mathrm{P}}^{\mathrm{FWHM}}$ is short, the pedestal is very long. One can calculate by the Fourier transform, the extremely wide spectrum would support pulse as short as 73 fs (FWHM) or 0.56 ps ($D4\sigma$), if it would have flat spectral phase, leading to the lowest possible TBP of 4.5.

Furthermore, the range of predelays and thicknesses where the output 2H pulse is short and intense, is wide, and one can simply vary predelay to obtain less intense pulse, but with higher quality. One can take e.g. pulse with predelay of 3.4 ps, already plotted in fig. 3.5c. This pulse has FWHM pulse duration of 129 fs and efficiency only 19.8 %, but the $D4\sigma$ is less than for the most powerful pulse, being 0.92 ps, and the beam quality is 2.0. The output power is still about two-times higher than the input power. **This means that one can simply change the predelay to switch between more compressed intense pulses and pulses with better beam quality.**

Even when all other experimental parameters are slightly varied, like energy in pulse, diameter or even PFT angle, a compression below 350 fs with at least two times more power on the output compared to input should be achievable.

From these results one can asses, that tilting of the pulse fronts leads to much more significant pulse compression than is the case with pulse shaping through back-conversion. I describe the corresponding experiments in chapter 5. In the experiments, I was unable to measure the pulse shape directly and I did not see expected pulse compression, as measured with autocorrelation. However, I observed beam profile structure, spectral broadening and shape of the efficiency curves very similar to the ones calculated.

Again, few practical notes at the end follow. Remembering the section 1.4.4 in introduction, one can use a prism or a diffraction grating to tilt the pulse fronts. With use of equilateral prism from NSF-11 glass and considering 1030 nm wavelength, the achievable PFT is 2.1°. If the original laser beam diameter is decreased from 12 mm to 1.5 mm, the resulting PFT would be $\approx 16.4°$. Thus, use of two prisms would lead to the angle $\alpha_0 \approx 35°$ desired for BBO nonlinear crystal, but at the expense of non-optimal beam diameter. Achieving tilt large enough for BiBO crystal is not practical by using only prisms – there would have to be even more of them.

The compensation of the tilting of the second harmonic beam is easier, tilt achievable by NSF-11 prism is 8.1°. The beam would have to be resized to 3.5 mm after the crystal in order to change the PFT from $\approx 35°$ to 16.2°, for the compensation with two prisms to be possible.

With a diffraction grating, one can achieve higher PFT more easily. To get $\alpha_0 = 35°$ at 1030 nm, one should choose a grating with 600 lines/mm, as this grating will generate PFT between 35° and 31.8° for all incidence angles between 8 and 90°. At shorter wavelength, higher d_{g} is needed. To compensate for $\alpha_0 =$

35° at wavelength of 515 nm, one should use grating with 1200 lines/mm with β_i anywhere above 15°. One can, of course, image the nonlinear crystal onto the grating by means of a telescope and choose appropriate grating with different parameters. I discuss this in more detail in section 5.1.2.

Both of the mentioned gratings, blazed for the specific wavelengths, are readily available, with efficiencies ranging from 60 % for the polarization parallel to the grooves to 90 % for the polarization perpendicular to the grooves, but higher efficiencies can be achieved per request. Ideally, the grating should be placed before the pulse is rotated and divided into two distinct polarizations, to achieve higher efficiency. When one takes the limited efficiency (assumed to be 80 %) of the diffraction grating into account, one should use around 1.84 GW of input power, or 3.1 mJ instead of 2.5 mJ of input energy. The output power from the whole system will be 5.88 GW instead of the 7.35 GW coming out of the nonlinear crystal and the observed output power relative to the input power will still be increased by a factor of 3.2.

3.5 Few notes on non-collinear regime

There is another method for group velocity control. It is possible to find large group velocity mismatch and ideal conditions assuming non-collinear regime in BBO and BiBO crystals. It is important to note, however, that the effective coupling coefficient of nonlinear interaction d_{eff} can not be calculated by simply following standard equations for interaction with one or two extraordinarily polarized waves, as these were derived for collinear interaction. The values are usually corrected for walk-off, but this correction assumes, that the walk-off angles of all e polarized waves are the same. That is almost universally untrue, but values calculated in this way are better than the ones calculated while omitting walk-off altogether. Walk-off angles are relatively small (84 mrad corresponds to roughly 4.8°) so there is still one propagation direction. In non-collinear mixing scheme, the angles needed to obtain ideal conditions are much larger.

To illustrate the difference between collinear pulse tilting and non-collinear pulse tilting, the GVI differences by PFT in BBO is 0.09. When the titling angle is $\alpha = -37.5°$ and non-collinear scheme is used, the GVI difference is much larger, being 0.49. The correct tilting angle was chosen as follows: I varied the tilting angle and found beam directions, where the group velocity of 2H pulse was the closest to the arithmetic mean of group velocities of the input pulses. For these directions, I also calculated the GVI difference and then I have chosen the tilting angle, where the GVI difference was largest and the 2H group velocity was in ideal condition. In the presented case, the corresponding beam directions are

$\delta = 10.8°$, $\gamma = 10.5°$ and $\theta = 49.7°$ with angle definition following fig. 3.7. Note, that these are internal angles inside the nonlinear crystal. In this way, input beams have mutual angle of more than 21°, which leads to a short interaction length. Therefore, the non-collinear scheme is useful for pulses with durations of no more than hundreds of fs, for which the interaction length is always short. Furthermore, one can expect significant beam distortions.

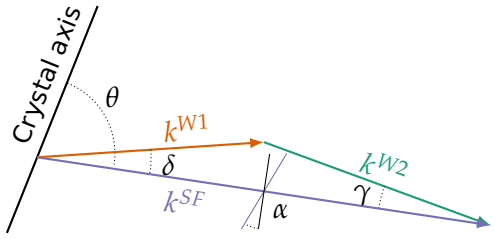

Figure 3.7: Illustration of angles inside the crystal with non-collinear sum frequency mixing scheme, with $W1$ and $W2$ being input waves and SF being the sum frequency wave.

In a BiBO crystal, the v_g values are more favourable – GVI difference of 0.78 can be achieved with tilt of $-49°$ – but the beam directions have still large mutual angle, with $\delta = 9.9°$, $\gamma = 9.2°$ and $\theta = 71.5°$. As a rule of thumb, decreasing the PFT to more negative value increases the GVI difference.

The SNLO software does not support simple numerical simulations of non-collinear three-wave mixing scheme and as such, further pursuit of this group velocity control scheme was suspended in favour of simple PFT, which gives very good results and is more suitable for ps pulses.

3.6 Chapter summary

In this chapter, I presented three methods of nonlinear pulse compression through second harmonic generation.

The use of back-conversion does not lead to optimal results: either the pulse temporal profile has large pedestal, or the energy conversion efficiency is small. Increase in the power cannot be expected. A compression should be possible using non-collinear SHG, and the parameters were presented, but this scheme is more suitable for shorter pulses because of limited interaction length.

A pulse compression with group velocity controlled by the tilting of the pulse fronts appears to be the method of choice, because in 8.5 mm thick BBO crystal one can achieve 5-fold peak power increase with almost 20-fold pulse compression in respect to the input pulses. This

method can be easily scaled to higher energies, if the input intensity around 20 GW/cm^2 is preserved. This optimal intensity is dictated by the differences in group velocities and effective nonlinear coefficient, and is different for other crystals.

The energy conversion efficiency of the 87 fs long output 2H pulse is almost 50 %. The beam quality is rather low, being 3.3, which is caused by back-conversion in the central part of the beam. Nevertheless, the beam profile is still smooth. Using a flat beam should lead to less pronounced changes in the beam profile and quality.

If the need arises, changing the predelay allows one to obtain higher quality beam with an M^2 parameter of 2.0, but with a lower energy conversion efficiency of 20 % and pulse duration of 130 fs. There is again the balance between beam quality and conversion efficiency, as was already observed in chapter 2.

Tilting of the pulse front by 35° necessary for the SHG compression can be easily done and undone by using diffraction grating and imaging optics. There are no substantial technological obstacles preventing the use of this relatively cheap pulse compression method, as it only relies on standard optical elements. It could significantly extend the range of uses of high average power, high repetition rate Yb:YAG thin-disk lasers. I devote the next two chapters to the experiments, which I conducted in order to verify the possibility of nonlinear pulse shaping and compression.

4 Pulse shaping through back-conversion

In this chapter, I present the results of experiments I designed and carried out at the HiLASE centre, the aim of which was to verify the results of numerical simulations and the possibility of nonlinear pulse shaping and compression through back-conversion by delaying one input pulse in respect to the other. Most of these results were presented at CLEO Europe conference in Munich, Germany, on 23 – 27 June 2019 in form of poster [50] and at SPIE Photonics West conference held in San Francisco, USA, on 1 – 6 February 2020 and published in the conference proceedings [51]. They were measured on multiple occasions throughout more than a year. Experiments with tilting of the pulse fronts are described in the next chapter.

4.1 Experimental setup

The experimental setup is shown in figure 4.1. It follows the same principle as the one shown in fig. 2.1, the telescopes and the particular diagnostics are not shown.

The experiments differ by the use of the delay line. The input laser beam at wavelength of 1030 nm is splitted into two parts with orthogonal polarizations. The ratio of the energy between them is controlled by a half-wave plate preceding the beam splitter. The horizontal polarization is predelayed by the means of a motorized linear stage with a mounted retro-reflector, in the figure 2.1 shown as two mirrors.

Next, the polarizations are combined together and aligned into the nonlinear crystal. **Two crystals were used, 3.35 mm thick BBO crystal and 7.43 mm thick LBO crystal, both of them cut for type II phase-matching.** The thicknesses are little larger than the ones chosen in section 3.3 based on numerical simulations, because of the limited precision of the manufacture process. The cut angles of BBO crystal were $\theta = 33.7°$ and $\varphi = 0°$, in accordance with values in table 3.1. For LBO crystal, the cut angles were $\theta = 25.4°$ and $\varphi = 90°$. Both crystals were manufactured by Castech and had AR coating on both faces. Their

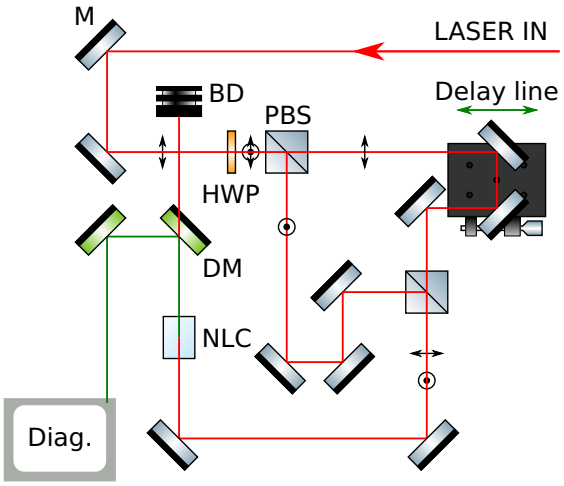

Figure 4.1: Experimental scheme used for pulse shaping experiments with back-conversion as the pulse shaping mechanism. Shown are also the polarization of the laser in different parts along the laser path. Legend: M – mirror, HWP – half-wave plate, PBS – polarizing beam splitter, NLC – nonlinear crystal, DM – dichroic mirror transmitting first harmonic and reflecting second harmonic, BD – beamdump, Diag. – diagnostics like power meter, beam profiler, spectrometer, and autocorrelator/FROG.

aperture was $8 \times 8\,\mathrm{mm}^2$ in case of the BBO crystal and $6 \times 6\,\mathrm{mm}^2$ for the LBO crystals.

The nonlinear crystal is rotated in the horizontal direction to achieve phase-matching. Since the extraordinary polarization is the faster one in the BBO crystal, the horizontally polarized beam should be predelayed – the beam should propagate for a longer time. In LBO crystal, the slow polarization is the one changing with the crystal rotation, so the vertically polarized beam should be predelayed – the horizontally polarized beam should propagate for a shorter time. The positive predelay in units of ps was adjusted for this, with positive value meaning the faster pulse trailing the slower one for both crystals.

Finally, the first and second harmonic beams are separated by a dichroic mirror and the second harmonic beam goes into the diagnostic branch of the experimental setup. This branch consisted of a power meter, beam profiler, spectrometer, autocorrelator and FROG measurement device. The power meters used were Ophir 12A for measurement of the second harmonics and Ophir 30A-BB-18 or L50(150)A-35 for the measurement of the input laser. For some of the spectrum measurements, I used Narran BR8 with a Thorlabs IS200 integration sphere. The spectrometer is designed for the first harmonic frequency – I added a blue coloured glass BGG21 filter and used the spectrometer in a second diffraction order. For the rest of the measurements, this spectrometer was not

available and I had to use a spectrometer from OceanOptics, model USB2+ This device was designed for the proper wavelength, but its resolution was much lower and I did not see as many features as I would like. As the beam profiler, Spiricon SP620U was used, and the autocorrelation, as well as FROG, was measured with APE pulseCheck device.

4.2 Measurements with autocorrelation

First, I will shortly describe my measurements with autocorrelation. The part about LBO was modified from the publication [51] and the BBO part was presented at CLEO Europe conference [50].

4.2.1 Parameters of the driving laser

The driving laser was Perla B laser system running at 1 kHz repetition rate, having at the time of the experiment beam quality parameter $M^2 < 1.2$.

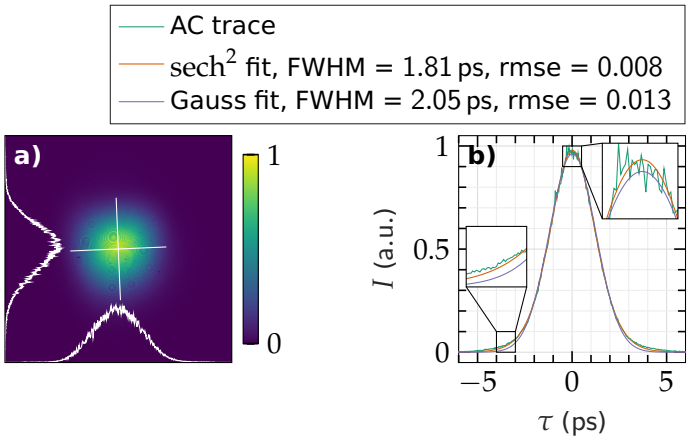

Figure 4.2: Beam profile of the fundamental beam at the start of the experimental setup (a). The area shown is $3.52 \times 3.52\,\mathrm{mm}^2$. The autocorrelation trace (b) with fitted curves and two zoomed regions in the insets, showing the sech^2 fit to be better.

The fundamental beam profile at an input face of the crystal and the autocorrelation is shown in figure 4.2. The width of the beam was 1.49 mm × 1.59 mm in minor and major axis, respectively. For the intensity calculation, I used the beam diameter value of 1.54 mm. The pulse duration was around 2.1 ps, or 1.8 ps, using Gaussian or sech^2 fit, respectively. I would like to remind, that the particular simulations I was trying to verify were calculated using 1.5 ps pulse duration and a peak intensity of $18\,\mathrm{GW/cm}^2$ for the case of the BBO crystal

and 14 GW/cm^2 for the LBO crystal. Experimental intensities are in this region and will be stated with each particular result.

4.2.2 Measurement procedure

First, I have chosen a value of input energy and I have set the ratio of energy between the input pulses. This was done by comparing the power in the whole input beam and the power of the horizontally polarized beam. Next, I measured spectrum, power of the 2H beam, and the autocorrelation while varying predelay of the horizontally polarized beam in a previously specified range. At the end, I measured input energy in pulse again to be sure that it did not drift significantly. Afterwards, I set a new value of the input energy and repeated the measurement.

I varied the predelay around 0 ps value by 20 µm, which corresponds to $\approx$ 133 fs. I measured the position of a zero predelay by the use of a neutral density filter. I measured the absorption of such filter while adjusting predelay, and I assumed, that there will be the highest two-photon absorption at zero predelay – I was looking for a minimum of the transmitted power.

4.2.3 Results from LBO crystal

The efficiencies and pulse durations measured in the LBO crystal are shown in figure 4.3.* One can see, that the efficiency is rather low, with maximum being below 20 %, which is about two times lower than expected, and symmetric in respect to the predelay, which agrees well with the numerical simulations. When one changes the predelay from the optimum value around 0 ps, η decreases. The efficiency is at its maximum already at the lowest input energy around 30 µJ, and with increasing energy it goes even lower. This would point to a back-conversion regime, the onset of which usually occurs at the point of the highest efficiency, as was already discussed in section 2.2.1.

However, if this was the case, one should also see a degradation of the pulse shape, which would be visible in the third map showing RMSE of the autocorrelation fit. This fitting error stays low up to the energy around 110 µJ. The second map shows the width of the pulse $\Delta t_{\mathrm{P}}^{\mathrm{FWHM}}$ calculated from the autocorrelation, and it shows a gentle lengthening of the pulse duration up to the

*Note about the data representation: Previously, similar colourful maps with simulated results were calculated for a regular grid and were displayed in such way, that one pixel with a given colour represented one data-point at the coordinates dictated by the centre of the particular pixel. Now, the grid is not regular, the measured data-points are located at the intersections of the grid lines and the colours in the pixels are interpolated by Goraud shading between these points.

energy of 110 µJ. Due to this fact, I think there is something else causing the efficiency decrease and I am unsure about the source of this problem – it was probably caused by some uncontrolled parameter in the driving laser.

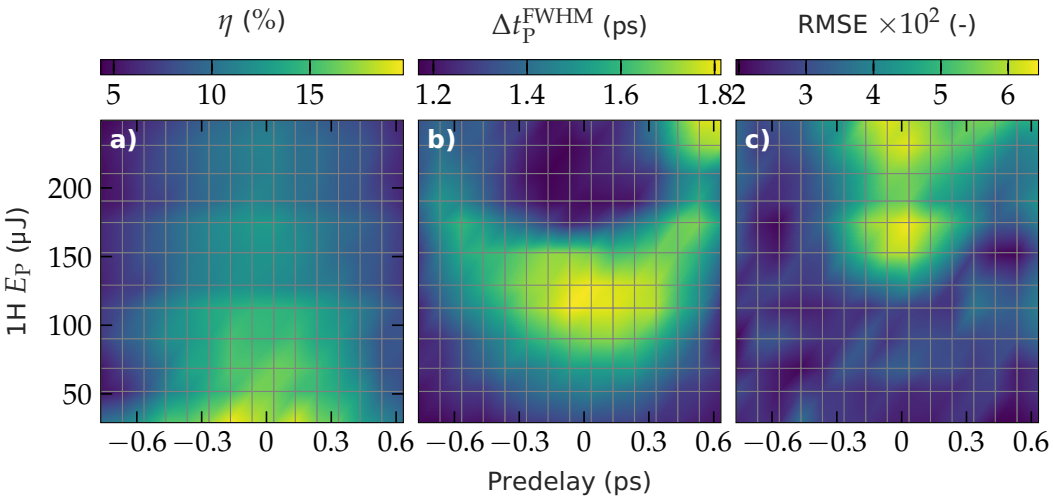

Figure 4.3: Maps of efficiency η (a), pulse duration measured by autocorrelation Δt_P^{FWHM} (b) and error of the autocorrelation trace fit (c) assuming sech^2 pulse shape and measured in LBO crystal, in dependence on predelay and input energy in pulse E_P. The lower energy limit of 30 µJ corresponds to a peak intensity of 1.5 GW/cm^2, upper limit of 250 µJ corresponds to an intensity of 12 GW/cm^2.

The efficiency map seems symmetric in respect to predelay, but this is not the case for the Δt_P^{FWHM} and fitting error map. The pulse duration lowers at higher energies to below 1.2 ps, but from the fit error one can see, that these values are unreliable.

To better see the shapes of the AC traces, I plotted them for one particular predelay in figure 4.4, together with the spectral profiles. First of all, the spectrum gets wider above input energy of 100 µJ, and so is able to support shorter pulse. AC trace gets wider with increasing energy and above 120 µJ, the shape of the AC trace changes from the typical one to a narrow peak and wide pedestal or wings. The FWHM pulse duration is sharply reduced, but the fitting error increases – only the narrower central peak is fitted, and the neglected wings cause the rise in the RMS fitting error.

I also plotted similar graphs in figure 4.5, but now the observed parameters are shown in dependency on predelay for two particular energies – 250 µJ, the highest energy measured, and 100 µJ, the one measured with the highest density of points.

At the lower energy, the pulse duration Δt_P^{FWHM} is longest at zero predelay, only slightly shorter than the duration of the input laser pulse. From the nega-

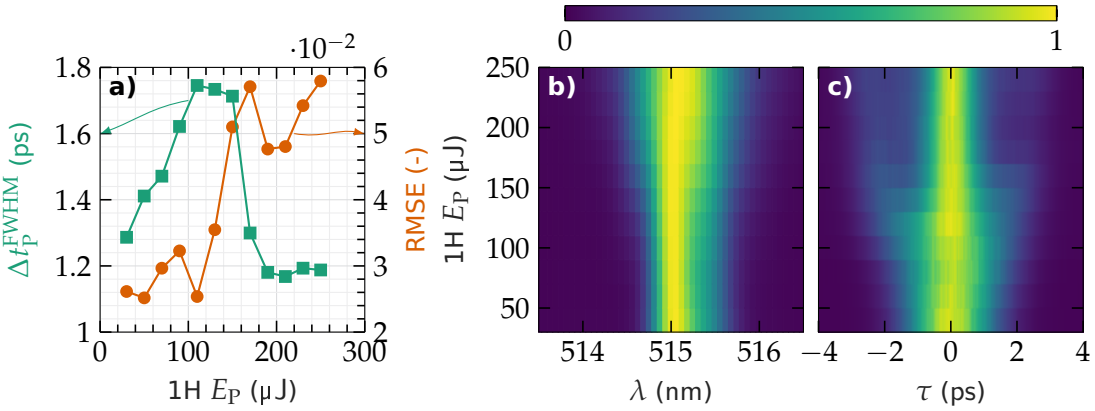

Figure 4.4: Pulse duration Δt_P^{FWHM} with an error of sech^2 fit (a), spectral profiles (b) and AC traces (c) in dependence on input energy in pulse 1H E_P measured in LBO crystal with a predelay of -100 fs.

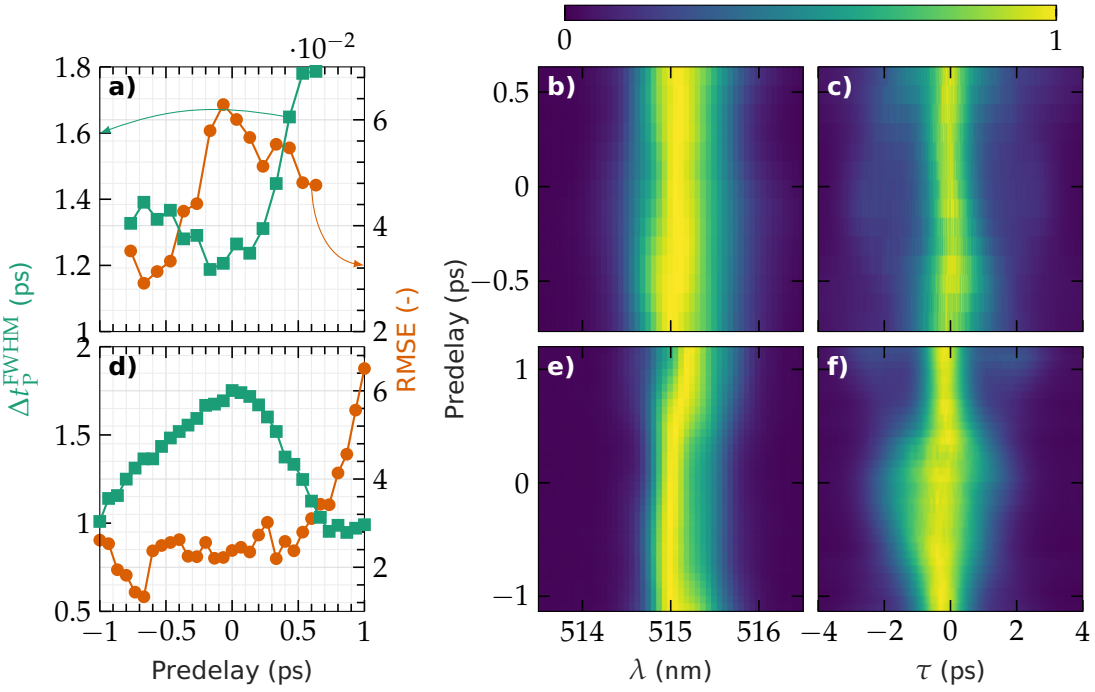

Figure 4.5: Pulse duration Δt_P^{FWHM} with an error of sech^2 fit (a,d), spectral profiles (b,e) and AC traces (c,f) in dependence on predelay measured in LBO crystal with an input energy of 249 µJ (top row, a-c) and 100 µJ (bottom row, d-f).

tive predelay up to the value of around 0.5 ps, the shape of the AC trace looks correctly and the fitting error is small. As one increases the predelay further, there comes the region with the narrow peak and eventually wide wings again. The duration of the central pulse is small and the wings are disregarded in the fitting procedure. The spectrum does not get significantly wider, but the position of the peak is shifted to a longer wavelength.

At the highest energy, corresponding to a peak intensity of $12\,\mathrm{GW/cm^2}$, so still less than the one recommended from simulations, there is no apparent trend in the pulse duration. At negative predelay of less then -0.5 ps, the shape of the AC trace looks like a normal pulse, but with a predelay of more than -0.5 ps, one can see the ongoing back-conversion process and very wide pedestal in the AC traces. At the largest measured predelay, the pedestal is already so pronounced that it is included in the fitting procedure. The spectral profile is much wider than at the lower energy for all the predelays. Due to the fact, that I had to use the OceanOptics spectrometer with smaller resolution, there are no additional features visible in the spectrum. For the measurement of the BBO crystal, I had better spectrometer and I show some spectral features in the next section and figure 4.8.

To sum up the available data on pulse duration: **At lower energies up to some threshold of 120 µJ of energy in pulse, the pulse duration seems symmetric in respect to the zero predelay. At negative predelay, the interacting pulses have shorter temporal overlap and cannot interact with each other fully, causing the reduction in pulse duration. At positive predelay, one can see a creation of a wide pedestal with a narrow peak, which was not expected from the simulations with back-conversion. At higher energies, this pedestal is even more pronounced and the spectrum is even wider, supporting the shorter pulse hypothesis.**

The beam profiles at different energies, plotted in figure 4.6, confirm, that the back-conversion becomes dominant above energy of around 100 µJ, which is a value coincident with the one assessed from the temporal pulse profiles. The degradation of the beam profile does not depend much on the predelay. The astigmatism negatively influencing the ellipticity of the beam, already observed in chapter 2, is also present here.

4.2.4 Results from BBO crystal

I now only briefly present results I measured in the BBO crystal, which are qualitatively the same as the results obtained with the LBO crystal. In the LBO crystal, I measured at lower peak intensities than those calculated. To compensate for that, here I will present data measured with a pulse energy

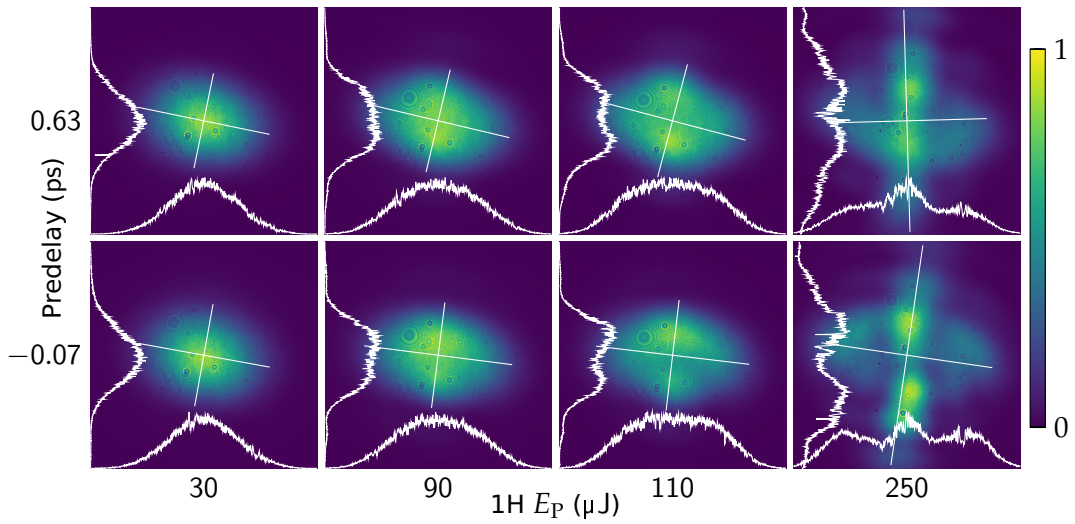

Figure 4.6: Beam profiles at different predelays and different input energies in pulse E_P, measured ≈ 1 m after the LBO crystal. The area shown is $3.52 \times 3.52\,\mathrm{mm}^2$.

of 550 µJ, corresponding to a peak intensity of $26\,\mathrm{GW/cm^2}$, and with a ratio of input intensities $I_o/I_e = 1.14$, or 46.7 % of the power in the horizontal, faster polarization. These results were measured at a different time than the previous ones.

The dependence of energy conversion efficiency and pulse duration on predelay is shown in figure 4.7. The conversion efficiency is the highest at 0.33 ps predelay, corresponding very well to the simulated value of 0.2 ps. The maximum efficiency is 51 %, so very high, especially in comparison with the efficiencies in LBO crystal, although much lower than the simulated 80 %. With increasing predelay, it decreases monotonously. It is also symmetric, the efficiency decrease is the same with increasing or decreasing predelay from the maximum value. This was also observed in the LBO measurement and in the simulations.

At a predelay just below 2 ps, the pulse duration is the lowest, reaching 0.75 ps with a conversion efficiency of almost 15 %. This is in the shortest $D4\sigma$ regime, but the simulated value of the 2H pulse duration was below 0.5 ps, with similar η. With increasing predelay, the apparent pulse duration starts to increase from this global minima, but this is caused by the fitting procedure trying to fit the pedestal, which is starting to appear, and is also visible in the AC trace of the shortest pulse, shown in fig. 4.7b. I have to note, that the RMSE of the fit is always quite high and does not show any particular and easily recognizable trend. Another thing to note is the asymmetry of the AC trace, which becomes more prominent at even higher predelay, with new peak

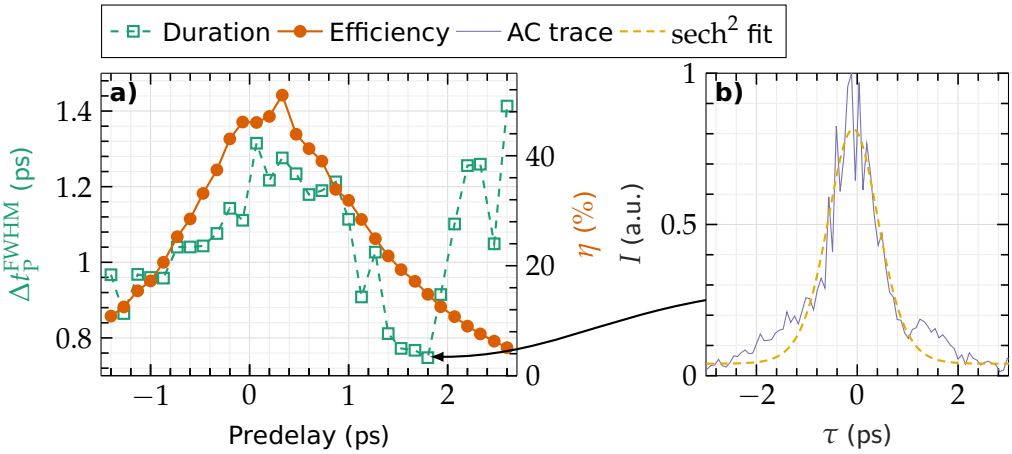

Figure 4.7: Energy conversion efficiency η and 2H pulse duration Δt_P^{FWHM} in dependency on the predelay of input pulses (a) and the AC trace and the fit of the shortest output pulse (b). Fit corresponding to the sech^2 pulse shape was chosen.

starting to appear at the positive side of the autocorrelation delay τ. I discuss the AC asymmetry in more detail in the next chapter in section 5.6.2, since more data and more thorough investigation is presented in that chapter.

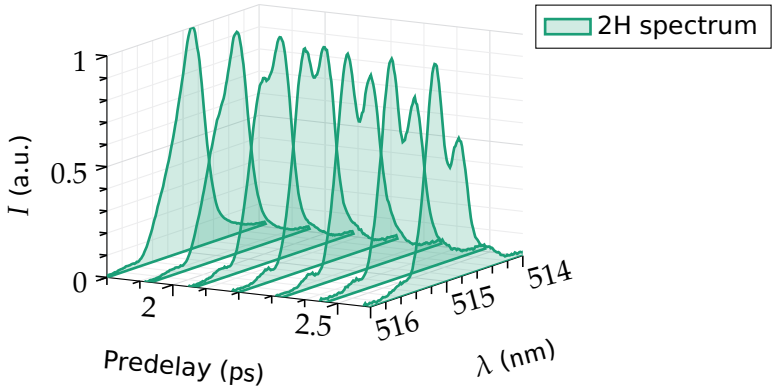

Figure 4.8: Normalized spectrum λ at varying predelay.

The spectral profiles (measured with the Narran spectrometer with higher resolution) are uniform with no significant changes happening up to the predelay of 2.0 ps. Then, **the spectral profiles get slightly wider, asymmetric, and two peaks appear, as is visible in figure 4.8. The intensity gets shifted to a higher wavelength.** Such spectral splitting was also reported in papers [41, 42], and is typical for this pulse compression regime. It does not, however, coincide with the shortest measured pulse. The position of the maximum and of the centre of gravity of the spectral profiles gets shifted to higher wavelength,

as was also apparent in figure 4.5, but without the respective double peaks visible, due to the lower resolution spectrometer. One can speculate, that if the higher quality spectrometer would be used in LBO measurement, two peaks in the spectral profile would also be visible.

4.2.5 Section summary

To summarize the autocorrelation measurement, I measured pulse shaping in two borate crystals.

In LBO crystal, I observed very low conversion efficiency, with maximum being below 20 %, and slight pulse compression to around 1.2 ps, with simultaneous widening of the spectral profile and its shifting to a higher wavelength. The beam profile deteriorated from the back-conversion, but was more influenced by the change in input energy rather than predelay.

In BBO crystal, the observed efficiency was much higher, reaching 50 %, and **I achieved around 2.5-fold pulse compression down to 0.75 ps from the original 1.8 ps 1H pulse in the short $D4\sigma$ regime in BBO crystal with an efficiency of 15 %. The trends and values of predelay with the highest efficiency and lowest pulse duration coincide very well with the numerical simulations.** I also measured widening and shifting of the centre of the spectral profile, with two distinct peaks in the spectral profiles present.

However, the measured AC traces leading to the short pulses were always far from their assumed shape and the pulse durations are thus unreliable. Due to that, I decided to do a new measurement with a FROG apparatus.

4.3 New measurements with FROG

The FROG device I used was limited to measurements with repetition rates above 10 kHz. I tried to use it at the basic 1 kHz repetition rate of the laser, but the FROG trace was too noisy and the pulse retrieval was nor reliable, nor repeatable. That is why I have measured all the presented data at a repetition rate of 10 518 Hz. Otherwise, all the controlled and diagnosed driving laser parameters were the same as in the AC measurement.

I first measured the data at few predelays and input energies in LBO crystal. The measured conversion efficiency is shown in figure 4.9 and one can immediately see, that the efficiency is around two times higher than the one obtained from the AC measurement. The maximum efficiency of 32 %, and subsequently the onset of the back-conversion process, is at energy around 80 µJ, which also differs from the previous results shown in fig. 4.3a. Between

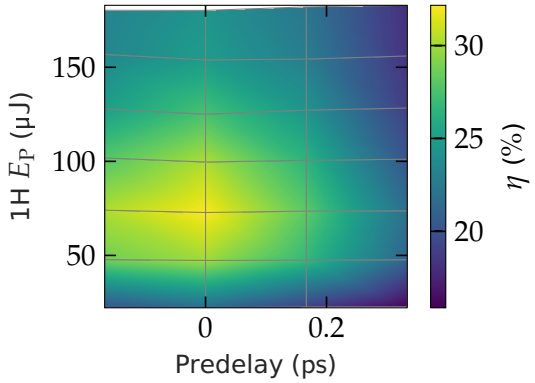

Figure 4.9: Energy conversion efficiency η in the LBO crystal in dependence on predelay and input energy E_P measured during the measurement with FROG.

the measurement, some kind of maintenance of the driving laser was conducted and I am not sure, what changed apart from the repetition rate.

In figure 4.10, results of pulse shape measurements are shown. First, FROG trace and pulse retrieval, together with the beam profile, at low input energy of 22.7 µJ is shown in fig. 4.10a. No back-conversion is expected at this low energy and the pulse temporal profile should be simple and short. The FROG measurement reveals this expectation to be true. The pulse temporal profile has a $\Delta t_P^{FWHM} = 1.1$ ps, so slightly shorter than the 1.2 ps value measured by autocorrelation. The beam looks good and smooth and the spectral profile agrees exceptionally well with the one measured by a spectrometer.

Next, I show two pulse profiles in the energy region, where back-conversion is expected to be prominent, around 125 µJ with zero predelay in fig. 4.10b and predelay of 0.33 ps in fig. 4.10c. Without predelay, the temporal profile is still simple. The back-conversion manifests itself by lowering the central peak, which is consequently not so sharp and the Δt_P^{FWHM} is increased to 1.6 ps. Now, if one introduces the predelay, widening of the spectral profile becomes apparent, and second peak appears at a longer wavelength. At first, the spectral broadening observed by the spectrometer was smaller than the one retrieved from the FROG trace, and the features were less visible. The temporal profile had $\Delta t_P^{FWHM} = 0.8$ ps, was sharper and 2.3 times shorter than the input 1H pulse (with energy conversion efficiency 24 %).

However, since the source trace is noisy and asymmetric, the retrieval algorithm did not converge every time to the same results. All of my tries at the retrieval ended with a two peak spectrum and I show in the fig. 4.10c also a second possible retrieval, where the retrieved spectrum is better matched to the one measured. From this retrieval, the pulse duration is not short any more, the Δt_P^{FWHM} is 1.8 ps and **the pulse shape is similar to the one calculated from**

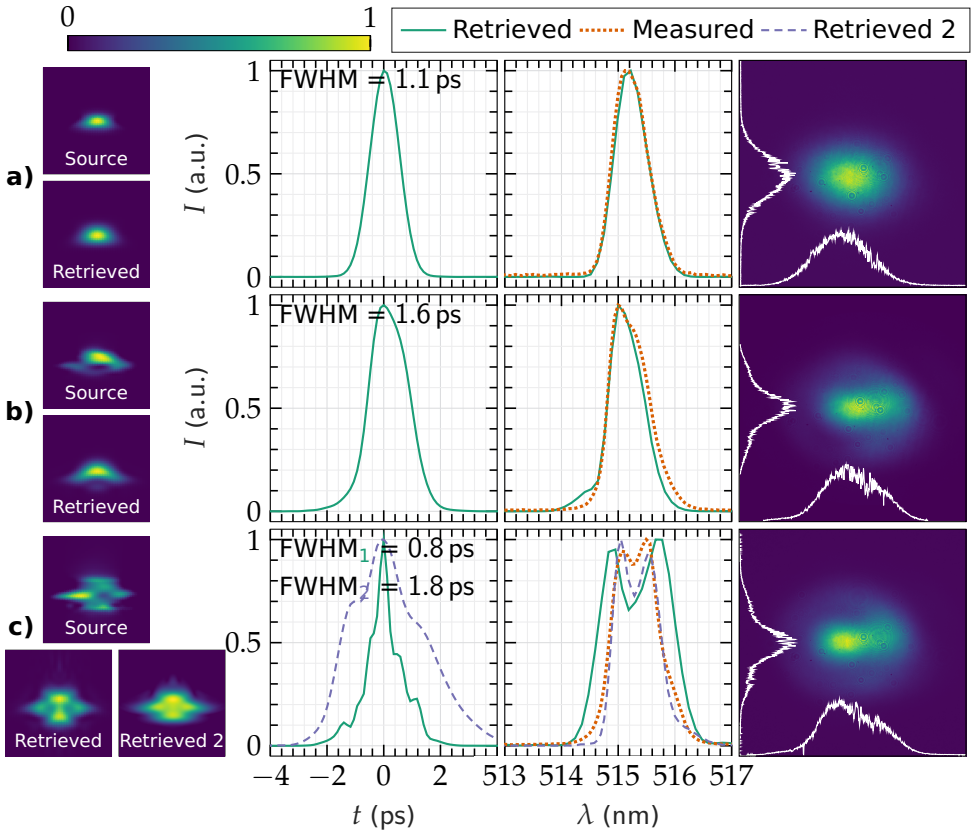

Figure 4.10: Selected pulse shapes measured with FROG. From left to right: Source and retrieved FROG trace (horizontal axis is pulse delay and vertical axis is optical frequency), the retrieved temporal pulse shape, retrieved and measured spectral profile and the beam profile with plotted area of $3.52 \times 3.52\,\mathrm{mm}^2$. The data are measured at energy 22.7 µJ and predelay 0.33 ps (a), 125.1 µJ and zero predelay (b) and 128.3 µJ and 0.33 ps predelay (c).

simulations and plotted in fig. 3.3a. By this I mean, that there is a wide pedestal and a smaller peak coming out of it. In the simulations in fig. 3.3a, I have shown a temporal pulse profile with a shorter peak, which was appearing as the predelay was increased, and I speculate, that it would also appear in the experiment, if I had measured the FROG traces with higher predelay.

One note about the beam profiles: Apart from being asymmetric, they agree well with the simulations in fig. 3.3bc – there is a central peak, which is narrower compared to the beam profile at low energy, and wider pedestal.

I made further measurements with the FROG in order to increase the measured predelay range and have more particular powers I measured at. I experienced more problems with the FROG (the traces were even more asymmetric

than is visible in fig. 4.10) and after the measurement and data analysis, which gave unexpected results, I enquired about the state of the driving laser and noticed, that there was a post-pulse 9 ns after the main pulse with energy at around one third that of the main pulse. This of course devalued the results and I have decided to abandon this pulse shaping method based on back-conversion in order to pursue the next option – pulse shaping with group velocity control.

This or similar previously unnoticed problem with the driving laser could also be the cause of the unusually small energy conversion efficiency observed in section 4.2.3 and figure 4.3.

4.4 Chapter summary

In this chapter, **I demonstrated shaping of the temporal pulse profile in LBO and BBO crystals with a simple setup consisting of a predelay stage.**

In the autocorrelation measurement with the BBO crystal, I achieved around 2.5-fold pulse compression down to 0.75 ps from the original 1.8 ps with an assumption of sech^2 pulse shape. The energy conversion efficiency was around 15 %. To compare it with previous numerical simulations, the measured pulse was by 0.3 ps longer than the simulated one, but so was the input pulse. The simulated conversion efficiency was 11 %. I also measured the broadening of the spectral profile and creation of two peaks in it, which was in agreement with simulations and previously reported experiments. The value of predelay with the shortest pulse was also in agreement with the simulations. Since the difference in the 2H pulse duration can be explained by the difference in the 1H pulse duration, it can be said, that **the experimental results follow the numerical simulations exceptionally well.**

The maximum conversion efficiency achieved in the type II phase matched LBO crystal was 32 % and 50 % in the BBO crystal, so significantly lower than in the type I phase matched crystals in chapter 2, where the maximum efficiency was around 80 %. It was also lower than the simulated efficiencies.

Next, I measured the pulse shape of the 2H pulse generated in the LBO crystal with FROG. The FROG retrieval algorithm did not always converge to the same solution. There is a possibility, that I measured more than twofold pulse compression down to 0.8 ps with a conversion efficiency of 24 %. Other possibility is, that **I obtained pulse temporal profile similar to the one, that was expected based on the numerical simulations,** with large pedestal and short peak on top of it. The latter version is more convincing and probable, because the retrieved spectrum in this case matches more closely with the one measured by a spectrometer.

More thorough FROG measurement and analysis was impossible due to some technical problems with the driving laser.

Strong beam deterioration accompanies the pulse shaping process, so the potential uses of this particular pulse compression shaping are limited. Using top-hat beam profile would result in an improvement of the pulse shaping process, as the rate of the back-conversion would be invariable across the beam. This would increase the possible application range as well as the accuracy of the characterization.

5 Pulse shaping through tilting of the pulse fronts

In this chapter, I describe the experimental setup and the results of the experiments with tilted pulse fronts, which aim to verify the numerical simulations from chapter 3 and which are currently being prepared for publication.

5.1 Experimental setup

The experimental setup, shown in figure 5.1, consists of three distinct parts: The predelay part, the part responsible for tilting of the pulse fronts, and diagnostics part. I now describe all of them in more detail.

5.1.1 Predelay generator

First thing in the experimental setup is a predelay generator, which is almost the same as the one in the section 4.1. There is one change, however. Since there is a need for the spatial walk-off pre-compensation, one of the retro-reflectors, in the figure 4.1 shown as two mirrors, is mounted on a linear stage perpendicular to the direction of the incoming and the outcoming beams. By slightly moving the linear stage, the position of the outcoming beam is shifted, but the direction does not change. This allows for simple pre-compensation of the spatial walk-off in the critical plane, which is perpendicular to the orientation of the grooves in the diffraction grating. The horizontal plane in the laboratory translates to the plane containing extraordinary polarization in the nonlinear crystal. This polarization is the faster one in the BBO crystal, so the horizontally polarized pulse has to be predelayed.

5.1.2 Tilting of the pulse fronts and SHG

Next, there is a diffraction grating, which causes the angular dispersion, or the pulse front tilt. As a remainder, one needs to tilt the pulse fronts by an angle of 23.5° with respect to the wavefronts inside the crystal. Outside of it, this angle is a little bit different for each polarization, particularly 34.6° for

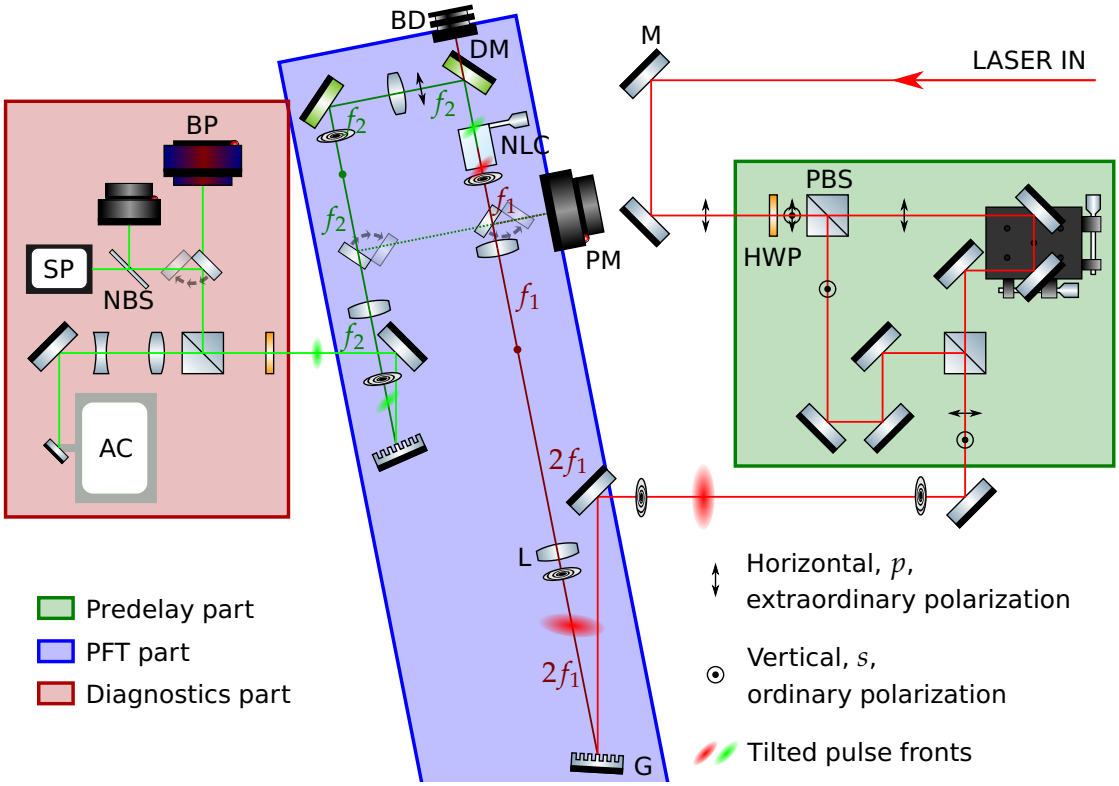

Figure 5.1: Experimental scheme used for pulse shaping experiments with tilted pulse fronts. Shown are also the polarization of the laser beam in different parts along the optical path and the tilted pulse fronts. Legend: M – mirror, HWP – half-wave plate, PBS – polarizing beam splitter, G – diffraction grating, L – lens, PM – power meter, NLC – nonlinear crystal, DM – dichroic mirror transmitting first harmonic and reflecting second harmonic, BD – beamdump, AC – autocorrelator, NBS – non polarizing beam splitter, SP – spectrometer and BP – beam profiler.

the ordinarily polarized pulse and 36.1° for the extraordinarily polarized pulse. For the *e*-polarized pulse generated at the second harmonic frequency, the PFT angle outside the crystal will be 35.4°. It is not practical to tilt each input pulse by its particular ideal value, so I tilt them both only approximately with the use of one diffraction grating.

Before picking the particular gratings, I will comment further on the angular dispersion. Following the analysis in [66], when the pulse is dispersed by a diffraction grating, it gets longer upon the propagation, and the tilt of the pulse front is reduced. The reason for that is following: since there is an angular dispersion, each spectral component is headed in a different direction. This causes decrease of the available spectral bandwidth at each particular point, resulting in pulse broadening. The beam also gets larger upon propagation,

which causes the reduction of the tilt. It is simple to calculate the tilt generated at the diffraction grating (equations (1.16), (1.18) and (1.19)), but not so simple to calculate the changes happening upon the propagation, which depend also on the spectral profile, beam size and other parameters. Furthermore, I would like to limit the pulse broadening.

This can be solved by imaging the diffraction grating into the nonlinear crystal [67]. It is not practical to use one lens as a 4f imaging system, as the beam size and tilt would be the same in the crystal as at the grating, but the divergence would be larger. This is unacceptable, since the angular acceptance of the relatively thick nonlinear crystal is much smaller than the potential divergence. Better is to use a Keplerian telescope focused to the infinity, with the grating at the object focal plane of the first lens and the crystal at the image plane of the second lens. This allows for the collimated beam to stay collimated, pulse broadening is avoided and the angular dispersion is magnified by the telescope magnification. The crystal has to be imaged onto the second diffraction grating with another telescope to compensate the angular dispersion.

Now, to continue with the design of the diffraction grating: Originally, I wanted to avoid magnification and I proposed to use two lenses with the same focal length. To avoid creating a spark in the focus, I used two lenses with $f = 125\,\mathrm{mm}$ to image the grating. I decided to use a diffraction grating from Thorlabs `GR25-0610` with 600 lines/mm and with a blaze angle of 17°27′ designed for a wavelength of 1 µm. The diffraction angle β_d and PFT α_0 for such grating at a wavelength of 1030 nm is plotted in fig. 5.2. The Littrow angle is 18° and $\alpha_0 = 33°$ at this angle. I used an incidence angle close to the Littrow one, nominally 12.5°, with $\alpha_0 = 34°$ and a diffraction angle of 23.7°. Thus, the angle between the incident and diffracted beam was 11.2°. For the second harmonics beam, I used grating from Thorlabs `GR25-1205` with 1200 lines/mm and identical angles.

Unfortunately, the first grating was damaged in the experiment, when higher energies were used. I was forced to use an incident beam of a double size, different grating `GR25-0310` and telescope, which again reduced the beam size two times, with the first lens having $f_1 = 250\,\mathrm{mm}$ and the second one $f_1/2 = 125\,\mathrm{mm}$. The grating had 300 lines/mm. I did not want to change the rest of the experimental setup due to the different angles, so I used such angles as to achieve the same angle between the incident and the diffracted beam. Thus, I used an incidence angle of 3.3°, resulting in $\alpha_0 = 32.6°$ and $\beta_d = 14.5°$. This is the closest I could get to the ideal PFT of 35° with this kind of grating and standard set of lenses, while staying close to the Littrow angle, which was necessary in order to maintain high efficiency of the diffraction grating.

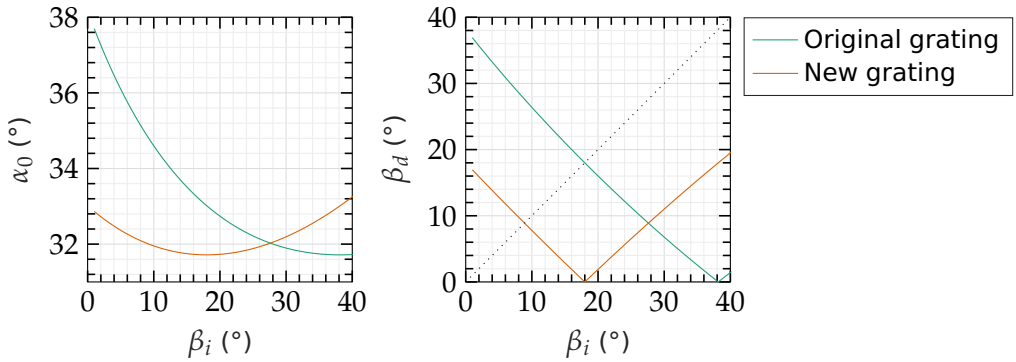

Figure 5.2: The dependence of pulse front tilt angle α_0 and a diffraction angle β_d on the incidence angle β_i of the original grating with 600 lines/mm at a wavelength of 1030 nm and 1200 lines/mm at a wavelength of 515 nm, and a new grating with 300 lines/mm at 1030 nm and with the angular dispersion already doubled by the imaging telescope, calculated using equations (1.16), (1.18) and (1.19) in an $m = -1$ diffraction order.

Having started on the topic of diffraction efficiency, it is expected to be close to 60 % for an average polarization. The efficiency is different for each polarization, so the ratio of the energy in the input pulses has to be measured after the diffraction grating, and set to 1 : 1. Because of the limited diffraction efficiency of the grating, the power of the first harmonic frequency is always measured after the diffraction grating and the power of the 2H beam is measured before the second diffraction grating.

Finally, 1H beam at the diffraction grating is imaged into a nonlinear optical crystal. I used two crystals for the experiment. Both were **BBO crystals with dual wavelength AR coating at both faces with aperture of $8 \times 8\,\mathrm{mm}^2$ from company Castech. One had a thickness of 6.12 mm and the second had a thickness of 8.45 mm**. Their cut angle was $\theta = 33.7°$ and $\varphi = 0°$, and were operated at a room temperature.

5.1.3 Diagnostics

For diagnostics, it was already mentioned, that the laser power was calibrated to a value just before the crystal in the case of the input power and after the second dichroic mirror for the output power. Other parameters that have to be measured are spectrum, beam profile and a pulse duration or pulse shape. It would be ideal to measure the pulse shape with a FROG, but our FROG measurement device needs repetition rate at least 10 kHz, and the driving laser cannot achieve sufficient energies with such repetition rate. Thus, I used just

an autocorrelator for the pulse duration measurement, with all its limitations. I resigned on measuring the M^2 parameter, as that would be too time consuming.

For the measurement of the 2H spectrum, I used Narran spectrometer BR8 with an integration sphere IS200 from Thorlabs. Before the integration sphere I put a blue coloured glass filter BGG21 to filter out the rests of the first harmonic frequency, and I measured the spectrum in the second diffraction order. For the power measurement, I used Ophir 50(150)A-BB-26 thermopile power meter for the calibration – measuring the 1H beam after the diffraction grating and the 2H beam before the second grating – and Ophir 3A thermopile power meter for the continuous 2H power monitoring. For the profile measurement I used camera from Cinogy, model CinCam CMOS 1.001 nano, with a RayCi Pro beam profiling software. The autocorrelation was measured with APE pulseCheck device. The beam was originally larger than was the size of the input aperture of the autocorrelator, so I added a telescope with lenses $f = 200\,\mathrm{mm}$ and $f = -50\,\mathrm{mm}$ to reduce the beam size four times.

5.2 Parameters of the driving laser

I used Perla B laser system at 1 kHz repetition rate regime. The maximum energy available at the time of the experiments was around 6 mJ. The FWHM pulse duration was 1.7 ps according to the Gaussian fit and 1.5 ps according to the slightly better sech^2 fit. The simulations were done expecting 1.7 ps long Gaussian pulse, which was Fourier transform limited. That is not the case of the Perla B laser, which was reportedly slightly chirped. The beam position stability was around 50 µm in the critical horizontal plane and the pointing stability was around 1 µrad. This value is good enough to not influence the efficiency of the SHG by even 1 %. The M^2 parameter was around 1.1 (measured before the setup), the beam was a simple astigmatic one. The power stability was around 0.3 % after the laser was properly warmed up and in use. The RMS energy stability was 0.6 %. The beam was slightly divergent and elliptic. The ellipticity was 0.89 with azimuth angle of 18°, the $D4\sigma$ width of the major axis was 5.02 mm and of the minor axis the width was 4.49 mm.

Based on the numerical simulations, I expect the pulse compression to occur at peak intensities between 15 and 20 $\mathrm{GW/cm^2}$. For the intensity calculation I use equation (1.12). With parameters as stated in the previous paragraph, I measured at energies of 2.35, 2.70, and 3.10 mJ, achieving peak intensities of 15.0, 17.2, and 19.8 $\mathrm{GW/cm^2}$, respectively, under assumption of circular beam profile with a diameter of 4.76 mm.

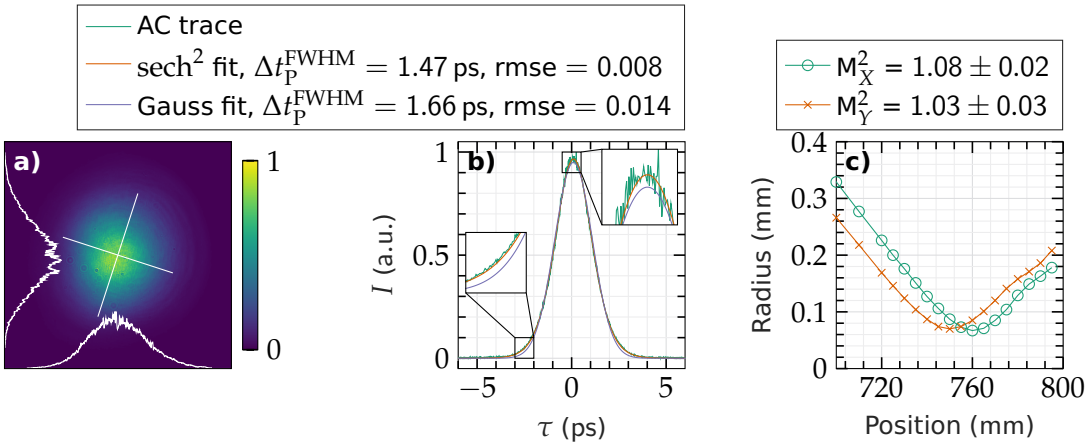

Figure 5.3: Selected characteristics of the driving laser: the beam profile (a) with its cross-sections, the autocorrelation trace (b) with fitted curves and two zoomed regions in the insets, and beam caustic measurement (c) with a lens with $f = 750$ mm.

5.3 Measurement protocol

After the characterization of the driving laser, I set the first half-wave plate in such a way, as to ensure that after the diffraction grating the power in both polarizations was the same. Afterward, I needed to find the proper orientation of the crystal and the zero predelay. Fortunately, both of these could be combined into single measurement.

Normally, there are two orientations of the crystal allowed. When the critical plane is in the horizontal direction, one can rotate the crystal left and right to find the phase-matching direction, and it does not matter, whether e.g. one increases the n of the e-polarized beam by rotating to the right or decreases it. But in the case of tilted pulse fronts, this orientation is crucial. One can remember figure 3.4, where one can see, that with a PFT angle of $\alpha = 23.5°$ there is large GV difference, but the n_g^{SH} lies just in the middle of n_g^{1He} and n_g^{1Ho}. On the other hand, when $\alpha = -23.5°$, there is almost no difference between the group velocities of the input pulses, and the SH pulse is significantly slower.

Just from a simple analysis I can show, which orientation is the right one, and find the zero predelay at the same time. If the angle is $\alpha = 23.5°$, then I can change the predelay by some amount and the conversion efficiency should not change significantly. There will be a range of predelays, where the input pulses will meet inside the crystal, and regardless, whether they meet exactly in the middle of the crystal, or earlier, or later, the second harmonic pulse will be generated for approximately the same time and in the same way. If $\alpha = -23.5°$, then the situation is different: If the pulses are separated at the input face of the

crystal by even a little, they will not have the time to approach each other and generate the second harmonic frequency efficiently. But if they arrive together, they should cause more efficient conversion than in the case of a positive angle α, as they will generate the SH beam for the whole crystal length.

Thus, the proper way to find the crystal orientation is by choosing one orientation, changing predelay in some range with high efficiency and measuring the SH power curve. Next, the crystal has to be rotated by 180° along the axis coincident with the beam propagation direction, and the same curve has to be measured again. One curve should contain sharp peak and then decrease quicker (for the negative α), whereas the other should have wider plateau, with maximum efficiency lower and decrease more slowly, as one goes further from the plateau (for the positive α).

To further confirm, one can asses the mutual positions of the efficiency maxima. The *e*-polarized beam is the one, which is being predelayed, and the faster one at the same time. With negative PFT angle, the maximum will be around 0 ps predelay, but with the positive PFT angle, the faster polarization should be delayed in respect to the slower one, so the maximum of the efficiency should be at larger predelay (before the calibration between ps and mm, this means larger distance, so higher number). From the numerical simulations in figure 3.5, one would expect the distance between the maxima to be approximately 0.4 ps.

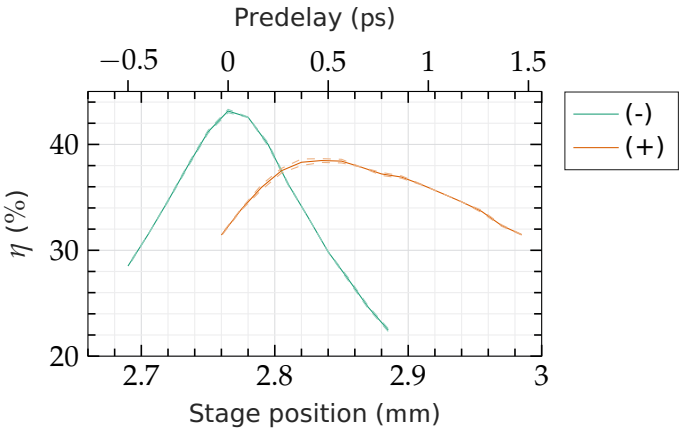

Figure 5.4: The energy conversion efficiency η curves across a varying predelay of the faster pulse, measured with two orientations of the nonlinear crystal. The orientation with positive PFT angle is labelled (+) and the one with negative PFT is labeled (-). Calibration between the position of the translation stage and predelay in units of ps is shown with the top axis. These data were measured with the shorter, 6 mm thick crystal, 1H power around 0.61 W and orientation for maximum efficiency at stage position of 2.8 mm.

Finally, I did such measurement and the results can be seen in figure 5.4. Since both of the assumptions are confirmed at the same time, and even the predelay distance between the conversion efficiency maxima was measured to be around 0.4 ps, there is no doubt about the correct crystal orientation as well as the zero predelay. I measured both of the crystals and zero predelay was always at the same linear stage position, while the length of the plateau for the correct orientation prolonged for the thicker crystal. For the record, all of the predelays in the further text refer to the position of the translation stage as follows: 0 ps predelay is at a position of 2.765 mm and change of predelay by 0.1 ps is equal to a change of stage position by 15 µm (the beam travels the distance two times).

Next, there was an issue of aligning the crystal for proper phase matching. I always aligned the crystal at relatively low input power (around 0.3 W), where the back-conversion is not yet prominent, and I looked for the maximum power. It was important to do it at low power, because once one is in the back-conversion regime, there are two conversion efficiency maxima at slight phase-mismatch on either side. This is illustrated by numerical simulations in figure 5.5, and can be attributed to the periodic exchange of the energy between the pulses. At the particular length, if one gets unlucky, one can end up in a trough, but at slight phase-mismatch, the period is smaller and one can end up in a crest of the energy exchange function, increasing the observed efficiency.

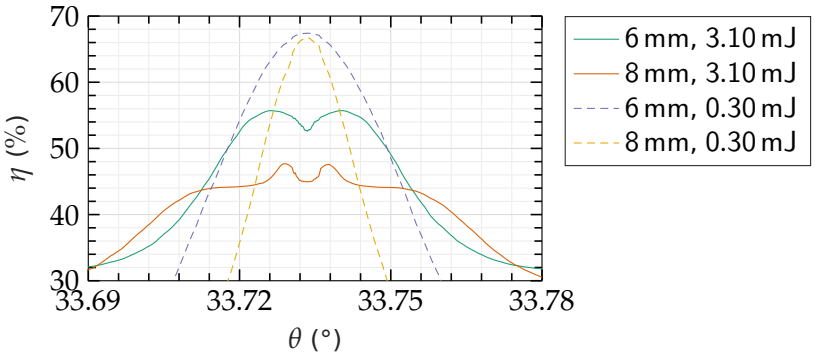

Figure 5.5: The variation of the conversion efficiency η of the 2H beam with the phase-matching angle θ, simulated with zero predelay and without PFT for two crystals and input energies.

To set up the walk-off pre-compensation, I observed the 2H beam profile at low power with zero predelay, and I set the mutual input beam distance in such

way, that the energy fluence profile of the 2H beam is the most symmetric one. I assessed this only visually.*

Last step in the measurement preparation was setting up and the calibration of the diagnostics. I subtracted background of the spectrometer and of the beam profiler at all exposure times. I also calibrated the monitoring power meter to the value of the calibration power meter. The beam was aligned into the autocorrelator to find the highest maximum of the autocorrelation trace at low power (around 0.3 W in the nonlinear crystal) and zero predelay, where the beam profile was circular, smooth and symmetric. The averaging was set to low (over two measurements) and the resolution to medium (1000 points per the whole delay range).

The measurement itself constituted from 40 steps at each energy for each crystal, each step was measured at different predelay from 3.5 ps to -0.4 ps with following procedure:

1. Set AC attenuator to zero (so all of the power goes to the rest of the diagnostic) and send all the power to power meter and spectrometer by flipping up the mirror.
2. Change the predelay to the correct value and wait few seconds for everything to settle down.
3. Measure the power for 20 s and measure the spectrum in the meantime.
4. After this is finished, flip the mirror down and measure the beam profile (for 5 s with 10 Hz repetition rate of the image data acquisition, and exposure time varying between 7 to 100 ms depending on the current power and number of the absorptive filters before the beam profiler).
5. Set AC attenuator in such way, that the AC trace is nicely visible but the detector is not overexposed. Wait for the stabilization of the trace and save three traces at 50 ps delay range.
6. Set the delay range to 15 ps, wait for the stabilization and measure another three traces.

5.4 Data processing

The data processing procedure follows the text in section 1.5.

There is a slight variation in the power processing procedure, since the small monitoring power meter I used took few seconds to stabilize at the correct

*In retrospect, this seems as a bad way to do it. More correct would be looking for the broadest spectrum or the shortest pulse at the working input intensity, then changing the walk-off pre-compensation to achieve most symmetric beam, and then look for the broadest spectrum again, and so on, iteratively. Alas, I did not have enough time to do this.

power. Due to that, I always measured across 20 s and then disregarded the first five seconds of the measurement. I also had a power calibration constant for the monitoring power meter, with its own error value, so the error of the measurement was already corrected for this calibration error.

The pulse autocorrelation was also processed differently and the need for that is evident from the pulse shape simulated in figure 3.5c and repeated in fig. 5.6, together with its calculated autocorrelation. One can see, that there is a wide pedestal and then a sharp peak in the autocorrelation. So to somehow asses the measured pulse, I tried not only standard fitting with the assumption of either Gaussian or sech^2 pulse, but also fitting with a sum of two functions corresponding to the AC of sech^2 together. These fits are also visible in the figure. 5.6.

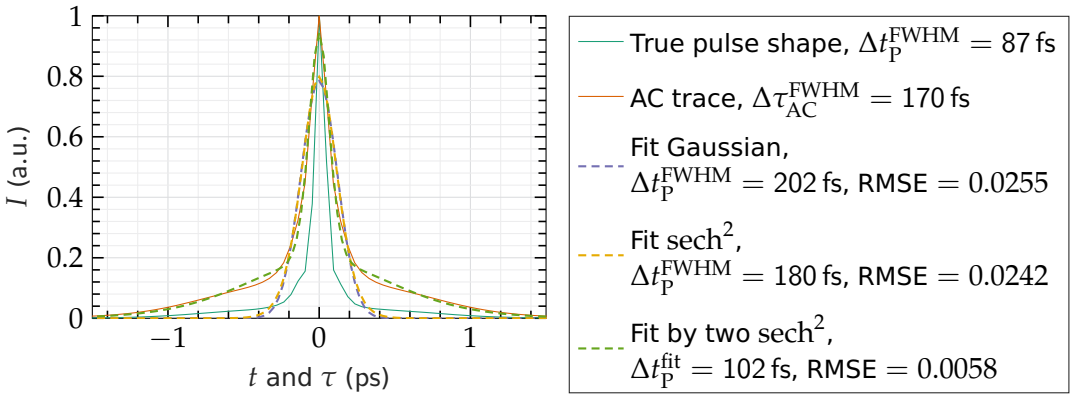

Figure 5.6: Temporal profile of the calculated pulse with the highest output power, together with its autocorrelation trace and fitting by various function. In the legend, basic parameters of the curves and fits are presented. t refers to time and Δt_P to a time duration, whereas τ refers to the autocorrelation delay and $\Delta \tau_{AC}^{FWHM}$ to a duration of AC.

It can be clearly seen, that the standard fitting functions are unusable. On the other hand, the fitting by sum of two functions (1.47) results in a good cover of the AC trace, the root mean squared error is low and the calculated Δt_P^{fit} is closest to the Δt_P^{FWHM} of the original pulse. I should add, that the Δt_P^{fit} for this particular function is calculated from the lower $\Delta \tau_{AC,s}^{FWHM}$ parameter by dividing it with 1.54.

I also measured three traces of the autocorrelation for each delay range, and I did the fitting procedure for the average of the traces.

5.5 Discussion of full results and overall trends

I have plotted four datasets of the results into the figure 5.7. I have chosen this way, because even though the individual graphs have to be small (and the particular values are therefore difficult to read), one can see the trends and compare the data more globally. One can also see better, what is the influence of changing the energy, predelay or the crystal thickness. Now, I will describe the data and the overall trends I can observe, and then I will present full data for some particular results.

5.5.1 Conversion efficiency

Let me start with the efficiencies in fig. 5.7a. For the 6 mm thick crystal, the shape of the efficiency curve matches nicely the simulated one in fig. 5.7b. There is a plateau between 0.3 ps and 1.2 ps. On the negative predelay side, the efficiency decreases more sharply than on the positive predelay part, which is exactly what one would expect. The absolute magnitude of the efficiency is around half of that of the simulated one.

For the thicker crystal, the measured plateau is about three times longer than the simulated one, and the efficiency is still lower. One can, however, observe, that at the right side of the graph, the efficiency is higher in the longer crystal, and it is the other way around on the left side of the graph. This corresponds with the simulations. One can notice one more thing – the efficiency is higher at lower energies.

I presume, that there is a phase-mismatch caused by beam aberrations (more specifically, by the stripes discussed later in section 5.6.3), which was unaccounted for in the simulations. This increased phase-mismatch results in much higher rate of the back-conversion (with bigger energy and thicker crystal even more pronounced), which does not allow for the resulting 2H power be so high. Due to this fact, one cannot see the high peak in the 8 mm crystal and instead, there is only the wide plateau. Outside of this region, the efficiency behaves according to the expectations, but is approximately two times smaller, which can be again caused by the beam aberrations. These could be caused by the diffraction grating, which introduced intensity modulations into the beam profile. The exact nature of the aberrations is discussed in section 5.6.3 and visible in figure 5.8c-f.

5.5.2 Spectrum

Next, there is a $D4\sigma_\lambda$ width of the spectral profiles in fig. 5.7c and the duration of the FT limited (FTL) pulse in fig. 5.7d. Around zero predelay, the spectrum

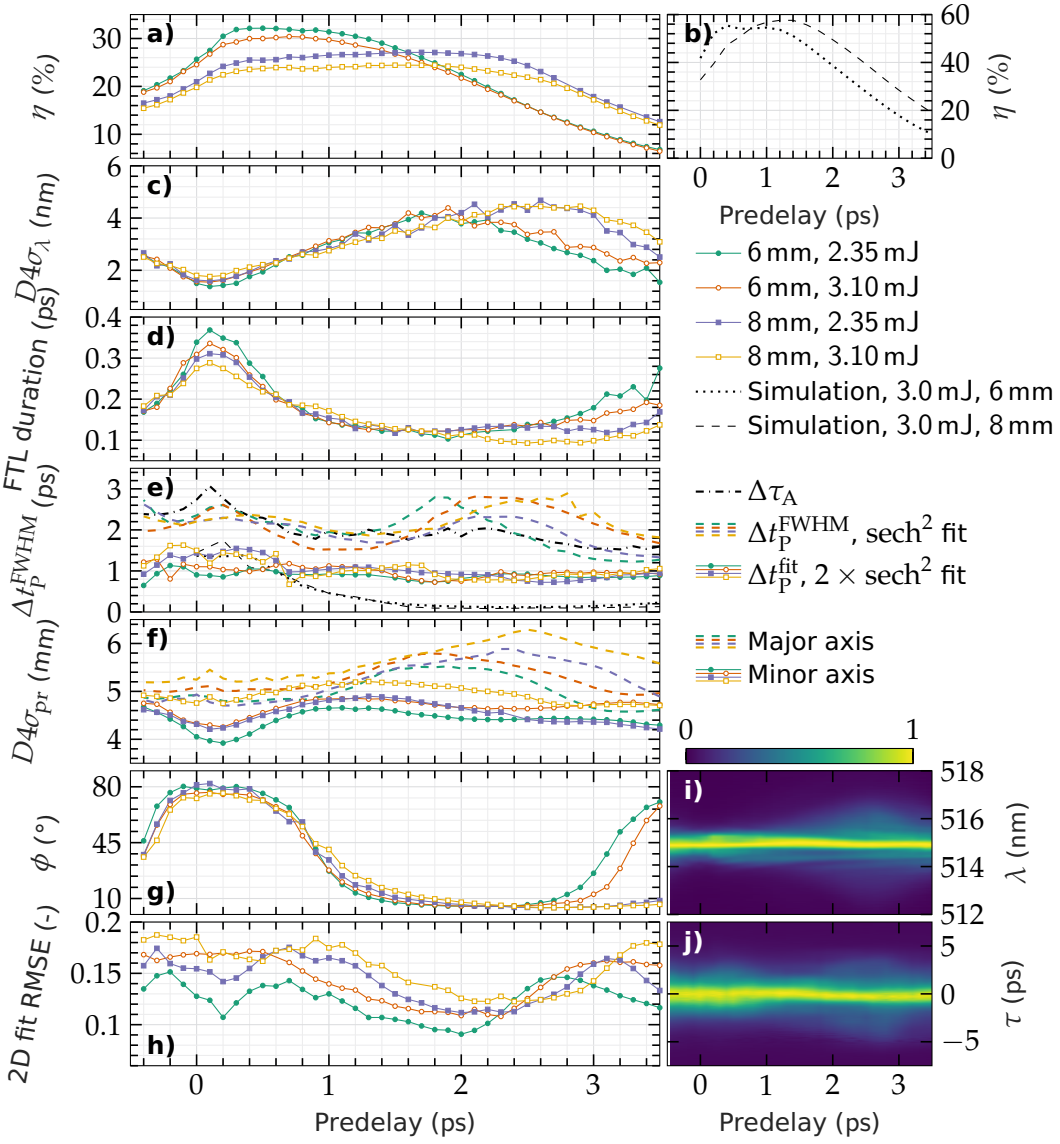

Figure 5.7: The collection of experimental results measured in two crystals at two energies. Shown are measured (a) and simulated (b) energy conversion efficiency η, spectral width $D4\sigma_\lambda$ (c) and the the duration of FT limited pulses (d). Next, there is a pulse duration $\Delta t_\mathrm{P}^\mathrm{FWHM}$ (e) measured by autocorrelation and fitted by two different ways. Furthermore, there are parameters of the beam profiles: width along major and minor axis (f), azimuth ϕ (g) and error of fit to a 2D Gaussian function (h). Finally, the spectral profiles measured in 8 mm long crystal at energy of 3.10 mJ are shown in (i) and autocorrelation traces measured at the same conditions are shown in (j).

is the narrowest and the FTL duration is the highest. For the 6 mm crystal, the maximum of the spectral width is around 1.9 ps predelay and then it decreases. For the 8 mm crystal, the maximum is around 2.5 ps. The minima of the FTL duration correspond to the respective maxima of the spectral width. **At higher energy, the spectrum is consistently wider and FTL duration shorter, with the absolute minimum being below 100 fs, the value I am aiming for.**

From the spectra one can also tell, that the back-conversion is not the main culprit behind spectral broadening, because the maximal back-conversion is at smaller predelays, where the pulses have enough time to interact. On the other hand, the maxima of the spectral width are at larger predelays, where the pulses meet just at the end of the crystal and do not have so much time to interact between each other. So the spectral broadening truly occurs due to the meeting of the pulses and generation of the short 2H pulse, as was intended and expected, based on illustration 1.3.

How do the spectral profiles look like is visible in fig. 5.7i. The image was measured with the 8 mm thick crystal at the 3.10 mJ 1H pulse energy. The originally more or less Gaussian spectral profile gets narrower peak and wide low intensity wings with increasing predelay, with the widest wings around predelay of 2.5 ps. Notice, that there are also small side peaks visible at the lower wavelength side of the spectrum, which was also simulated in figure 3.6e. I show some particular spectral profiles and compare them with the simulations later in section 5.6.1.

5.5.3 Autocorrelation

In fig. 5.7e are the temporal pulse widths as measured and calculated from the autocorrelation traces. Using normal fit corresponding to the sech^2 pulse shape does not make much sense, I added them for illustrative purposes. The widths from these fits are largest at the predelays, where the spectral width is the highest, and it should be the other way around. In fig. 5.7j one can see the autocorrelation traces measured with the 8 mm thick crystal at the 3.10 mJ energy. Where the spectrum is broadest, the autocorrelation trace is also broad, with large pedestal and narrower peak. This looks kind of similar to the expected autocorrelation trace visible in fig. 5.6. The sech^2 fit is unsuitable, since the measured pedestal is higher than the calculated one, the fitting approximates the pedestal more than the central peak, and the fitted pulse duration gets longer.

The narrower part of the measured AC trace is still much wider than it should be. This is also confirmed by the fitting with two (1.47) functions summed

together. According to these fits, the pulse duration gets shorter at about 0.7 ps predelay for all crystals and energies. Then there is a second decrease around 1.5 ps, but then the pulse duration stays more or less the same across the rest of the predelay range. The minimal pulse duration stays around 0.7 ps, which would hint at only a moderate pulse compression similar to the one achieved without PFT in chapter 4. To be sure, the minimum for the 6 mm and 8 mm crystal is around 1.8 ps and 2.4 ps or 2.6 ps, respectively. These values agree well with the predelays, where the spectrum is the broadest, but the pulse width minima are only slightly shorter than the surrounding points. One can notice, however, that the curves of simulated pulse durations are very similar to the FTL duration curves: there is a peak at around 0.1 ps, then the duration decreases with similar slope and from around 1.6 ps it stays low.

5.5.4 Beam profiles

The last three graphs, 5.7fgh, describe the measured beam profiles. They cannot really describe, how far from Gaussian the measured profiles are, as the RMSE of the 2D Gaussian fit is not a number, which can be easily interpreted without some known reference. However, I will first describe these general characteristics – beam widths, ellipticity[†], rotation of the principal axes – before showing some particular beam profiles.

For all the crystals and energies, the ellipticity is low at -0.4 ps predelay, but it rises sharply and is quite high at zero predelay. The next highest ellipticity is in the predelay region, where the spectrum is the broadest. This is actually global maximum, and is caused by the largest $D4\sigma_{\mathrm{major}}$, contrary to the first local maximum caused by the lowest $D4\sigma_{\mathrm{minor}}$. From the azimuth angle, one can see that these two local maxima of ellipticity are rotated by around 90°. Around zero predelay, the minor axis is close to the horizontal axis, and major axis is close to the vertical axis. As one increases the predelay, the width in the X axis increases and in the Y axis decreases up to the point of the broadest spectrum, and as the predelay is increased further, the trend gets reversed. I believe, that this width increase in the horizontal plane is caused by non-ideal compensation of the angular dispersion. At the predelay, where the spectrum is the broadest, it spreads in the horizontal direction due to the angular dispersion the most, and this changes the apparent rotation of the beam ellipsoid from the initial state with the beam in the vertical axis larger (see 1H beam profile in fig. 5.3a).

[†]Ellipticity is not shown in the figure 5.7 explicitly, but can be assessed from the difference between beam widths in minor and major axis.

The last graph in the figure 5.7 shows the fitting error of a 2D Gaussian function fitted to the beam profile, and it hints at the region with the beam most similar to the Gaussian beam being again in the region with the broadest spectrum. Without commenting on this observation further, I will advance to show some particular results at chosen predelay values, to be able to directly compare the spectral profiles, the autocorrelation traces and see the beam profiles.

5.6 Examples of individual results

Some chosen results measured in the 8 mm crystal with the highest energy are shown in figure 5.8 and some of their parameters are written in table 5.1.

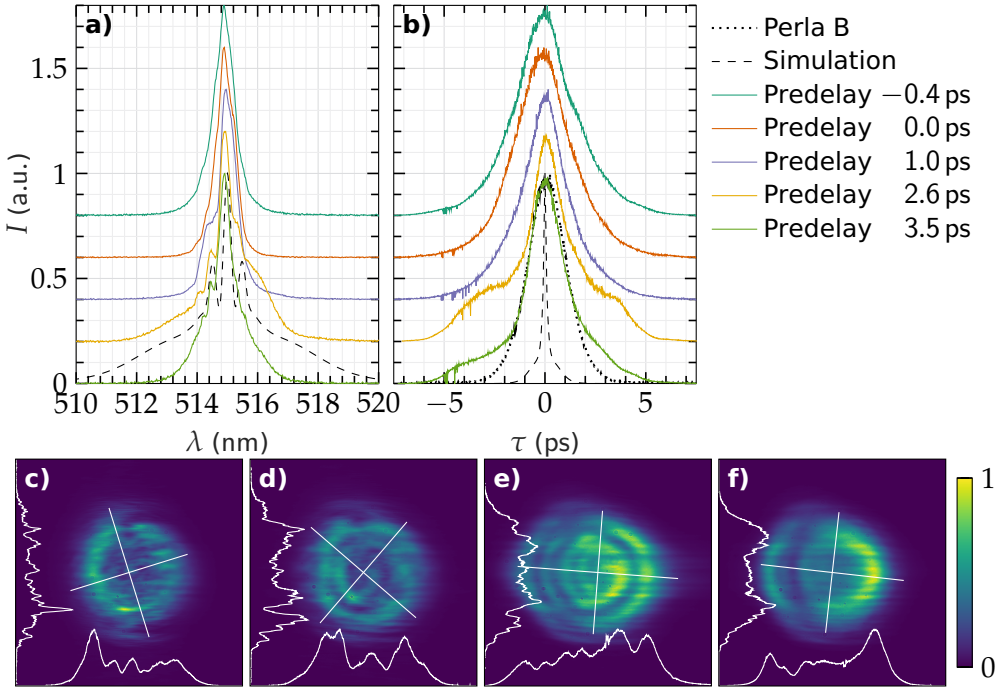

Figure 5.8: Spectral profiles (a) and autocorrelation traces (b) measured at different predelays in the 8 mm thick crystal with an energy of 3.10 mJ. Also shown are beam profiles at predelay of 0.0 ps (c), 1.0 ps (d), 2.6 ps (e) and 3.5 ps (f). Total area shown in the beam profiles is 7.04 mm × 7.04 mm.

5.6.1 Spectrum

Firstly, spectrum is shown in figure 5.8a. The width of the spectral profile is the lowest at zero predelay and as the predelay increases, new side peak starts to

Table 5.1: Chosen parameters for data points shown in fig. 5.8. η is energy conversion efficiency, $D4\sigma_{\mathrm{sp}}$ is a spectral width based on second moments, $\Delta t_{\mathrm{P}}^{\mathrm{fit}}$ is a pulse duration calculated from fit based on two sech^2 functions, $D4\sigma_{\mathrm{pr}}$ is a beam profile width in the major and minor axis, ϕ is the azimuth angle between the major axis and the X axis and fit RMSE is a fitting error of a 2D Gaussian function to the beam profile.

predelay (ps)	η (%)	$D4\sigma_{\mathrm{sp}}$ (nm)	$\Delta t_{\mathrm{P}}^{\mathrm{fit}}$ (ps)	$D4\sigma_{\mathrm{pr}}$ (mm)	ϕ (°)	fit RMSE
−0.4	15.4	2.51	1.13	5.19 and 4.92	36	0.182 59
0.0	19.8	1.80	1.50	5.24 and 4.76	72	0.185 37
1.0	24.0	2.75	0.92	5.38 and 5.17	41	0.174 84
2.6	21.4	4.45	0.85	6.24 and 4.80	4	0.124 18
3.5	11.9	3.09	1.06	5.58 and 4.71	6	0.178 36

appear at the lower wavelength part of the spectrum. At the optimal predelay of 2.6 ps the spectrum is the widest, with the pedestal ranging from below 512 nm to more than 518 nm. In the redder part of the spectrum, the side peaks are less pronounced. **The positions of the side peaks coincide well with the side peaks in the simulated spectrum,** but are less intense in respect to the central peak. The spectrum is asymmetric, but this stems from the asymmetry of the spectrum of the driving laser beam. The pedestal is wide, but still much narrower than would be expected from the simulations. As a reminder, the calculated 2nd moment spectral width was 8.1 nm, so almost double than the 4.45 mm measured here.

This spectral narrowing is partly caused by imperfect compensation of the angular dispersion by the second grating, which is also visible in the beam profile shown in figure 5.8e. The spectrum there is the broadest, and the width of the beam profile in the X axis is the largest. The farthest parts of the spectrum can be clipped by the small aperture of the used optics, so one cannot measure them. At the same time, both the polarizer and the mirrors between the nonlinear crystal and the spectrometer are designed for the central wavelength of 515 nm, and part of the spectrum farthest from this central value can be suppressed by the coatings. Of course, stronger effects are non-ideal PFT angle, causing non-ideal group velocities inside the crystal, slightly divergent beam at the crystal input face, and probably also temporal chirp in the 1H laser pulse. All of these effects result in the discrepancy between the measured spectral width and the simulated one. I would also like to remind the reader a spectral width measured in a standard second harmonic generation with the phase matching of the first type, presented in figure 2.8, where the 2nd moment spectral width was 1.04 nm. **Thus, the measured spectral width is two times lower than the calculated one, but still more than four times larger than the one ob-**

tained without implementing any pulse shaping technique. Accordingly, it supports much shorter pulse.

5.6.2 Autocorrelation

The autocorrelation traces are displayed in figure 5.8b. At negative or zero predelays, the traces look like regular ones and only slightly broader than the AC trace of the driving laser pulse. At 1 ps predelay, the trace gets narrower and the peak sharper. At even larger predelays, there is the distinct and expected pedestal, and from it, another, sharper peak rises. This is best visible with the 2.6 ps predelay, as for even larger predelays, the pedestal gets again lower and slowly diminishes.

Two things can be seen at a first glance: the traces are much longer than the simulated ones, and they are asymmetric. The much longer duration shows, that the pulse compression is sensitive about things not included in the numerical simulations. I will list them here again:

- non-Gaussian 1H pulse shape and beam profile;
- the 1H pulse had correct duration, but was not transform limited;
- divergent beam (since it was astigmatic, slight divergence was the best choice);
- the pulse energy and pointing stability was good, but not perfect;
- I did not manage to set up the correct PFT and then compensate the angular dispersion exactly;
- the spatial walk-off pre-compensation was probably set to non-ideal value.

Of course, there are other things and the most prominent one stems from the shape of the beam profiles and the method of the pulse duration measurement.

When the laser beam is directed into the autocorrelator, it gets splitted into two parts. One of the parts continues to a fixed retro-reflector and the other one continues to a retro-reflector mounted on a linear translation stage – this arm is a delay line. Afterwards, the beams are combined and they travel in the same direction. However, they are not coincident, because otherwise they would interfere with one another. They arrive onto a curved mirror and are directed and focused into a very thin nonlinear crystal, and a fourth harmonic pulse dependent on the position of the delay line creates a signal going into the detector. The measured beam has to be smaller than the input aperture of the autocorrelator, and both beams with a distance between them have to fit

onto the curved mirror and not get cut off at any other part of the device. That is why I added a telescope before the autocorrelator to decrease the beam size four times. Unfortunately, this worsened the already bad angular dispersion. Thus, the beam expanded inside the autocorrelator and the parts of the beam with wide spectrum were lost, as they did not fit onto the individual optical elements. This is how some of the pulse lengthening might have happened.

The asymmetry comes from the fact, that in order for the beam to get to the detector, it cannot travel in exactly the same direction as is the direction of the propagation of the linear stage in the delay line. This can be a construction problem of the particular autocorrelator, but I have found this to be true in three distinct devices of the same type. Due to this fact, the position of one of the beams changes with a change of delay. This means, that for every delay, different parts of the beam interact with each other inside the nonlinear crystal, and since the beam profile is highly non-homogenous and the different interacting parts thus have different intensity, the fourth harmonic signal (the autocorrelation signal) they generate has also different intensity. This leads to the asymmetric autocorrelation traces one can observe in the figure 5.8b, and it also hints at some deeper problem: It is unclear what is actually measured. Which features of the AC trace are dictated by the temporal profile of the pulse (which is actually different in every part of the beam, as was shown in figure 3.6) and which features are highly influenced by the variable beam profile? I do not have answer to this question. This same problem with autocorrelation, as well as FROG, was also observed in experiments of pulse shaping through back-conversion.

Introducing a pinhole before the autocorrelator and measuring only the centre of the beam will not solve the problem, because one can remember from simulated figure 3.6, that the pulse temporal profile is different in the centre of the beam and it has two distinct peaks. Only the temporal profile integrated over the whole beam area is the short pulse I am trying to measure.

5.6.3 Beam profiles

Finally, I will shortly comment on the beam profiles in figure 5.8d-f. The rotation of the axes is visibly caused by the uncompensated angular dispersion, which creates a wings, most notable in the beam profile belonging to the pulse with the broadest spectrum.

At low predelay, the beam profile is flattish, resembling a ring or a spiral. Since there is no central peak, the Gaussian fit is bad and the fitting error high. At higher predelay, there is at least some kind of peak visible, even though it's not central, symmetric or smooth. Still, the fitting error is lower, but the beam

shape is still very far from Gaussian. The concentric rings develop through the back-conversion – the rate of the energy exchange differs radially. The development of these rings was hinted by numerical simulations in figure 3.6d, where the radial steps are nicely visible in the cross-section. However, they were much less pronounced. The difference is again probably caused by the non-ideal input laser beam. Similarly to the simulated beam profiles shown in figure 3.5c, when predelay increases even further, the beam profile gets a little smoother and the concentric rings start to disappear.

The last problem with the beam profiles are the horizontal stripes. These are found in all the beam profiles, and are not caused by a diffraction from the crystal sides.[‡] When I removed the crystal and its holder and measured the collimation of the 1H beam, I also observed the stripes, only much more weakly. When I was again measuring the 2H beam profile along its propagation, the stripes were more pronounced than in the 1H beam and became much more noticeable after the second diffraction grating. For these reasons I presume, that the stripes are caused by the diffraction gratings, and they can negatively influence the whole pulse compression process.

5.7 Chapter summary

In this chapter I described the experiments I conducted at HiLASE centre and with which I aimed to find out, whether the numerical simulations from chapter 3 are realistic and one can achieve significant pulse compression, and possibly even peak power increase, by nonlinear second harmonic generation with tilted pulse fronts.

I observed conversion efficiency curves very similar to the simulated ones. The overall efficiency was measured to be approximately two times lower than the simulated one, but the observed trends matched the simulations closely. Where the spectrum was the broadest and pulse the shortest for each crystal and input energy, the conversion efficiency was consistently around 20 %.

I measured a significant spectral broadening. The spectral profile contained features expected from the simulations, at correct wavelengths and at correct predelays. The measured spectrum was very wide, the width was 4.5 nm and it supported pulse as short as 95 fs. However, the simulated spectrum was still almost two times broader with a width of 8.1 nm.

The measured beam profiles show a concentric ring-like structure, as was expected from the simulations.

[‡]I was originally worried about this, since the $D4\sigma$ of the 1H beam in the Y axis was around 5 mm and the clear aperture of the crystals was less than 8 mm. I aligned the beam to the centre of the crystal very carefully, and there was no change in the stripes.

However, there were problems accompanying the measurement. Due to the chosen diffraction gratings and their limited damage threshold, the pulse fronts were not tilted to the ideal value. Furthermore, the gratings introduced periodic intensity modulation into the beam profile, which increased the phase-mismatch, reducing the conversion efficiency and possibly also the magnitude of the pulse compression.

Last but not least, one cannot be sure in the autocorrelation measurement of the pulse width. Although the traces show a similarity to the ones I expected in having a pedestal and a sharper narrower peak, they are asymmetric and probably influenced by the non-homogenous beam profile. Most fo the features in the AC traces can originate from the temporal profile of the pulse, but some may be caused by the varying spatial beam profile.

It would be possible to repeat the experiments again with specially designed gratings to achieve the proper PFT angle. The complex pulse shapes should be properly characterized. For measurement with our FROG device, there is currently no suitable driving laser available, because it should work at a repetition rate of at least 10 kHz with an energy in pulse at least 4 mJ to allow for some energy losses in the diffraction gratings. Furthermore, there should ideally be no temporal chirp and astigmatism present in the laser. To tackle the problem of asymmetric autocorrelation (and possibly FROG) traces, top-hat beam profile could be used, with the peak intensity adjusted accordingly.

Instead of increasing the repetition rate of the driving laser, single-shot pulse temporal characterization could be employed. Even better option would be to use technique like Spatially and Temporally Resolved Intensity and Phase Evaluation Device: Full Information from a Single Hologram (STRIPED FISH) [68, 69], with which one can obtain full temporal characteristics of the laser pulse with a very good spatial resolution of few tens of μm in a single-shot measurement. The need for the top-hat beam profile would then be passé and the repetition rate of 1 kHz would be sufficient.

To conclude, based on the spectral measurements and the general observed trends in accordance with the simulations, I think **there is a real possibility of pulse shortening through the nonlinear frequency up-conversion with a predelay and tilting of the pulse fronts**. Currently, the main drawback is that the resulting beam profiles are far from Gaussian and limit the possible uses significantly. Furthermore, since two diffraction gratings and imaging optics are needed, this pulse compression scheme ceases to be compact and easy to align.

6 Conclusion

This thesis is devoted to the nonlinear second harmonic frequency generation process, from the point of view of high-repetition-rate, high-average-power Yb:YAG thin-disk lasers with pulses ps long in duration.

The first goal of the thesis was to **build a universal stage for an efficient generation of the second harmonic frequency**, which could be used with various high average power picosecond laser systems being operated at HiLASE centre and outside of it.

The development of such SHG stage, using LBO as the nonlinear crystal, was successfully carried out. The stage and its optimization is described in chapter 2 and also published in a paper [30]. The achieved **conversion efficiency is regularly in excess of 75 %, which is on par with the best results in the literature.** The second harmonic beam has very good beam quality, in the region of the best efficiency the M^2 parameter is around 1.5. More stages are currently regularly used with various laser systems, usually in a regime of lower conversion efficiency around 50 %, but **excellent beam quality factor around 1.2**.

The generated 2H beam has many uses, for example multi-beam drilling published in a paper [14], of which I am a co-author. I also observed simple pulse shaping of the 2H pulse – creation of top-hat-like pulse or a double-peaked pulse, when the SHG stage is operated beyond the best efficiency region, in the so called back-conversion regime. These pulse shapes can also find their uses for example in the pumping of the optical parametric chirped pulse amplification systems [31] to enhance the total OPA conversion efficiency.

This observed pulse shaping led me to the second goal of my thesis. The rest of this work is devoted to the **original numerical and experimental research of nonlinear pulse shaping** caused by group velocity mismatch in a nonlinear crystal cut for type II phase matching. The process is controlled mainly by a time predelay of the faster pulse in respect to the slower pulse. The principle of the pulse shaping and compression method is described in section 1.4.

I calculated extensive numerical simulations in chapter 3 for the case of Yb:YAG laser pulses and borate crystals, and I also published them in a paper [63]. I focused on two cases: **First, pulse shaping caused by the back-conversion, and second, pulse shaping with a group velocity manipulation through tilting of the pulse front.**

The first of these cases leads to a **compact and easy-to-align setup for nonlinear pulse shaping**. The magnitude of the predelay controls the shape of the 2H pulse, and three main regions can be found: Region of high conversion efficiency of 75 %, which is on par with the SHG process in type I phase matched nonlinear crystal; region of moderate conversion efficiency around 40 % and the pulse shape consisting of a long energetic pedestal and a short and intense pulse on top of it; and a region of **truly short 2H pulse with $\Delta t_{\mathrm{P}}^{\mathrm{FWHM}} = 0.46\,\mathrm{ps}$, meaning 3-fold pulse compression from the 1.5 ps long input pulse, and a very good beam quality of 1.4**, but conversion efficiency of only 11 %.

The group velocity mismatch in borate crystals is, however, not optimal. The second part of the simulations focuses on a case, where the effective group velocities of the interacting pulses are changed by the tilting of the pulse fronts. Particularly, for BBO crystal, PFT angle of 23.5° leads to ideal conditions: the group velocity of the generated 2H pulse is exactly between the group velocities of the *o* and *e* polarized input pulses. Then, if the thickness of the crystal is around 8 mm and the peak intensity is approximatelly 20 $\mathrm{GW/cm^2}$, **2H pulse much shorter than the input pulses can be generated**, and the magnitude of predelay still controls the pulse shaping process. **Specifically, when the predelay is 2.2 ps, the 2H pulse has $\Delta t_{\mathrm{P}}^{\mathrm{FWHM}}$ of 87 fs and is generated with an efficiency of 48 %. This means, that the 2H pulse is almost 20 times shorter than the 1.7 ps long input pulses and the output peak power is increased five times.** The 2H beam quality factor is 3.3, and if one needs better quality beam, then by increasing the predelay to 3.4 ps, one can generate 130 fs long pulse with 20 % efficiency with a beam quality equal to 2.0.

I experimentally verified these results in chapters 4 and 5.

Particularly, in chapter 4 and publications [50, 51], I present the results of experiments with a time predelay, but without the tilting of the pulse fronts. I measured pulse shaping in LBO and BBO crystals.

I measured the BBO crystal with an autocorrelation and by varying the predelay, I observed the region of maximum efficiency, exceeding 50 %, and the region of **the shortest pulse, measured to be 0.75 ps, meaning 2.5-fold pulse compression, with a conversion efficiency of almost 15 %**, at correct predelays. Since the duration of the input pulses was 1.8 ps, so by 0.3 ps longer than in the simulations, the compressed pulse was similarly by 0.3 ps longer than the simulated one. So, **the experimental results followed the simulations remarkably well**.

Next, **I measured the LBO crystal with FROG** and I looked for the second regime of large pedestal and a sharp narrow peak, which could not be observed by the autocorrelation. I have found it at a predelay of 0.33 ps, the pulse was generated with an efficiency of 24 %. **The retrieved pulse shape coincided**

with the simulated one well. The measured beam profiles also agree with the simulations in having a narrower peak and broader pedestal, when compared to a Gaussian beam, although they were asymmetric and deteriorated, limiting the possible applications.

The pulse compression was present, but limited to high hundreds of femtoseconds and rather low conversion efficiency. The experiments, however, followed the simulations exceptionally and gave me confidence in their predictive power, so I moved on to the pulse shaping through tilting of the pulse fronts, hoping to compress the pulses further to low hundreds of femtoseconds, or even below 0.1 ps. I describe these experiments in chapter 5.

For the experiments, **I used two BBO crystals with thicknesses of 6 and 8.5 mm, and the tilting of the pulse fronts was realized by a diffraction grating**. Due to the need of high input energy of few mJ, the laser could not be operated at 10 kHz repetition rate and the pulse duration was therefore only characterized by an autocorrelation.

The measured conversion efficiency was about two times lower than the calculated one, but with the general trends matching closely. **The actual value of conversion efficiency at the predelay with the broadest spectrum was above 20 % for all energies and crystals**, and the maximum efficiency exceeded 30 %. The spectral broadening was observed at the correct predelay and it contained the expected features, even though the spectrum was not as broad as would be ideal. Still, **the measured 4.5 nm wide spectrum supported pulses as short as 95 fs.**

The beam profiles show a ring-like structure, which is in accordance with the numerical simulations. However, the beam profiles were highly irregular and due to that, the autocorrelation traces were asymmetric, casting a shadow of doubt on the possibility of proper pulse duration characterization. The shortest pulse duration measured by the autocorrelation was 0.85 ps, so ten times longer than expected from the simulations. However, **all the other observed parameters hinted strongly at ongoing pulse compression matching with the numerical simulations**. The pulse shape of the non-homogenous beam could be properly measured in the future by e.g. STRIPED FISH method, which can measure full spatial and temporal characteristics of the single laser pulse. The deterioration of the 2H beam could be prevented by using higher quality optics or a top-hat beam profile. If these problems were solved, then **this nonlinear pulse shaping and compression technique with tilted pulse fronts could significantly extend the range of the possible applications of the SHG of Yb:YAG high-average-power thin-disk lasers into the fs regime.**

To conclude, all goals of the thesis were successfully met and most of the results were published or are currently being prepared for publication.

List of publications and references

In this chapter, I provide a list of my publications in journals and conference proceedings related to the nonlinear frequency up-conversion of high energy ultra fast lasers and its applications. For each publication, I describe my contribution. Additionally, peer reviewed publications on other topics, and conference proceedings with me being the first author, are presented. Finally, list of bibliography references is provided.

Publications related to the general topic of thesis

In peer-revied journals

[A.1] **M. Duda**, O. Novák, M. Smrž, A. Lucianetti, V. Kubeček and T. Mocek. 'Numerical study of sum frequency ultrashort pulse compression in borate crystals'. In: *Journal of the Optical Society of America B* 37.11 (Nov. 2020), p. 3229. DOI: 10.1364/JOSAB.401657. I have calculated the numerical simulations and written the paper. O. Novák provided a lot of feedback and helped to make the findings more clear. Rest of the authors provided the equipment and financial and institutional support.

[A.2] P. Hauschwitz, B. Stoklasa, J. Kuchařík, H. Turčičová, M. Písařík, J. Brajer, D. Rostohar, T. Mocek, **M. Duda** and A. Lucianetti. 'Micromachining of Invar with 784 Beams Using 1.3 ps Laser Source at 515 nm'. In: *Materials* 13.13 (July 2020), p. 2962. DOI: 10.3390/ma13132962. I provided the SHG stage serving as the laser source for the reported experiments.

[A.3] **M. Duda**, O. Novák, M. Chyla, M. Smrž and T. Mocek. 'Balancing the conversion efficiency and beam quality of second harmonic generation of a two-picosecond Yb:YAG thin-disk laser'. In: *Laser Physics* 30.2 (Feb. 2020), p. 025405. DOI: 10.1088/1555-6611/ab60b0. I have built the SHG stage and did the optimization, and I have written the paper. O. Novák came up with the task, assisted me with the writing as well as with the measurements. M. Chyla assisted me with the measurement. Rest of the authors provided the equipment and financial and institutional support.

Conference proceedings

[A.4] **M. Duda**, O. Novák, M. Chyła, V. Kubeček, M. Smrž and T. Mocek. 'Shaping of picosecond laser pulses by second harmonic generation with time predelay'. In: *Nonlinear Frequency Generation and Conversion: Materials and Devices XIX*. ed. by P. G. Schunemann and K. L. Schepler. Vol. 1126413. March. SPIE, Mar. 2020, p. 39. DOI: 10.1117/12.2546153. I havev designed and carried out the experiment, and I have presented the results at the conference and written the proceedings. Rest of the authors provided the equipment and financial and institutional support.

[A.5] **M. Duda**, O. Novák, M. Chyła, H. Turčičová, V. Kubeček, M. Smrž and T. Mocek. 'Peak Power Enhancement of Yb:YAG Laser Pulses by Second Harmonic Generation with Time Predelay in Borate Crystals'. In: *2019 Conference on Lasers and Electro-Optics Europe and European Quantum Electronics Conference*. Munich, 2019, cd_p_11. I have designed and carried out the experiment, and I have presented the results at the conference. Rest of the authors provided the equipment and financial and institutional support.

Signatures of selected co-authors, confirming my contribution to the publications above.

....

Other chosen publications

[B.1] D. Vojna, **M. Duda**, R. Yasuhara, O. Slezák, W. Schlichting, K. Stevens, H. Chen, A. Lucianetti and T. Mocek. 'Verdet constant of potassium terbium fluoride crystal as a function of wavelength and temperature'. In: *Optics Letters* 45.7 (Apr. 2020), p. 1683. DOI: 10.1364/OL.387911

[B.2] T. Fok, P. Wachulak, K. Janulewicz, **M. Duda**, Ł. Wegrzyński, A. Bartnik, R. Jarocki and H. Fiedorowicz. 'Near-Edge X-Ray Absorption Fine Structure Spectroscopy of Agarose with a Compact Laser Plasma Soft X-Ray Source'. In: *Acta Physica Polonica A* 137.1 (Jan. 2020), pp. 51–53. DOI: 10.12693/APhysPolA.137.51

[B.3] C. Liberatore, **M. Duda**, P. Sikocinski, M. Chyla, A. Endo, M. Smrz and T. Mocek. 'EUV SOURCE AT HiLASE: THE STATE OF THE ART'. in: *MM Science Journal* 2019.05 (Dec. 2019), pp. 3406–3409. DOI: 10.17973/MMSJ.2019_12_2018131

[B.4] P. Wachulak, **M. Duda**, A. Bartnik, Ł. Wegrzyński, T. Fok and H. Fiedorowicz. 'NEXAFS at nitrogen K-edge and titanium L-edge using a laser-plasma soft x-ray source based on a double-stream gas puff target'. In: *APL Photonics* 4.3 (2019), p. 030807. DOI: 10.1063/1.5085810

[B.5] **M. Duda**, P. Wachulak, T. Fok, Ł. Wegrzyński, A. Jančárek and H. Fiedorowicz. 'A single-shot near edge x-ray absorption fine structure spectroscopy using double stream gas puff target source'. In: *XXII International Symposium on High Power Laser Systems and Applications*. Ed. by P. Di Lazzaro. XXII International Symposium on High Power Laser Systems and Applications. SPIE, Jan. 2019, p. 33. DOI: 10.1117/12.2522429

[B.6] P. Wachulak, **M. Duda**, A. Bartnik, Ł. Wegrzyński, T. Fok, A. Jancarek and H. Fiedorowicz. 'NEXAFS spectroscopy and spectromicroscopy in the soft X-ray spectral region with a compact laser plasma source based on a double stream gas puff target'. In: *Radiation Physics and Chemistry* 175.November 2018 (Oct. 2018), p. 108086. DOI: 10.1016/j.radphyschem.2018.12.006

[B.7] P. Wachulak, **M. Duda**, T. Fok, A. Bartnik, Z. Wang, Q. Huang, A. Sarzyński, A. Jancarek and H. Fiedorowicz. 'Single-Shot near Edge X-ray Fine Structure (NEXAFS) Spectroscopy Using a Laboratory Laser-Plasma Light Source'. In: *Materials* 11.8 (2018), p. 1303. DOI: 10.3390/ma11081303

[B.8] **M. Duda**, P. Wachulak, A. Bartnik, A. Sarzyński, Ł. Węgrzyński, H. Fiedorowicz and A. Jančárek. 'NEXAFS based elemental mapping of EUV irradiated PET with compact soft X-ray source'. In: *Instruments and Methods for Biology and Medicine 2018* (2018), p. 15

[B.9] P. Wachulak, **M. Duda**, A. Bartnik, A. Sarzyński, L. Wegrzynski and H. Fiedorowicz. '2-D elemental mapping of an EUV-irradiated PET with a compact NEXAFS spectromicroscopy'. In: *Spectrochimica Acta Part B: Atomic Spectroscopy* 145 (2018), pp. 107–114. DOI: 10.1016/j.sab.2018.04.014

[B.10] P. Wachulak, **M. Duda**, A. Bartnik, A. Sarzyński, L. Wegrzynski, M. Nowak, A. Jancarek and H. Fiedorowicz. 'Compact system for near edge X-ray fine structure (NEXAFS) spectroscopy using a laser-plasma light source'. In: *Optics Express* 26.7 (2018), p. 8262. DOI: 10.1364/oe.26008260

Bibliographic references

[1] A. Giesen and J. Speiser. 'Fifteen years of work on thin-disk lasers: Results and scaling laws'. In: *IEEE Journal on Selected Topics in Quantum Electronics* 13.3 (2007), pp. 598–609. DOI: 10.1109/JSTQE.2007.897180.

[2] O. Novák, T. Miura, M. Smrž, M. Chyla, S. Nagisetty, J. Mužík, J. Linnemann, H. Turčičová, V. Jambunathan, O. Slezák, M. Sawicka-Chyla, J. Pilař, S. Bonora, M. Divoký, J. Měsíček, A. Pranovich, P. Sikocinski, J. Huynh, P. Severová, P. Navrátil, D. Vojna, L. Horáčková, K. Mann, A. Lucianetti, A. Endo, D. Rostohar and T. Mocek. 'Status of the High Average Power Diode-Pumped Solid State Laser Development at HiLASE'. In: *Applied Sciences* 5.4 (2015), pp. 637–665. DOI: 10.3390/app5040637.

[3] M. Smrž, O. Novák, J. Mužík, H. Turčičová, M. Chyla, S. S. Nagisetty, M. Vyvlečka, L. Roškot, T. Miura, J. Černohorská, P. Sikocinski, L. Chen, J. Huynh, P. Severová, A. Pranovich, A. Endo and T. Mocek. 'Advances in High-Power, Ultrashort Pulse DPSSL Technologies at HiLASE'. In: *Applied Sciences* 7.10 (Oct. 2017), p. 1016. DOI: 10.3390/app7101016.

[4] M. Smrž, J. Mužík, D. Štěpánková, H. Turčičová, O. Novák, M. Chyla, P. Hauschwitz, J. Brajer, J. Kubát, F. Todorov and T. Mocek. 'Picosecond thin-disk laser platform PERLA for multi-beam micromachining'. In: *OSA Continuum* 4.3 (Mar. 2021), p. 940. DOI: 10.1364/OSAC.418293.

[5] R. Jagdheesh, P. Hauschwitz, J. Mužík, J. Brajer, D. Rostohar, P. Jiříček, J. Kopeček and T. Mocek. 'Non-fluorinated superhydrophobic Al7075 aerospace alloy by ps laser processing'. In: *Applied Surface Science* 493.July (2019), pp. 287–293. DOI: 10.1016/j.apsusc.2019.07.035.

[6] P. Hauschwitz, D. Jochcová, R. Jagdheesh, M. Cimrman, J. Brajer, D. Rostohar, T. Mocek, J. Kopeček, A. Lucianetti and M. Smrž. 'Large-Beam Picosecond Interference Patterning of Metallic Substrates'. In: *Materials* 13.20 (Oct. 2020), p. 4676. DOI: 10.3390/ma13204676.

[7] P. Hauschwitz, J. Brajer, D. Rostohar, J. Kopeček, T. Mocek, M. Cimrman, M. Chyla and M. Smrž. 'Anti-Reflection Nanostructures on Tempered Glass by Dynamic Beam Shaping'. In: *Micromachines* 12.3 (Mar. 2021), p. 289. DOI: 10.3390/mi12030289.

[8] P. Hauschwitz, D. Jochcová, R. Jagdheesh, D. Rostohar, J. Brajer, J. Kopeček, M. Cimrman, M. Smrž, T. Mocek and A. Lucianetti. 'Towards rapid large-scale LIPSS fabrication by 4-beam ps DLIP'. In: *Optics & Laser*

Technology 133.August 2020 (Jan. 2021), p. 106532. DOI: 10.1016/j.optlastec.2020.106532.

[9] A. Endo, M. Smrž, J. Mužík, O. Novák, M. Chyla and T. Mocek. 'kW-class picosecond thin-disc prepulse laser Perla for efficient EUV generation'. In: *Journal of Micro/Nanolithography, MEMS, and MOEMS* 16.04 (2017), p. 1. DOI: 10.1117/1.jmm.16.4.041011.

[10] C. Liberatore, M. Duda, P. Sikocinski, M. Chyla, A. Endo, M. Smrz and T. Mocek. 'EUV SOURCE AT HiLASE: THE STATE OF THE ART'. In: *MM Science Journal* 2019.05 (Dec. 2019), pp. 3406–3409. DOI: 10.17973/MMSJ.2019_12_2018131.

[11] J. Vanda, M.-G. Muresan, P. Cech, M. Mydlar, K. Pilna, A. Lucianetti, J. Brajer, T. Mocek, S. Uxa and V. Škoda. 'Multiple pulse picosecond laser induced damage threshold on hybrid mirrors'. In: *Laser-induced Damage in Optical Materials 2020*. Ed. by C. W. Carr, V. E. Gruzdev, D. Ristau and C. S. Menoni. Vol. 11514. International Society for Optics and Photonics. SPIE, 2020, pp. 42–50. DOI: 10.1117/12.2572131.

[12] J. Novák, J. T. Green, T. Metzger, T. Mazanec, B. Himmel, M. Horáček, Z. Hubka, R. Boge, R. Antipenkov, F. Batysta, J. A. Naylon, P. Bakule and B. Rus. 'Thin disk amplifier-based 40 mJ, 1 kHz, picosecond laser at 515 nm'. In: *Optics Express* 24.6 (2016), p. 5728. DOI: 10.1364/OE.24.005728.

[13] S. Karimelahi, L. Abolghasemi and P. R. Herman. 'Rapid micromachining of high aspect ratio holes in fused silica glass by high repetition rate picosecond laser'. In: *Applied Physics A* 114.1 (Jan. 2014), pp. 91–111. DOI: 10.1007/s00339-013-8155-8.

[14] P. Hauschwitz, B. Stoklasa, J. Kuchařík, H. Turčičová, M. Písařík, J. Brajer, D. Rostohar, T. Mocek, M. Duda and A. Lucianetti. 'Micromachining of Invar with 784 Beams Using 1.3 ps Laser Source at 515 nm'. In: *Materials* 13.13 (July 2020), p. 2962. DOI: 10.3390/ma13132962.

[15] U. Quentin, F. Kanal, D. Sutter and C. Stolzenburg. 'Micro-processing in the ultraviolet: UV laser applications in manufacturing consumer electronics (Conference Presentation)'. In: *Laser Applications in Microelectronic and Optoelectronic Manufacturing (LAMOM) XXIV*. Ed. by T. Makimura, G. Račiukaitis and C. Molpeceres. Vol. 10905. International Society for Optics and Photonics. SPIE, 2019. DOI: 10.1117/12.2511116.

[16] H. Sopha, I. Mirza, H. Turčičova, D. Pavlinak, J. Michalicka, M. Krbal, J. Rodriguez-Pereira, L. Hromadko, O. Novák, J. Mužík, M. Smrž, E. Ko-

libalova, N. Goodfriend, N. M. Bulgakova, T. Mocek and J. M. Macak. 'Laser-induced crystallization of anodic TiO 2 nanotube layers'. In: *RSC Advances* 10.37 (2020), pp. 22137–22145. DOI: 10.1039/D0RA02929G.

[17] M. Aladi, I. Márton, P. Rácz, P. Dombi and I. B. Földes. 'High harmonic generation and ionization effects in cluster targets'. In: *High Power Laser Science and Engineering* 2.September (2014). DOI: 10.1017/hpl.2014.32.

[18] C. Y. Chien and M. C. Gupta. 'Pulse width effect in ultrafast laser processing of materials'. In: *Applied Physics A: Materials Science and Processing* 81.6 (2005), pp. 1257–1263. DOI: 10.1007/s00339-004-2989-z.

[19] C.-L. Tsai, F. Meyer, A. Omar, Y. Wang, A.-Y. Liang, C.-H. Lu, M. Hoffmann, S.-D. Yang and C. J. Saraceno. 'Efficient nonlinear compression of a mode-locked thin-disk oscillator to 27 fs at 98 W average power'. In: *Opt. Lett.* 44.17 (Sept. 2019), pp. 4115–4118. DOI: 10.1364/OL.44.004115.

[20] B. E. A. Saleh and M. C. Teich. *Fundamentals of photonics*. 2nd. Hoboken, NJ: John Wiley & Sons, Inc, Mar. 2007, p. 1200.

[21] R. W. Boyd. *Nonlinear Optics*. 3rd. Elsevier, 2008, p. 640.

[22] A. Smith. *Crystal Nonlinear Optics: With SNLO Examples*. AS-Photonics, 2018.

[23] H. Fattahi, A. Alismail, H. Wang, J. Brons, O. Pronin, T. Buberl, L. Vámos, G. Arisholm, A. M. Azzeer and F. Krausz. 'High-power, 1-ps, all-Yb:YAG thin-disk regenerative amplifier'. In: *Optics Letters* 41.6 (Mar. 2016), p. 1126. DOI: 10.1364/OL.41.001126.

[24] A. Alismail, H. Wang, J. Brons and H. Fattahi. '20 mJ, 1 ps Yb:YAG Thin-disk Regenerative Amplifier'. In: *Journal of Visualized Experiments* 2017.125 (July 2017), pp. 1–9. DOI: 10.3791/55717.

[25] J. R. Lee, R. B. Birch, B. Fulford and D. Birkin. 'Operation of a novel, dual function thin slab ultrafast amplifier at 1030 nm, 515 nm and 343 nm'. English. In: *SOLID STATE LASERS XXIX: TECHNOLOGY AND DEVICES*. Ed. by Clarkson, WA and Shori, RK. Vol. 11259. Proceedings of SPIE. Conference on Solid State Lasers XXIX - Technology and Devices, San Francisco, CA, FEB 04-06, 2020. SPIE. 1000 20TH ST, PO BOX 10, BELLINGHAM, WA 98227-0010 USA: SPIE-INT SOC OPTICAL ENGINEERING, 2020. DOI: 10.1117/12.2544278.

[26] C. Röcker, A. Loescher, F. Bienert, P. Villeval, D. Lupinski, D. Bauer, A. Killi, T. Graf and M. Abdou Ahmed. 'Ultrafast green thin-disk laser

exceeding 1.4 kW of average power'. In: *Optics Letters* 45.19 (Oct. 2020), p. 5522. DOI: 10.1364/OL.403781.

[27] A. Kornev, R. Balmashnov, E. Viktorov, A. Davtian, V. Koval, A. Makarov and I. Kuchma. 'High-energy high-power near-diffraction-limited 1064 and 532 nm picosecond Nd:YAG laser'. In: *Electronics Letters* 56.7 (Mar. 2020), pp. 339–342. DOI: 10.1049/el.2019.3173.

[28] O. Novák, H. Turčičová, M. Smrž, T. Miura, A. Endo and T. Mocek. 'Picosecond green and deep ultraviolet pulses generated by a high-power 100 kHz thin-disk laser'. In: *Optics Letters* 41.22 (2016), p. 5210. DOI: 10.1364/OL.41.005210.

[29] H. Turcicova, O. Novak, L. Roskot, M. Smrz, J. Muzik, M. Chyla, A. Endo and T. Mocek. 'New observations on DUV radiation at 257 nm and 206 nm produced by a picosecond diode pumped thin-disk laser'. In: *Optics Express* 27.17 (Aug. 2019), p. 24286. DOI: 10.1364/OE.27.024286.

[30] M. Duda, O. Novák, M. Chyla, M. Smrž and T. Mocek. 'Balancing the conversion efficiency and beam quality of second harmonic generation of a two-picosecond Yb:YAG thin-disk laser'. In: *Laser Physics* 30.2 (Feb. 2020), p. 025405. DOI: 10.1088/1555-6611/ab60b0.

[31] J. Moses and S.-W. Huang. 'Conformal profile theory for performance scaling of ultrabroadband optical parametric chirped pulse amplification'. In: *Journal of the Optical Society of America B* 28.4 (2011), p. 812. DOI: 10.1364/josab.28.000812.

[32] Y. Wang and R. Dragila. 'Efficient conversion of picosecond laser pulses into second-harmonic frequency using group-velocity dispersion'. In: *Physical Review A* 41.10 (1990), p. 5645. DOI: 10.1103/PhysRevA.41.5645.

[33] A. Stabinis, G. Valiulis and E. A. Ibragimov. 'Effective sum frequency pulse compression in nonlinear crystals'. In: *Optics Communications* 86.3-4 (1991), pp. 301–306. DOI: 10.1016/0030-4018(91)90009-3.

[34] Y. Wang and B. Luther-Davies. 'Frequency-doubling pulse compressor for picosecond high-power neodymium laser pulses'. In: *Optics letters* 17.20 (1992), p. 1459. DOI: 10.1364/OL.17.001459.

[35] A. Umbrasas, J.-C. Diels, J. Jacob, G. Valiulis and A. Piskarskas. 'Generation of femtosecond pulses through second-harmonic compression of the output of a Nd: YAG laser'. In: *Optics letters* 20.21 (1995), p. 2228. DOI: 10.1364/OL.20.002228.

[36] T. Zhang, H. Daido, Y. Kato, L. B. Sharma, Y. Izawa and S. Nakai. 'Second-Harmonic Generation of a Picosecond Laser Pulse at High Intensities with Time Predelay'. In: *Japanese Journal of Applied Physics* 34 (1995), p. 3546. DOI: 10.1143/JJAP.34.3546.

[37] C. Y. Chien, G. Korn, J. S. Coe, J. Squier, G. Mourou and R. S. Craxton. 'Highly efficient second-harmonic generation of ultraintense Nd-glass laser pulses'. In: *Optics Letters* 20.4 (1995), p. 353. DOI: 10.1364/OL.20.000353.

[38] A. Dubietis, G. Tamošauskas and A. Varanavičius. 'Femtosecond third-harmonic pulse generation by mixing of pulses with different duration'. In: *Optics Communications* 186.1-3 (2000), p. 211. DOI: 10.1016/S0030-4018(00)01046-4.

[39] T. Zhang, Y. Kato and H. Daido. 'Numerical study of fourth-harmonic generation of a picosecond laser pulse with time predelay'. In: *Journal of the Optical Society of America B* 13.6 (June 1996), p. 1166. DOI: 10.1364/JOSAB.13.001166.

[40] G. Veitas, A. Dubietis, G. Valiulis, D. Podenas and G. Tamošauskas. 'Efficient femtosecond pulse generation at 264 nm'. In: *Optics Communications* 138.4-6 (1997), pp. 333–336. DOI: 10.1016/S0030-4018(97)00072-2.

[41] R. Danielius, A. Dubietis, A. Piskarskas, G. Valiulis and A. Varanavicius. 'Generation of compressed 600-720-nm tunable femtosecond pulses by transient frequency mixing in a beta-barium borate crystal'. In: *Optics letters* 21.3 (1996), p. 216. DOI: 10.1364/OL.21.000216.

[42] M. Nisoli, S. De Silvestri, G. Valiulis and A. Varanavicius. 'Fivefold femtosecond pulse compression by sum frequency generation'. In: *Applied Physics Letters* 68.25 (1996), p. 3540. DOI: 10.1063/1.116523.

[43] T. Zhang, Y. Kato, K. Yamakawa, H. Daido and Y. Izawa. 'Peak intensity enhancement and pulse compression of a picosecond laser pulse by frequency doubling with a predelay'. In: *Japanese Journal of Applied Physics* 34 (1995), p. 3552. DOI: 10.1143/JJAP.34.3552.

[44] A. Dubietis, G. Valiulis, R. Danielius and A. Piskarskas. 'Fundamental-frequency pulse compression through cascaded second-order processes in a type II phase-matched second-harmonic generator.' In: *Optics letters* 21.16 (1996), p. 1262. DOI: 10.1364/OL.21.001262.

[45] T. Zhang and M. Yonemura. 'Pulse Shaping of Ultrashort Laser Pulses with Nonlinear Optical Crystals'. In: *Japanese Journal of Applied Physics* 38.11 (Nov. 1999), p. 6351. DOI: 10.1143/JJAP.38.6351.

[46] T. Harimoto, M. Aoyama and K. Yamakawa. 'Numerical simulation of self-compressed second-harmonic generation in type II potassium dihydrogen phosphate with a time predelay for Yb-doped solid-state lasers'. In: *Optics Express* 15.26 (2007), p. 17529. DOI: 10.1364/OE.15.017529.

[47] D. Eimerl. 'High average power harmonic generation'. In: *IEEE Journal of Quantum Electronics* 23.5 (1987), pp. 575–592. DOI: 10.1109/JQE.1987.1073391.

[48] A. Smith. *SNLO software*. online, http://www.as-photonics.com/.

[49] S. Beyer, C. Grebing, M. Schultze, K. Michel, G. Korn and T. Metzger. 'High Average Power Type II Frequency Doubling with a Predelay for Pulse Compression and Peak Intensity Enhancement'. In: *Conference on Lasers and Electro-Optics*. OSA Technical Digest, 2018, SM3N.4. DOI: 10.1364/CLEO_SI.2018.SM3N.4.

[50] M. Duda, O. Novák, M. Chyła, H. Turčičová, V. Kubeček, M. Smrž and T. Mocek. 'Peak Power Enhancement of Yb:YAG Laser Pulses by Second Harmonic Generation with Time Predelay in Borate Crystals'. In: *2019 Conference on Lasers and Electro-Optics Europe and European Quantum Electronics Conference*. Munich, 2019, cd_p_11.

[51] M. Duda, O. Novák, M. Chyła, V. Kubeček, M. Smrž and T. Mocek. 'Shaping of picosecond laser pulses by second harmonic generation with time predelay'. In: *Nonlinear Frequency Generation and Conversion: Materials and Devices XIX*. Ed. by P. G. Schunemann and K. L. Schepler. Vol. 1126413. March. SPIE, Mar. 2020, p. 39. DOI: 10.1117/12.2546153.

[52] R. Danielius, P. Di Trapani, C. Solcia, P. Foggi, A. Andreoni and A. Piskarskas. 'Matching of group velocities by spatial walk-off in collinear three-wave interaction with tilted pulses'. In: *Optics Letters* 21.13 (July 1996), p. 973. DOI: 10.1364/OL.21.000973.

[53] A. Dubietis, G. Valiulis, G. Tamosauskas, R. Danielius and A. Piskarskas. 'Nonlinear second-harmonic pulse compression with tilted pulses'. In: *Optics letters* 22.14 (1997), p. 1071. DOI: 10.1364/OL.22.001071.

[54] A. Dubietis, G. Valiulis, G. Tamosauskas, R. Danielius and A. Piskarskas. 'Nonlinear pulse compression in the ultraviolet'. In: *Optics Communications* 144.1-3 (1997), p. 55. DOI: 10.1016/S0030-4018(97)00431-8.

[55] T. Zhang and M. Yonemura. 'Pulse Compression with a Noncollinear Type I Frequency Doubling Crystal'. In: *Japanese Journal of Applied Physics* 37.Part 1, No. 2 (Feb. 1998), pp. 542–543. DOI: 10.1143/JJAP.37.542.

[56] J. Biegert and J.-C. Diels. 'Compression of pulses of a few optical cycles through harmonic generation'. In: *Journal of the Optical Society of America B* 18.8 (2001), p. 1218. DOI: 10.1364/JOSAB.18.001218.

[57] T. Zhang, K. Yamakawa, M. Aoyama and M. Yonemura. 'Temporal solitons in second-harmonic generation with a noncollinear phase-mismatching scheme'. In: *Applied Optics* 40.9 (Mar. 2001), p. 1417. DOI: 10.1364/AO.40.001417.

[58] A. Grün, D. R. Austin, S. L. Cousin and J. Biegert. 'Three-wave mixing mediated femtosecond pulse compression in β-barium borate'. In: *Optics Letters* 40.20 (2015), p. 4679. DOI: 10.1364/OL.40.004679.

[59] B. Willenberg, F. Brunner, C. R. Phillips and U. Keller. 'High-power picosecond deep-UV source via group velocity matched frequency conversion'. In: *Optica* 7.5 (May 2020), p. 485. DOI: 10.1364/OPTICA.386257.

[60] Z. Bor and B. Rácz. 'Group velocity dispersion in prisms and its application to pulse compression and travelling-wave excitation'. In: *Optics Communications* 54.3 (June 1985), pp. 165–170. DOI: 10.1016/0030-4018(85)90284-6.

[61] N. Schiller and R. Alfano. 'Picosecond characteristics of a spectrograph measured by a streak camera/video readout system'. In: *Optics Communications* 35.3 (Dec. 1980), pp. 451–454. DOI: 10.1016/0030-4018(80)90072-3.

[62] S. Szatmari, G. Kuhnle and P. Simon. 'Pulse compression and traveling wave excitation scheme using a single dispersive element'. In: *Applied Optics* 29.36 (Dec. 1990), p. 5372. DOI: 10.1364/AO.29.005372.

[63] M. Duda, O. Novák, M. Smrž, A. Lucianetti, V. Kubeček and T. Mocek. 'Numerical study of sum frequency ultrashort pulse compression in borate crystals'. In: *Journal of the Optical Society of America B* 37.11 (Nov. 2020), p. 3229. DOI: 10.1364/JOSAB.401657.

[64] R. H. French, J. W. Ling, F. S. Ohuchi and C. T. Chen. 'Electronic structure of β-BaB2O4 and LiB3O5 nonlinear optical crystals'. In: *Physical Review B* 44.16 (Oct. 1991), pp. 8496–8502. DOI: 10.1103/PhysRevB.44.8496.

[65] R. Riedel, J. Rothhardt, K. Beil, B. Gronloh, A. Klenke, H. Höppner, M. Schulz, U. Teubner, C. Kränkel, J. Limpert, A. Tünnermann, M. Prandolini and F. Tavella. 'Thermal properties of borate crystals for high power optical parametric chirped-pulse amplification'. In: *Optics Express* 22.15 (July 2014), p. 17607. DOI: 10.1364/OE.22.017607.

[66] O. E. Martinez. 'Pulse distortions in tilted pulse schemes for ultrashort pulses'. In: *Optics Communications* 59.3 (Sept. 1986), pp. 229–232. DOI: 10.1016/0030-4018(86)90290-7.

[67] O. Martinez. 'Achromatic phase matching for second harmonic generation of femtosecond pulses'. In: *IEEE Journal of Quantum Electronics* 25.12 (1989), pp. 2464–2468. DOI: 10.1109/3.40630.

[68] P. Gabolde and R. Trebino. 'Single-frame measurement of the complete spatiotemporal intensity and phase of ultrashort laser pulses using wavelength-multiplexed digital holography'. In: *J. Opt. Soc. Am. B* 25.6 (June 2008), A25–A33. DOI: 10.1364/JOSAB.25.000A25.

[69] Z. Guang, M. Rhodes, M. Davis and R. Trebino. 'Complete characterization of a spatiotemporally complex pulse by an improved single-frame pulse-measurement technique'. In: *J. Opt. Soc. Am. B* 31.11 (Nov. 2014), pp. 2736–2743. DOI: 10.1364/JOSAB.31.002736.

[70] D. Vojna, M. Duda, R. Yasuhara, O. Slezák, W. Schlichting, K. Stevens, H. Chen, A. Lucianetti and T. Mocek. 'Verdet constant of potassium terbium fluoride crystal as a function of wavelength and temperature'. In: *Optics Letters* 45.7 (Apr. 2020), p. 1683. DOI: 10.1364/OL.387911.

[71] T. Fok, P. Wachulak, K. Janulewicz, M. Duda, Ł. Wegrzyński, A. Bartnik, R. Jarocki and H. Fiedorowicz. 'Near-Edge X-Ray Absorption Fine Structure Spectroscopy of Agarose with a Compact Laser Plasma Soft X-Ray Source'. In: *Acta Physica Polonica A* 137.1 (Jan. 2020), pp. 51–53. DOI: 10.12693/APhysPolA.137.51.

[72] P. Wachulak, M. Duda, A. Bartnik, Ł. Wegrzyński, T. Fok and H. Fiedorowicz. 'NEXAFS at nitrogen K-edge and titanium L-edge using a laser-plasma soft x-ray source based on a double-stream gas puff target'. In: *APL Photonics* 4.3 (2019), p. 030807. DOI: 10.1063/1.5085810.

[73] M. Duda, P. Wachulak, T. Fok, Ł. Wegrzyński, A. Jančárek and H. Fiedorowicz. 'A single-shot near edge x-ray absorption fine structure spectroscopy using double stream gas puff target source'. In: *XXII International Symposium on High Power Laser Systems and Applications*. Ed. by P. Di

Lazzaro. XXII International Symposium on High Power Laser Systems and Applications. SPIE, Jan. 2019, p. 33. DOI: 10.1117/12.2522429.

[74] P. Wachulak, M. Duda, A. Bartnik, Ł. Wegrzyński, T. Fok, A. Jancarek and H. Fiedorowicz. 'NEXAFS spectroscopy and spectromicroscopy in the soft X-ray spectral region with a compact laser plasma source based on a double stream gas puff target'. In: *Radiation Physics and Chemistry* 175.November 2018 (Oct. 2018), p. 108086. DOI: 10.1016/j.radphyschem.2018.12.006.

[75] P. Wachulak, M. Duda, T. Fok, A. Bartnik, Z. Wang, Q. Huang, A. Sarzyński, A. Jancarek and H. Fiedorowicz. 'Single-Shot near Edge X-ray Fine Structure (NEXAFS) Spectroscopy Using a Laboratory Laser-Plasma Light Source'. In: *Materials* 11.8 (2018), p. 1303. DOI: 10.3390/ma11081303.

[76] M. Duda, P. Wachulak, A. Bartnik, A. Sarzyński, Ł. Węgrzyński, H. Fiedorowicz and A. Jančárek. 'NEXAFS based elemental mapping of EUV irradiated PET with compact soft X-ray source'. In: *Instruments and Methods for Biology and Medicine 2018* (2018), p. 15.

[77] P. Wachulak, M. Duda, A. Bartnik, A. Sarzyński, L. Wegrzynski and H. Fiedorowicz. '2-D elemental mapping of an EUV-irradiated PET with a compact NEXAFS spectromicroscopy'. In: *Spectrochimica Acta Part B: Atomic Spectroscopy* 145 (2018), pp. 107–114. DOI: 10.1016/j.sab.2018.04.014.

[78] P. Wachulak, M. Duda, A. Bartnik, A. Sarzyński, L. Wegrzynski, M. Nowak, A. Jancarek and H. Fiedorowicz. 'Compact system for near edge X-ray fine structure (NEXAFS) spectroscopy using a laser-plasma light source'. In: *Optics Express* 26.7 (2018), p. 8262. DOI: 10.1364/oe.26008260.